

MULTIPHASE MASTER

Erasmus Mundus

MSc thesis report

Computational Modeling of Superheated Steam Spray Drying of Particles Using an Eulerian-Lagrangian Framework

Nikodem Dabrowski (cohort M25)

August 17, 2026

The MULTIPHASE MSc program is an Erasmus Mundus Joint Master Degree funded by the European Union. It aims at educating young scientists in the field of multiphase systems for sustainable engineering. These systems are made of a dispersed medium (particles, drops, bubbles, ...) surrounded by a fluid phase (liquid or gas). The program give the students the opportunity to understand the different phenomena (mechanical behaviour, heat and mass transfer, chemical reactions, ...), to see how they come into play in industrial unit operations, and to model them with analytical approaches or advanced numerical simulation tools.

This program is jointly offered by a consortium of three institutions: the Ecole des Mines de Saint-Etienne (France), the Politecnico di Torino (Italy) and the Technische Universtät München (Germany). After one semester in each institution and master thesis, the successfull students receive three master degrees:

- MSc. Process and bio-process engineering delivered by Mines Saint-Etienne
- MSc. Chemical & sustainable processes engineering delivered by Politecnico di Torino
- MSc. Materials Science and Engineering delivered by Technische Universität München

More information on this program is available at: www.multiphase-master.eu

Co-funded by the European Union

Contents

1 Introduction **1**
- 1.1 Background and Motivation . . . 1
- 1.2 Engineering Challenges . . . 2
- 1.3 Research Gap . . . 2
- 1.4 Research Objectives . . . 3
- 1.5 Thesis Outline . . . 3

2 Literature Review: Spray Drying and Superheated Steam **5**
- 2.1 Drying as a Fundamental Unit Operation . . . 5
  - 2.1.1 Drying Technologies . . . 5
- 2.2 Spray Drying . . . 6
  - 2.2.1 Fundamental Principles of Spray Drying . . . 6
  - 2.2.2 Spray Dryer Design . . . 8
- 2.3 Superheated Steam Spray Drying . . . 10
  - 2.3.1 Superheated Steam Kinetics . . . 11
  - 2.3.2 Challenges in Numerical Modeling of SHS Environments . . . 12

3 Physical and Mathematical Modeling **15**
- 3.1 Governing Equations for the Continuous Phase . . . 15
  - 3.1.1 Conservation of Mass . . . 16
  - 3.1.2 Conservation of Momentum . . . 16
  - 3.1.3 Conservation of Energy . . . 16
  - 3.1.4 Equation of State and Transport Properties . . . 17
- 3.2 Turbulence Modeling . . . 18
  - 3.2.1 The $k-\epsilon$ Turbulence Model . . . 19
  - 3.2.2 The $k-\omega$ Turbulence Model . . . 19
  - 3.2.3 Model Adequacy and Selection . . . 19
- 3.3 Discrete Phase Modeling . . . 20
  - 3.3.1 Forces Acting on a Particle . . . 20
  - 3.3.2 Significant Forces in CFD . . . 22
- 3.4 Coupling of Droplet Evaporation with Gas Dynamics . . . 22
  - 3.4.1 Initial Condensation and Sensible Heating Regime . . . 22
  - 3.4.2 Constant Rate Evaporation . . . 23
  - 3.4.3 Falling-Rate Period . . . 23
- 3.5 Phase Coupling and Source Terms . . . 24
  - 3.5.1 Source Term Quantification . . . 24

4 Numerical Framework and Implementation **27**
- 4.1 Hydrodynamic Tracking of Particles . . . 27
  - 4.1.1 Single Phase Flow . . . 27
  - 4.1.2 Multiphase Flow Implementation . . . 30
- 4.2 Hydrodynamic and Thermal Simulation . . . 31
  - 4.2.1 Model Architecture . . . 32

5 Verification and Validation **37**
5.1 Single Phase Flow . . . 37
5.1.1 Flow Regime Assessment . . . 37
5.1.2 Mesh Sensitivity Study . . . 41
5.2 Verification of Multiphase Hydrodynamics . . . 45
5.3 Verification of crustReactingParcelFoam . . . 48
5.3.1 Baseline verification . . . 48
5.3.2 Code Validation . . . 51
5.3.3 Computational Profiling and Code Optimization . . . 52
5.3.4 Declaration on the Use of Generative AI . . . 53

6 Results and Discussion **55**
6.1 Passive Particle Transport in Steam Environment . . . 55
6.1.1 Effect on the Continuous Phase Hydrodynamics . . . 55
6.1.2 Particle Kinematics and Spatial Deposition Patterns . . . 56
6.1.3 Particle Residence Time Distribution . . . 57
6.2 Coupled Heat and Mass Transfer Simulation . . . 66
6.2.1 Effect on the Continuous Phase . . . 66
6.2.2 Particle Kinematics and Spatial Deposition Patterns . . . 69
6.2.3 Residence Time Distribution and Product Properties Analysis . . . 69
6.3 Particle Drying Kinetics . . . 80

7 Conclusion and Future Work **83**
7.1 Key Findings . . . 83
7.2 Model Limitation . . . 84
7.3 Future Work . . . 85

Nomenclature **87**

Bibliographic references **91**

ABSTRACT

Traditional air-based spray drying is widely used in industry but suffers from high energy consumption and safety risks, such as dust explosions and product oxidation. Superheated Steam Drying offers a sustainable alternative, enabling up to 80% energy recovery in a closed-loop, oxygen-free environment. However, its industrial adoption is limited by complex flow physics and the difficulty of taking physical measurements inside the operating chamber. To address this, this thesis develops a custom multiphase phase-change library within the open-source Computational Fluid Dynamic framework, OpenFOAM.

Using a three-dimensional, two-way coupled Eulerian-Lagrangian approach, the model simulates heat-transfer limited evaporation and solid crust formation. Simulations of the continuous phase revealed a stable, oscillating central vortex core along the chamber axis. When tracking individual particles, their behavior was highly dependent on size. Fine droplets follow the gas streamlines closely, causing them to get trapped in the central vortex and extending the global Residence Time Distribution. Coarser droplets migrate toward the walls due to higher inertia, creating a characteristic helical roping pattern before descending.

Thermally coupled simulations showed an 80 K temperature drop directly beneath the nozzle, marking the zone of intense evaporation. Crucially, the rapid drying kinetics ensure that droplets form a rigid crust before hitting the walls, theoretically eliminating wet-particle wall fouling. Sensitivity analyses indicated that while the final product properties are robustly insensitive to initial injection velocities, angles, and droplet subcooling, they depend heavily on the feedstock mass flow rate, inlet particle size distribution, and the critical moisture parameter.

Ultimately, this research provides a clear, physics-based tool to help process engineers optimize SSD systems without relying on costly empirical trial-and-error. While bounded by simplifying assumptions — such as isotropic turbulence approximations and the absence of a steam condensation sub-model — the framework establishes a reliable foundation for future multiphase drying research.

Keywords: Lagrangian, Eulerian, Particle, Spray Drying

Chapter 1

Introduction

1.1 Background and Motivation

The global manufacturing sector is subject to increasingly strict legislation regarding environmental protection, greenhouse gas emissions, and sustainable energy utilization, making the decarbonization and electrification of industrial processes a priority. Industrial drying operations are significant energy sinks, currently accounting for approximately 12 to 20% of the total energy consumed withing developed manufacturing sectors [1]. Over 85% of these industrial dryer operate via convection, employing hot air or flue gases as the drying medium [2]. The reliance on fossil fuel combustion to generate these high temperature gas streams contributes heavily to global greenhouse gases emissions.

Spray drying is a wide spread unit operation used for drying liquid slurries [3]. The flexibility of this technology has made it indispensable across a variety of fields, including the fine chemicals, biotechnology, food, and pharmaceutical sectors. It is often employed in manufacturing of high-value products. Its primary advantage lies in the degree of control it offers over droplet atomization and the evaporation kinetics. By modifying operational parameters, engineers can carefully tailor final particle morphologies, residual moisture content, and the overall particle size distribution.

Despite its flexibility, conventional air drying is energy demanding, which is tied to the high latent heat of vaporization of water. In a standard hot-air spray dryer, the continuous gas phase is vented to the atmosphere to carry away the evaporated moisture. This results in the irreversible energy loss in form of sensible heat and latent enthalpy. Attempting to recover this latent heat from the humid exhaust air is both economically and physically challenging; the presence of a non-condensable carrier gas suppresses the dew point to a rather low temperature of approximately 50 degrees Celsius, limiting how much energy can actually be recovered.

Beyond these thermodynamic limitations, using hot air as the primary drying medium introduces several constraints regarding process safety and product degradation. Processing organic food concentrates or certain pharmaceutical products carries the risk of dust explosions and fire hazards. Mitigating these risks often requires deploying closed-loop inert nitrogen atmospheres, which drives up capital equipment costs and operational overhead [4, 5].

Furthermore, exposing the product to oxygen throughout the drying cycle can trigger oxidative degradation, potentially compromising the quality of the final powder. It is also worth noting that the continuous atmospheric exhaust of conventional systems contributes to greenhouse gas footprints and creates challenges regarding the emission of volatile organic compounds and fine particulate matter.

To navigate these bottlenecks of conventional air drying, there is a growing shift in the industry toward Superheated Steam Drying architectures. By substituting hot air with steam, the spray dryer effectively becomes a closed-loop, oxygen-free environment [6]. Because the exhaust stream consists entirely of pure steam without any non-condensable carrier gases, the latent heat supplied for evaporation can be almost entirely recovered through direct condensation or mechanical vapor recompression [7, 1, 8]. This shift towards steam has the potential to significantly reduce net specific energy consumption, offering estimated energy savings of 60% to 80% when compared to conventional hot-air operations [8]. These energy savings directly corresponds to a significant reduction in operational expenditure.

In addition to the energy conservation benefits, the use of superheated steam can lead to improvements in process kinetics, product quality and operational safety. Operating in an oxygen-free environment eliminates the risk of dust explosions, while at the same time preventing oxidative product degradation. From a kinetic perspective, the application of steam can facilitate higher evaporation rates due to steam's superior specific heat capacity and thermal conductivity [7]. Interestingly, the rapid moisture vaporization characteristic of a superheated steam environment often triggers early crust formation and droplet inflation [8, 9]. This yields a highly porous final particle structure with favorable wettability properties.

1.2 Engineering Challenges

While Superheated Steam Drying offers distinct thermodynamic benefits, its widespread industrial adoption remains somewhat hindered by both operational hurdles and complex, multi-scale flow physics. Unlike conventional open-loop air dryers, SSD units must be engineered as sealed, closed-loop systems. Component interfaces must be pressure-resistant and gas-tight

Aside from mechanical constraints, the phase-change kinetics introduce highly non-linear transport phenomena. Because the slurry is typically injected at a temperature well below the steam's saturation point, the droplets initially act as microscopic thermal sinks. This causes the surrounding continuous phase to condense onto the droplet surfaces, temporarily increasing their mass and moisture content before the boiling-driven evaporation can begin. Consequently, the coupled heat, mass, and momentum transfers become sensitive to localized thermodynamic gradients, causing traditional empirical scale-up heuristics to be largely ineffective.

There are empirical limitations associated with analyzing spray drying systems. In classical chemical engineering, unit operations are traditionally modeled using data gathered from pilot-plant scaling trials. However, obtaining high quality data regarding the transient kinematics and thermodynamics of the dispersed phase is challenging. The drying chamber is characterized by highly transient, turbulent, and three-dimensional swirling flow fields. There are steep temperature gradients and large recirculation zones. Monitoring devices are difficult to install in such a harsh environment, as they are quickly compromised by high temperatures and wet-particle fouling [10].

Furthermore, standard measuring equipment fail to capture the microscopic reality of the multiphase phenomena. Tracking the precise spatial trajectories, localized velocities, and morphological evolution of millions of individual discrete droplets exceeds the capacity of conventional measurement techniques. Relying solely on macroscopic inlet and outlet parameters effectively reduces the drying chamber to a black box, obscuring the localized physical phenomena governing the actual powder formation [11].

Computational Fluid Dynamics bypasses physical measurement limits to capture precise drying kinetics. Using an Eulerian–Lagrangian framework, the model treats superheated steam as a continuous volumetric field while tracking individual droplets via Newtonian mechanics. Two-way coupling models the heat and momentum exchange between both phases. This delivers detailed particle histories, residence times, and wall-impact heat maps, allowing engineers to optimize nozzle specs, chamber geometries, and operating conditions without expensive trial-and-error.

1.3 Research Gap

While initial efforts to utilize Computational Fluid Dynamics for modeling superheated steam spray drying date back to 1999 [12], the available scientific literature remains fragmented and lacks comprehensive, high-fidelity analyses. Many existing studies rely on simplifying assumptions that compromise model accuracy. For instance, the frequent use of two-dimensional axisymmetric geometries fails to capture the complex, asymmetrical three-dimensional swirling flow structures characteristic of cyclonic drying chambers [10]. Furthermore, many models employ a restricted one-way phase coupling assumption, in which the continuous steam phase advects the dispersed droplets and the particles act as passive scalars, failing to exert reciprocal momentum, mass, or heat source terms back onto the fluid domain [13].

Additionally, the current literature exhibits a distinct absence of fully coupled phase-change models that incorporate dynamic solid crust formation. Foundational studies, such as the work by Frydman et al. [12], often simplify the drying kinetics by assuming the formation of uniformly dense particles. This

assumption misrepresents the inertial response and Lagrangian trajectories of the highly porous, inflated particles typically generated by the rapid vaporization kinetics of a superheated steam environment.

There is also a lack of systematic parametric sensitivity studies within SSD frameworks. Comprehensive evaluations detailing the macroscopic impact of specific atomizer operating conditions, such as the liquid feedstock mass flow rate, initial droplet velocity, and injection cone angle, on the residence time distribution are largely missing from the literature. Additionally, detailed spatial analyses of particle-wall collision patterns and verifications of Lagrangian discretization independence (parcel count sensitivity) remain underexplored in the context of pure steam drying.

A significant technical barrier contributing to this research gap is the fundamental limitation of standard open-source CFD architectures, such as native OpenFOAM solvers. These standard frameworks are mathematically formulated to model evaporation into an inert, non-condensable carrier gas, where the interphase mass transfer is driven by concentration gradients (Fickian diffusion). Conversely, vaporization within a pure superheated steam environment is governed by convective heat transfer; the evaporation rate is limited by the thermal gradient rather than species diffusion. Standard multi-species mass-transfer libraries are incapable of resolving this pure-vapor boiling mechanism.

In summary, while the conceptual foundation for numerical SSD modeling exists, past implementations are constrained by low-fidelity spatial discretizations, incomplete Eulerian-Lagrangian coupling, and an inability to correctly resolve pure-vapor thermodynamic phase changes. As a result, a robust, fully coupled 3D parametric analysis of droplet kinematics and drying histories is required to bridge this gap in the current literature.

1.4 Research Objectives

This thesis aims to develop a high-fidelity numerical framework for simulating superheated steam spray drying. Specifically, this work is driven by the following primary research objectives:

- The development and numerical verification of a custom phase-change thermodynamic library within the OpenFOAM framework, specifically formulated to resolve heat-transfer limited superheated steam evaporation and dynamic solid crust formation.
- The evaluation of the macroscopic continuous-phase hydrodynamics of the drying chamber and the validity and necessity of the two-way Eulerian-Lagrangian interphase momentum coupling.
- Conducting parametric sensitivity study assessing the influence of critical atomization and operating conditions (injection angle, initial droplet velocity, inlet particle size distribution, and feedstock mass flow rate) on the residence time distributions, final product morphology, spatial boundary deposition patterns, and residual moisture content.

1.5 Thesis Outline

The reminder of this thesis is structured as follows:

- **Chapter 2** provides a literature review on the fundamental principles of spray drying and the specific application of superheated steam as the continuous drying medium.
- **Chapter 3** details the physical phenomena governing the multiphase system and outlines the mathematical formulations required to describe the coupled momentum, heat, and mass transfer. These formulations form the theoretical basis for the subsequent computational modeling.
- **Chapter 4** focuses on the numerical methodology utilized to discretize and solve the governing equations within the Computational Fluid Dynamics framework. This section defines the selected boundary conditions, solver configurations, and computational domain setup.
- **Chapter 5** presents the verification and validation protocols employed to ensure the accuracy and reliability of the numerical model. It defines the underlying mathematical and physical assumptions, establishing the computational confidence required for the subsequent predictive analyses.

- **Chapter 6** constitutes the primary analytical core of the thesis, presenting a discussion of the simulation results. It evaluates the parametric sensitivity of the system to various initial and boundary conditions, interpreting these findings from an applied process engineering perspective.
- **Chapter 7** summarizes the conclusions drawn from the research, addresses the inherent limitations of the implemented model, and proposes potential trajectories for future numerical and empirical investigation.

Chapter 2

Literature Review: Spray Drying and Superheated Steam

2.1 Drying as a Fundamental Unit Operation

Drying is among the most common and energy-intensive unit operations in the chemical process industries [14]. It is estimated that industrial drying accounts for approximately 12% of the total energy consumption in manufacturing, a figure that underscores the necessity for process optimization [1]. While the operation is essential across many sectors, including pharmaceuticals, polymers, mining and chemical industry and food science, it remains one of the most complex to characterize due to the simultaneous heat, mass, and momentum transfer phenomena involved.

Formally, drying is defined as a separation process that converts a liquid or semi-solid feedstock into a solid product through the thermal removal of volatile substances [14]. Unlike mechanical separation techniques such as filtration or centrifugation, drying involves a phase change, specifically the vaporization of a solvent (most commonly water). In specific configurations, such as freeze-drying, this occurs via sublimation below the triple point; however, in most industrial contexts, it involves the convective or diffusive transport of moisture from a product surface into a gaseous medium.

The primary motivations behind drying are twofold: biochemical stability and transport economics. By reducing water content, drying inhibits microbial growth and enzymatic degradation, thereby extending the stability of perishable materials without the need for refrigeration [10]. From a logistics perspective, the reduction in product mass and volume minimizes storage requirements and lowers distribution costs. Furthermore, drying allows for the engineering of specific solid formats, such as free-flowing powders or granules, which are essential for downstream handling and consumer utility [5].

2.1.1 Drying Technologies

Industrial drying technologies are primarily classified by their dominant mode of heat transfer - convective, conductive, or radiative - and further categorized by the hydrodynamics of the material handling system. Given the focus of this work on spray drying systems, convective methods represent the most important category, as they rely on direct contact between a drying medium and the feedstock.

Convective Drying

Accounting for over 85% of industrial applications, convective dryers transfer sensible heat from a flowing gaseous medium to the surface of a wet solid, simultaneously transporting evaporated moisture away from the interface [14]. From a modeling perspective, these systems are characterized by complex gas-solid or gas-liquid momentum exchange.

- **Spray Drying**: This technique transforms suspension into particulate powders in a single continuous step [5]. The process involves the atomization of the liquid into a fine droplet dispersion within a

specialized nozzle. The resulting high surface-area-to-volume ratio yields rapid evaporation rates. Due to short residence times and evaporative cooling effects, it is the industry standard for thermosensitive biological and pharmaceutical products [10].

- **Fluidized Bed Drying**: Designed for granular solids, this technique utilizes an upward-flowing gas stream to suspend particles in a "pseudofluid" state [14]. The intense mixing maximize the interfacial area, resulting in high heat and mass transfer coefficients.

- **Rotary Drying**: High-throughput unit operation engineered for the large-scale thermal dehydration of free-flowing granular materials, crystalline solids, heavy chemicals, and natural ores [14]. It relies on a rotating, slightly inclined cylindrical chamber where the dispersed solid phase is transported axially via gravity and mechanical rotation.

- **Flash Drying**: The slurry is superheated under elevated pressure prior to the injection to the drying chamber where the pressure is significantly lower. The sudden pressure drop across the atomizing orifice induces an immediate adiabatic expansion, using the feed's sensible enthalpy to cause solvent evaporation [4].

Emergence of Superheated Steam Drying

An important sub-classification of convective drying relates to the nature of the drying medium. While air is the traditional drying fluid, Superheated Steam Drying (SSD) has gained significant traction due to its superior energy profile and product quality benefits [7].

In SSD, the air is replaced entirely by superheated steam. Operating in an oxygen-free environment eliminates oxidative degradation, fire risks, and dust explosions [7]. SSD alters the mass transfer physics: since the environment consists of the pure vapor of the solvent, the process is not limited by the resistance to mass transfer as it is the case in diffusion of vapor through an inert gas film. Instead, it is governed by the heat transfer rate to the interface. Usage of superheated steam allows for near-complete recovery of latent heat via condensation, potentially reducing net energy consumption by up to 85% compared to conventional air-based systems [8].

2.2 Spray Drying

2.2.1 Fundamental Principles of Spray Drying

The complexity of spray drying stems from the highly coupled, transient multiphase transport phenomena and morphological phase transitions occurring within the drying chamber. Unlike simpler drying operations, the evolution of a droplet into a solid particle follows a two-stage kinetic mechanism.

Single-Droplet Drying Kinetics

In the first drying period (constant rate period), the liquid droplet undergoes sensible heating toward the equilibrium temperature of the surrounding medium [10]. In conventional air drying, this is the wet-bulb temperature; however, in Superheated Steam Drying, the interface reaches the local boiling point of the solvent [7].

Evaporation proceeds uniformly at the interface, and the droplet shrinks as free solvent vaporizes. This rapid phase change maintains a depressed droplet temperature due to latent heat absorption, protecting thermolabile components. Simultaneously, internal concentration gradients induce species segregation, where solutes with low diffusion coefficients concentrate at the receding interface, altering the surface composition [10].

As the surface moisture falls below a critical threshold, the localized solid concentration supersaturates, initiating the second drying period (falling rate period) [3]. This stage is marked by the formation of a porous solid crust or skin encompassing a wet core. The particle diameter stabilizes, and moisture must now overcome the supplementary mass-transfer resistance of the crust via capillary flow or vapor diffusion.

The reduced evaporation rate causes the particle temperature to elevate sharply toward the bulk gas temperature. If the internal core temperature exceeds the boiling point, internal vapor pressure can lead to particle inflation, fracturing, or puffing, which defines the final powder porosity [10].

The temperature of the particle and the moisture content during the drying operation have been presented in Figure (2.1). In the same figure a simplistic diagram of particle nature across different drying stages was illustrated.

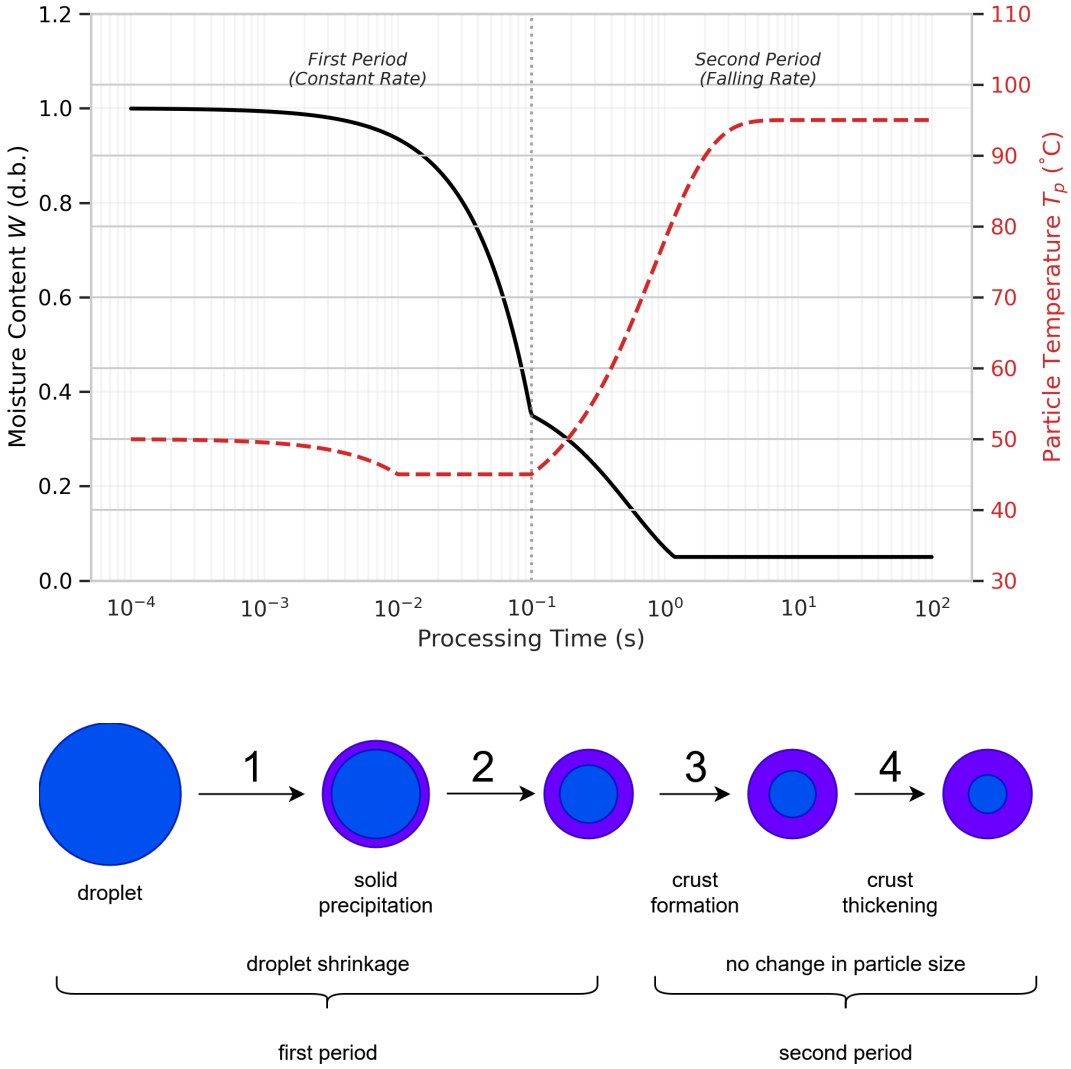


Figure 2.1: Morphological evolution of a droplet during the spray drying process. Stages 1–2 represent the Constant Rate Period characterized by droplet shrinkage. Stages 3–4 represent the Falling Rate Period governed by crust-controlled mass transfer. Redrawn and adapted from [10].

Macroscopic Hydrodynamics and Wall Interactions

Although individual drying kinetics are important, the overall airflow within the chamber decides where the particles travel. As droplets move through the dryer, their spatial trajectories are driven by a combination of aerodynamic drag and turbulent eddies [10, 5]. A primary focus when modeling these systems is accurately predicting how these semi-dried particles interact with the chamber walls.

Whether a particle adheres to the wall or bounces off depends on its glass transition temperature (T_g),

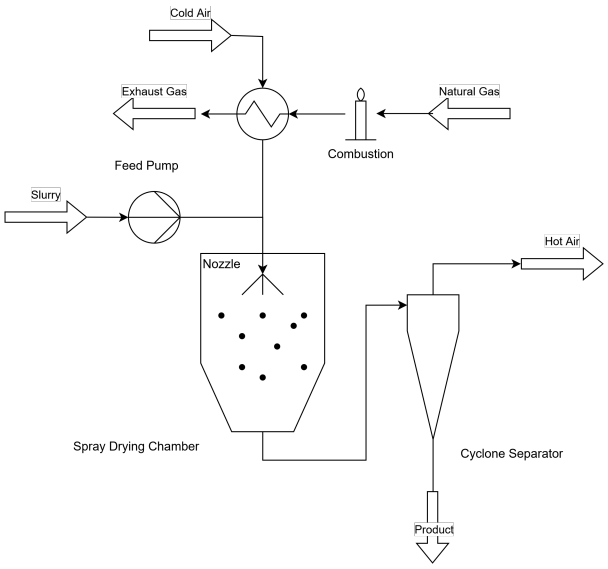
which dynamically changes as the particle loses moisture. This interaction is governed by a specific thermal threshold known as the sticky point:

- **Wall Fouling**: If a particle impacts the wall while its temperature is above the sticky threshold ($T > \Delta T + T_g$), it remains in a cohesive, rubbery state and sticks to the surface, resulting in wall fouling.
- **Elastic Rebound**: Conversely, if the particle has dried sufficiently, it transitions into a hard, glassy state. This allows it to bounce off the wall elastically, preventing accumulation and increasing the final powder yield [10].

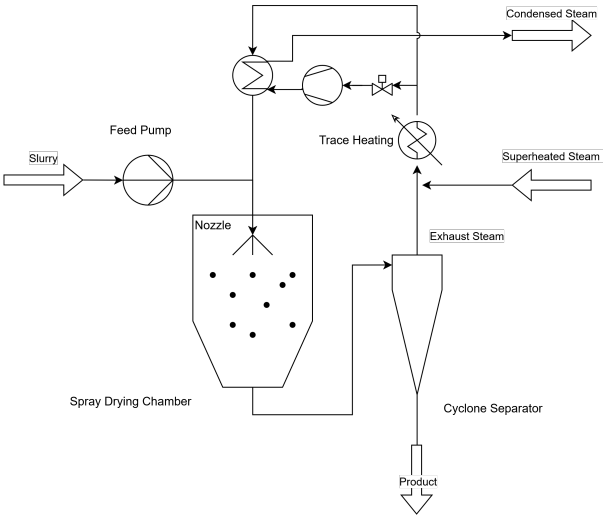
Beyond wall collisions, the internal hydrodynamics influence how often particles interact with each other. In many industrial applications, small, under-dried particles are reinjected into the atomization zone. When these fines collide with freshly injected droplets, they stick together and promote structural agglomeration [15].

2.2.2 Spray Dryer Design

A standard industrial spray dryer architecture consists of several integrated subsystems, the configuration of which dictates the hydrodynamic environment within the vessel. Comparison between a conventional and superheated steam spray drying system is presented in Figure (2.2).



(a) Schematic of an open-loop conventional air spray drying system.



(b) Schematic of a superheated steam spray drying system featuring a closed-loop steam recirculation and mechanical vapor recompression.

Figure 2.2: Comparison between conventional and superheated steam spray drying systems.

Feed and Atomization Systems

The feed system is composed of a storage tank, filtration units, a high-pressure delivery pump, and the atomizing device [10]. Atomization is the key phase of the process, as it governs the transition from a bulk fluid to a highly dispersed droplet cloud, creating large interfacial area required for rapid heat and mass transfer [5].

From a modeling perspective, the atomizer defines the source terms for the discrete phase. It determines the initial droplet size distribution, the spray pattern (cone angle), and the initial velocity vectors of the particles [5, 10]. These parameters are the primary determinants of particle morphology, residence time, and the likelihood of wall impingement.

Industrial spray drying rely on four standard atomization technologies. Each utilizes distinct physical phenomena to overcome fluid surface tension and viscous forces.

Rotary (Centrifugal or Wheel) Atomizers rely on centrifugal energy to disintegrate the fluid. Feedstock is fed into a disc rotating at 10,000 to 30,000 rpm, where it is accelerated radially and sheared into droplets at the periphery [10]. This results in a broad, horizontal spray (approaching 180°), requiring wide-diameter drying chambers to prevent premature wall deposition [5].

Pressure (Single-Fluid) Nozzles convert hydrostatic pressure (5–7 MPa) into kinetic energy. The fluid is forced through a swirl core, exiting as a thin, unstable liquid film that shatters into a hollow-cone spray [5]. These produce narrower spray angles (40°–140°), making them suitable for tall-form dryer geometries.

Pneumatic (Two-Fluid) Nozzles utilize high-velocity gas to induce aerodynamic shear and liquid breakup. While energy-intensive due to the requirements for compressed air or steam, they allow for precise control of the gas-to-liquid ratio to manipulate the resulting droplet size [10]. In the context of Superheated Steam Drying, the atomizing gas can also be steam, maintaining the pure-vapor environment of the chamber.

Ultrasonic Atomizers represent a specialized solution for non-Newtonian or highly viscous fluids. High-frequency acoustic vibrations and cavitation disrupt the fluid into uniform droplets, avoiding the "stringing" or filament formation common with polymer-heavy feedstocks [10].

Drying Medium Conditioning and Distribution

The gas handling subsystem is responsible for conditioning and transporting the drying medium, ensuring it possesses the required thermal energy and aerodynamic momentum to facilitate multiphase heat and mass transfer [5]. In conventional systems, this integrates solid-gas separation via cyclones and bag-house filters, mechanical propulsion via centrifugal fans, and thermal energy addition. In conventional systems natural gas is burned to heat up cold air before directing it towards the drying chamber [2].

For SSD, this subsystem instead involves a steam generator and a recirculation loop. The evaporation of water continuously adds mass to the continuous phase. To maintain balance, a dedicated bypass loop with a condenser is required. Frequently mechanical vapor recompression systems are inserted in the recirculation loop to elevate the specific enthalpy and pressure of the exhaust steam for upstream use [7].

The air disperser is a vital component of this subsystem, as it defines the boundary conditions for the continuous phase. The geometric configuration of the disperser dictates the macroscopic hydrodynamic regime, typically co-current, counter-current, or mixed flow, which determines the thermal history and residence time of the discrete phase[5].

Drying Chamber

The drying chamber is a control volume where rapid multiphase heat and mass transfer occurs. Its geometric and aerodynamic design dictates the drying kinetics and the final product morphology.

Geometrically, the chamber dimensions must be designed to integrate the specific spray angle, droplet size distribution, and initial kinetic velocity generated by the atomizer. Inadequate chamber volume relative to these injection parameters leads to severe wall fouling, localized product degradation, and substantially reduced powder yield [5]. The chamber walls represent boundary conditions where particle-wall interactions, such as reflection, accretion, or film formation, occur.

In industrial practice, chambers are classified by their aspect ratio (H/D) into short-form and tall-form designs. Tall-form units generally exhibit more directed, plug-flow-like patterns, whereas short-form units often involve complex recirculating flows that increase residence time but complicate numerical convergence. The base of the chamber is typically conical, serving as the terminal drying zone [5].

Powder Recovery and Exhaust Systems

The exhaust system is responsible for the separation of the dried solid phase from the continuous gas medium. While the primary discharge of coarse product typically occurs at the chamber's conical base, finer fractions remain entrained and are subsequently recovered via downstream high-efficiency cyclone separators or baghouse filters [5].

From a fluid dynamics perspective, the conical base functions as an aerodynamic classifier. The separation efficiency is governed by the competition between gravitational/inertial forces and aerodynamic

drag. Coarser, heavier agglomerates possess sufficient inertia to overcome the gas drag, disengaging from the flow field to be collected at the apex. Conversely, finer particles with lower Stokes number, which is the primary dimensionless parameter characterizing how suspended particles respond to carrier fluid structure, follow the gas streamlines and exit the chamber via the exhaust duct.

Mathematically the Stokes number is defined as the ratio of the characteristic particle response time to the characteristic time scale of the fluid flow. Low Stokes number indicate that particles responds almost instantaneously to local fluid velocity changes, following streamlines perfectly.

2.3 Superheated Steam Spray Drying

Superheated steam drying is a unit operation where steam replaces conventional hot air or inert gases as both the convective heat transfer medium and the moisture carrier [7]. In an SSD system, the slurry is atomized directly into a high-temperature steam environment. Because the exhaust from the drying chamber consists almost entirely of pure solvent vapor, the system is typically engineered as a closed-loop circuit.

In this configuration, a portion of the exhaust is continuously bled from the system, while the remainder is thermally or mechanically upgraded and recirculated back into the drying chamber [8]. This allows for the near-complete recovery of latent heat, which is otherwise lost to the atmosphere in conventional air-drying systems. Furthermore, the exclusion of oxygen from the computational and physical domain alters the transport kinetics, shifting the process from a diffusion-limited mechanism to one governed by the rate of heat addition to the interface.

The adoption of SHS technology is primarily driven by the necessity to mitigate the massive thermal energy footprint inherent to industrial spray drying. While conventional air-based dryers typically exhibit specific energy consumption between 4 and 6 MJ per kilogram of water evaporated, integrated SHS systems can recover the latent heat of vaporization via condensation. This recovery potential can theoretically reduce net energy requirements by up to 85% compared to open-loop systems [8].

Beyond thermal efficiency, SHS systems operate in an oxygen-free environment. This exclusion of oxygen eliminates the risk of dust explosions and fire hazards, enhancing plant safety. Furthermore, the absence of an oxidizing atmosphere prevents the oxidative degradation of sensitive bioactive or chemical components. From an environmental perspective, SSD allows for near zero-emission operation; because the process vapor is condensed rather than vented, particulate fines and volatile organic compounds are captured in the condensate rather than released into the atmosphere [7].

From a product engineering standpoint, SHS produces a distinct end-product morphology. The rapid vaporization and internal pressure build-up within the droplet during the falling rate period lead to structural inflation. This mechanism results in highly porous, spherical particles with superior rehydration capabilities [8].

Despite its thermodynamic superiority, SHS spray drying is not universally applicable and is highly material-dependent. The primary constraint is the thermal sensitivity of the feedstock. In conventional air drying, the droplet surface temperature is governed by evaporative cooling, which maintains the material at the wet-bulb temperature [14]. Conversely, in atmospheric SHS drying, the droplet rapidly heats up to the saturation temperature of the solvent (100°C for water) during the constant-rate period [14].

As a consequence, materials that undergo undesirable phase transitions, denaturing, or chemical degradation at these elevated temperatures cannot be processed in atmospheric SHS systems [7]. While conducting the process under sub-atmospheric pressures can lower the boiling point, this configuration significantly increases the specific volume of the steam and the capital cost of the vacuum-handling equipment, potentially negating the energy efficiency benefits.

From an operational and capital expenditure perspective, SHS systems exhibit higher complexity than conventional air-based units. To prevent uncontrolled steam condensation, the drying chamber and downstream hardware must be heavily insulated or actively heated to maintain surface temperatures above the saturation point [8]. Furthermore, product discharge requires high-integrity rotary valves or double-flap systems to prevent air infiltration, which would compromise the purity of the steam loop and reduce the efficiency of the latent heat recovery [8].

2.3.1 Superheated Steam Kinetics

The drying kinetics in an SHS environment deviate from conventional hot-air systems due to the absence of a non-condensable gas phase. The temporal evolution of the material undergoes three principal kinetic regimes [8], as illustrated in Figure (2.3).

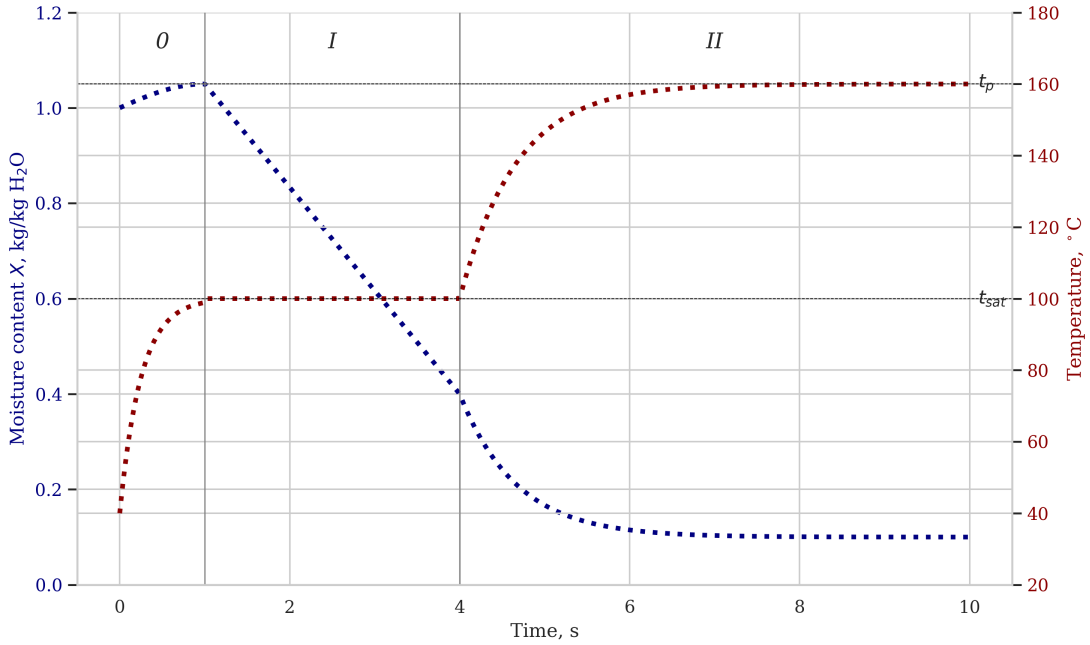


Figure 2.3: Superheated steam drying (SSD) curves for a liquid droplet. The relationship between moisture loss and thermal history is shown across the constant rate (I) and falling rate (II) periods. Redrawn and adapted from [8]

Stage 0: Initial Condensation and Heating

When the ambient-temperature feedstock is injected into the high-enthalpy steam environment, sensible heating is accompanied by the immediate condensation of steam onto the cold droplet surface. This results in a transient increase in the droplet mass and moisture content. The latent heat released during condensation rapidly elevates the material temperature until it reaches the saturation temperature (T_{sat}) corresponding to the local operating pressure [9].

Stage I: Constant Drying Rate Period

Once the droplet reaches T_{sat}, the evaporation of unbound moisture proceeds isothermally, as shown in Figure (2.3). In this pure-vapor environment, moisture removal does not occur via binary molecular diffusion through an inert gas film [9]. Instead, the kinetics are purely heat-transfer-controlled, effectively functioning as a boiling mechanism where the evaporation rate is proportional to the heat flux provided by the superheated steam. Furthermore, the critical moisture content (X_c) marking the end of this stage is typically lower than in hot-air drying due to the elevated thermal driving force and enhanced internal moisture mobility [8].

Stage II: Falling Drying Rate Period

As the surface moisture is depleted and a solid crust begins to form, the removal of bound moisture commences [8]. During this falling rate period, the macroscopic evaporation rate decelerates, causing the

particle temperature to elevate above the saturation point toward the bulk steam temperature (T_p). The absence of external diffusional resistance, combined with high operating temperatures, frequently allows for significantly faster drying rates during this period compared to conventional air-based systems [8].

Inversion Temperature

The relative kinetic efficiency of SHS versus conventional air drying is governed by a thermodynamic threshold known as the inversion temperature [9]. This is the specific thermal setpoint at which the moisture evaporation rate becomes independent of the drying medium's composition, yielding identical performance in pure steam and air [8]. The crossover of these kinetic rates is graphically represented in Figure (2.4).

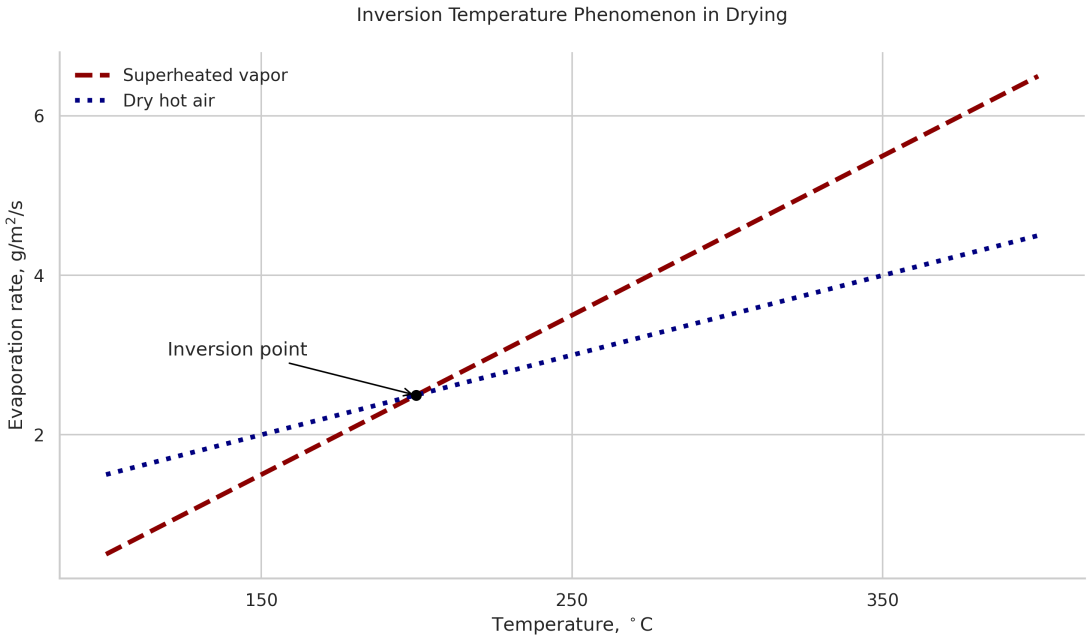


Figure 2.4: Comparison of evaporation rates between dry hot air and superheated vapor as a function of temperature. Redrawn and adapted from [8]

Below the inversion temperature, the evaporation rate in SHS is lower than in convective hot air. This is due to the lack of a partial pressure gradient and the "temperature plateau" at the boiling point, which limits the thermal driving force. Conversely, above the inversion temperature, the superior thermophysical transport properties of steam — specifically its higher heat capacity and improved radiative heat transfer — compensate for the reduced temperature gradient. For water-based systems at atmospheric pressure, this inversion point is typically found between 160° C and 200° C, making SHS particularly effective for high-temperature industrial applications where rapid drying kinetics are required [8].

2.3.2 Challenges in Numerical Modeling of SHS Environments

Simulating SHS spray drying via Computational Fluid Dynamics introduces several specific mathematical and physical modeling challenges that differentiate it from standard air-based simulations.

Absence of Mass Diffusion Gradients

In a pure SHS environment, the absence of a non-condensable gas eliminates the concentration gradient required for binary molecular diffusion. Consequently, the standard mass-transfer correlations used in air-drying models are inapplicable. Instead, evaporation is purely heat-transfer-controlled; this necessitates

modifying the discrete phase source terms to ensure that the vaporization rate is dictated strictly by the heat flux, typically calculated via the Ranz-Marshall correlation for the Nusselt number [12].

Aerodynamic Drag and Trajectory Deviations

Superheated steam possesses a lower dynamic viscosity compared to air at equivalent temperatures, which alters the aerodynamic drag forces acting on the discrete phase. CFD simulations must accurately resolve these modified momentum exchange terms, as the reduced drag allows droplets — particularly those with higher inertia — to maintain their initial trajectories longer. This often results in premature wall impingement if the chamber geometry or the gas disperser is not specifically optimized for the SHS flow field [8].

Initial Condensation Kinetics

The transient stage of steam condensation onto the cold droplet surface is mathematically complex to resolve within a Lagrangian-Eulerian framework. Many simplified models neglect this mass-gain period, assuming immediate evaporation at the constant rate. However, a high-fidelity CFD model must account for the latent heat of condensation released into the droplet and the resulting transient increases in diameter and mass to accurately predict the early-stage particle trajectories [8].

Thermophysical Property Dependencies

The modeling of the continuous phase requires the implementation of precise polynomial correlations for the density, specific heat, thermal conductivity, and dynamic viscosity of SHS. Because near-saturation steam behavior deviates from the ideal gas law, these temperature-dependent properties are important for capturing the correct heat transfer coefficients and gas-phase buoyancy effects within the drying chamber [16].

Chapter 3

Physical and Mathematical Modeling

Mathematical modeling of spray drying operations necessitates a multi-scale formulation to resolve the highly coupled transport phenomena - specifically momentum, heat, and mass transfer - occurring between the continuous gaseous drying medium and the discrete particles [17]. For detailed spatial resolution and system design, multi-dimensional CFD frameworks are employed to solve the governing partial differential equations for mass, momentum, and energy conservation [11]. Within the CFD environment, the mathematical treatment of multiphase flow leads to three primary architectures:

- **Eulerian-Eulerian (Two-Fluid) Approach**: Both phases are mathematically treated as interpenetrating continua. The governing equations are formulated using averaging techniques, making this approach suitable for dense multiphase systems where particle-particle interactions dominate [13].
- **Eulerian-Lagrangian (Discrete Phase) Approach**: This is the most predominant framework for spray drying, which typically exhibits a dilute particle loading. The continuous gas phase is resolved in a fixed Eulerian reference frame, while the dispersed phase is tracked individually as "parcels" in a Lagrangian reference frame [18].
- **Interface Tracking Methods**: Utilized for highly localized, small-scale phenomena such as primary atomization and liquid jet breakup, where the interface between liquid and gas must be explicitly resolved [10].

This work utilizes the Eulerian-Lagrangian approach for modeling the macroscopic multiphase interactions within the spray dryer. At the microscopic level, specialized mathematical sub-models govern the droplet drying kinetics and morphological evolution. These kinetic models divide the droplet history into a constant-rate evaporation period governed by surface convective transport, followed by a falling-rate period characterized by solid crust formation and internal transport resistance.

3.1 Governing Equations for the Continuous Phase

In the Eulerian-Lagrangian framework, the behavior of the continuous fluid medium is mathematically resolved by treating it as a continuum within a fixed spatial Eulerian coordinate system, while simultaneously interacting with the discrete phase [13]. The macroscopic hydrodynamics and thermodynamics of the primary phase are described by the time-averaged conservation equations of mass, momentum, thermal energy, and species transport [9]. In process engineering applications such as spray drying, these are typically formulated as the Reynolds-Averaged Navier-Stokes (RANS) equations to balance computational efficiency with the resolution of turbulent transport [19].

To accurately resolve the coupled momentum, heat, and mass transfer mechanisms inherent to multiphase processes, these continuum Eulerian equations are augmented by distributed volumetric source terms. These terms represent the exchange of mass, momentum, and energy between the steam and the tracked Lagrangian parcels [9].

3.1.1 Conservation of Mass

The conservation of mass for the continuous phase — often referred to as the continuity equation — dictates the temporal and spatial evolution of the fluid density. Within the Eulerian-Lagrangian framework, this equation is augmented by a source term to account for the mass added to the steam phase via droplet evaporation:

$$\frac{\partial \rho}{\partial t} + \nabla \cdot (\rho \vec{u}) = S_m \tag{3.1}$$

In Equation (3.1), $\vec{u}$ represents the continuous phase velocity vector, and S_m is the interphase mass source term representing the summation of the vaporization rates from all discrete droplets within a given computational control volume [19].

In the specific context of SSD, the source term S_m is uniquely characterized. Unlike conventional air-drying, where mass transfer is driven by a vapor concentration gradient, the evaporation in a pure steam environment is governed strictly by the balance of heat transfer to the droplet interface. As a consequence, S_m is determined by the rate at which the superheated steam supplies the latent heat required for vaporization [12].

3.1.2 Conservation of Momentum

The momentum transport equation — the RANS formulation — resolves the continuous velocity field subject to pressure gradients, viscous stresses, and the bidirectional momentum coupling with the discrete phase:

$$\frac{\partial (\rho \vec{u})}{\partial t} + \nabla \cdot (\rho \vec{u} \vec{u}) = -\nabla p + \nabla \cdot \bar{\bar{\tau}} + \rho \vec{g} + \vec{F} + S_{\text{mom}} \tag{3.2}$$

In Equation (3.2), p is the static pressure, $\bar{\bar{\tau}}$ is the effective stress tensor (incorporating both molecular and turbulent viscosity components), and $\vec{g}$ is the gravitational acceleration vector. The term $\vec{F}$ signifies the external body force exerted by the dispersed phase onto the gas due to aerodynamic drag, while S_{mom} accounts for the specific momentum transferred into the continuous phase resulting from the mass flux of the evaporating solvent [19].

3.1.3 Conservation of Energy

Thermal energy transfer within the continuous phase is resolved by accounting for convective transport, conductive diffusion, viscous dissipation, and the enthalpy exchange with the discrete phase. The general conservation equation for the total energy, E, is formulated as:

$$\frac{\partial (\rho E)}{\partial t} + \nabla \cdot [\vec{u}(\rho E + p)] = \nabla \cdot \left[\left(\kappa + \frac{c_p \mu_t}{\text{Pr}_t} \right) \nabla T - \sum_i h_i \vec{J}_i + \bar{\bar{\tau}} \cdot \vec{u} \right] + S_E \tag{3.3}$$

In Equation (3.3), E represents the specific internal energy (or total enthalpy), T is the gas temperature, κ is the thermal conductivity, and the fraction $c_p \mu_t / \text{Pr}_t$ represents the turbulent thermal conductivity, which is closed via the specific heat capacity c_p, the turbulent dynamic viscosity μ_t, and the turbulent Prandtl number Pr_t. The terms $\vec{J}_i$ and h_i are the diffusive flux and specific enthalpies of species i. The term $\bar{\bar{\tau}} \cdot \vec{u}$ represents the viscous dissipation within the continuous phase, quantifying the irreversible conversion of kinetic energy into internal thermal energy due to the fluid friction. Normally this term is not significant and can be omitted. The volumetric source term S_E represents the rate of thermal energy transferred to the continuous fluid, which encompasses the sensible convective heat transferred to the droplets as well as the latent heat extracted from the gas to drive solvent vaporization [19].

For the specific case of SSD, the energy conservation is more effectively cast in terms of the specific enthalpy of the steam, H. Since the medium consists of a single pure vapor phase, the species diffusion flux ($\vec{J}_i$) is eliminated, simplifying the transport to:

$$\frac{\partial (\rho H)}{\partial t} + \nabla \cdot (\rho \vec{u} H) = \left(\kappa + \frac{c_p \mu_t}{\text{Pr}_t} \right) \nabla T + \frac{\partial p}{\partial t} + \nabla \cdot (p \vec{u}) + S_E \tag{3.4}$$

The pressure terms in Equation (3.4) represent the transient pressure work and the reversible flow work exerted within the control volume [12]. When the energy conservation equation is cast in terms of the specific enthalpy of the gas phase, rather than total internal energy, the mechanical work performed by the fluid must be explicitly resolved to maintain a thermodynamic balance [12].

3.1.4 Equation of State and Transport Properties

The three macroscopic conservation equations for mass, momentum, and energy are mathematically unclosed and insufficient to completely describe the behavior of a superheated steam continuous phase. To achieve closure within the Eulerian framework, these partial differential equations must be coupled with a thermodynamic Equation of State alongside constitutive models for transport and caloric properties [20].

The necessity of Equation of State (EoS)

The primary phase conservation equations resolve system variables (velocity, pressure and enthalpy), but they require precise inputs for local density, specific heat capacity, dynamic viscosity, and thermal conductivity to compute convective fluxes, viscous dissipation, and interphase heat transfer [12].

Because SHS in industrial dryers frequently operates in near-saturation regimes or under varied pressure conditions, its thermodynamic behavior deviates from ideality, meaning its compressibility factor (Z) diverges from unity [21]. Assumption of ideal gas behavior under these conditions may lead to errors. Therefore, an EoS is necessary to map $p - V - T$ (pressure-volume-temperature) surface and update the fluid density and thermodynamic state at every computational iteration. There are several proposed EoS available in the literature, each with own strengths and drawbacks.

Ideal Gas Equation

In many macroscopic CFD spray drying simulations operating at low to moderate pressures, the continuous medium is treated as an ideal gas [22, 12].

The equation of state is formulated simply as:

$$p = \rho R T \tag{3.5}$$

In Equation (3.5), R represents the ideal gas constant. Usage of this equation imposes the absolute minimum computational load on the CFD solver, ensuring quick convergence and stability [20]. It is sufficient for high temperature, low-pressure gas flows where the compressibility factor remains close to unity.

The ideal gas assumption fails when applied to condensable continuous media (like SHS near the saturation dome) or in systems with wide pressure gradients. It cannot predict real-gas compression, expansion work, or phase change boundaries.

Analytical (Cubic) Equations of State

Cubic equations of state, such as the Peng-Robinson or Soave-Redlich-Kwong models, are standard models for real-gas CFD simulations, used to predict fluid properties in both single-phase and two-phase regions [20].

All cubic equations can be generalized into a fractional form:

$$p = \frac{RT}{V_{\text{mol}} - b} - \frac{a_c \alpha(T_R, \omega)}{V_{\text{mol}}(V_{\text{mol}} + b) + b(V_{\text{mol}} - b)} \tag{3.6}$$

In Equation (3.6), V_{mol} is the molar volume, T_R is the reduced temperature, ω is the Pitzer acentric factor, and a_c and b account for attractive forces and excluded molecular volume, respectively [20].

Cubic EoS represent an effective engineering compromise between mathematical simplicity and thermodynamic accuracy. The roots of the EoS can be found analytically, avoiding iterative numerical root-finding algorithms during the CFD flow field resolution [21].

Cubic models systematically mispredict non-classical phenomena near the vapor-liquid critical point. Standard implementations of Peng-Robinson equation in CFD codes like OpenFOAM are incapable of accurately calculating liquid-phase densities without applying complex volume translations [20].

Multiparameter Helmholtz-Energy Explicit Models

When spray drying operations involve complex real fluids, severe pressure drops, or require high precision near saturation, standard CFD codes must be augmented with high-fidelity multiparameter EoS libraries, such as CoolProp [20].

These models are explicit in the reduced Helmholtz energy (α) which is partitioned into an ideal gas contribution (α^0) and a residual real fluid contribution (α^r):

$$\alpha = \alpha^0 + \alpha^r$$

All macroscopic thermodynamic properties are derived via exact analytic differentiation of the above term [20]. These formulations yield best level accuracy and are capable of accurately predicting properties for dense liquids, phase changes,and the critical regions where cubic models fail [20].

However, the computational demand is significant; a single direct call to a Helmholtz explicit EoS can be up to 20 times slower than a Peng-Robinson calculation [20]. To make these models viable for transient CFD simulations, it is necessary to bypass direct evaluation and instead utilize optimized tabular interpolation methods.

Transport Properties

In CFD modeling of multiphase operations, the continuous phase transport and caloric properties are routinely parametrized as temperature dependent polynomial functions [23].

A typical constant-pressure polynomial regression correlates the target transport property (ϕ) as a function of local absolute temperature T [21]:

$$\phi(T) = a_0 + a_1 T + a_2 T^2 + a_3 T^3 + a_4 T^4 \tag{3.7}$$

Depending on the specific fluid and the required thermal envelope, the polynomial order in Equation (3.7) is truncated to optimize the computational load. For pure SHS applications, transport properties are typically defined via higher-order polynomials directly generated by interpolating standardized empirical thermodynamic steam tables over the expected operating bounds [12, 16].

These polynomial equations are precise provided the system operates within the specific pressure and temperature boundaries of the regressed data. However, the polynomials are incapable of capturing complex thermodynamic phenomena. They lack accuracy when the control volume is subjected to operations adjacent to phase-change boundaries [20]. Because they depend solely on temperature, they are inadequate for modeling real-gas compression, near critical fluids, or severe compressible flow regimes.

Integrating high-fidelity models to accurately resolve transport properties imposes a massive computational penalty. Direct calls to advanced libraries can inflate the physical duration of a single CFD time step several times compared to simple algebraic evaluations [20]. Utilizing polynomials for viscosity, specific heat, and thermal conductivity represents the standard compromise, allowing for quick solver convergence and preserving macroscopic accuracy without the prohibitive computational overhead associated with exact real-gas formulation [20].

3.2 Turbulence Modeling

Industrial spray drying operations operate under highly turbulent flow conditions. These regimes are characterized by large volumetric flow rates, complex chamber geometries, swirl generators and high velocity atomization jets, frequently exceeding 70 m/s at the nozzle exit [12]. Within the Eulerian-Lagrangian multiphase framework, an accurate turbulence model for the continuous phase is physically and mathematically essential for three fundamental reasons:

1. Turbulence strictly dictates the macroscopic hydrodynamics of the drying medium. The spatial momentum distribution governs the formation of central down-flowing jets, boundary layer separation, and large-scale turbulent recirculation zones, which define the thermodynamic history and bulk residence time of the discrete phase [18].

2. The stochastic dispersion of the secondary phase is driven by local turbulent velocity fluctuations. Failing to model turbulence effectively neutralizes mathematical submodel like the Discrete Random Walk, resulting in mispredictions of droplet trajectories,localized concentration gradients, and premature particle-wall impingement [24].

3. Turbulent kinetic energy intensifies the interphase convective transport; highly turbulent eddies compress the boundary layer surrounding the droplet, elevating the heat and mass transfer kinetics during solvent evaporation [18].

To achieve mathematical closure of unclosed Reynolds stress tensor in Equation (3.2), engineers predominantly rely on the RANS framework [11]. This approach represents the optimal compromise. In this work two turbulence models are of particular interest.

3.2.1 The $k-\epsilon$ Turbulence Model

The standard $k-\epsilon$ model computes the spatial and temporal evolution of the turbulent kinetic energy (k) and its volumetric dissipation rate (ϵ) [17]. The assumption of this model is that the flow is fully turbulent and molecular viscosity effects are negligible.

The governing transport equations are formulated as:

$$\frac{\partial(\rho k)}{\partial t} + \nabla \cdot (\rho \vec{u} k) = \nabla \cdot \left[\left(\mu + \frac{\mu_t}{\sigma_k} \right) \nabla k \right] + G_k + G_b - \rho\epsilon - Y_M + S_k$$

$$\frac{\partial(\rho \epsilon)}{\partial t} + \nabla \cdot (\rho \vec{u} \epsilon) = \nabla \cdot \left[\left(\mu + \frac{\mu_t}{\sigma_\epsilon} \right) \nabla \epsilon \right] + C_{1\epsilon} \frac{\epsilon}{k} (G_k + C_{3\epsilon} G_b) - C_{2\epsilon} \rho \frac{\epsilon^2}{k} + S_\epsilon$$

Here, ρ is density, $\vec{u}$ is the velocity vector, μ is molecular viscosity, G_k and G_b represent the generation of turbulent kinetic energy due to velocity gradients and buoyancy, Y_M accounts for compressibility corrections, and S terms are user-defined sources [17]. The turbulent eddy viscosity is subsequently closed via the algebraic relation:

$$\mu_t = \rho C_\mu \frac{k^2}{\epsilon}$$

where C_μ is a calibration constant.

3.2.2 The $k-\omega$ Turbulence Model

To rectify the structural deficiencies of $k-\epsilon$ formulation in near-wall regions, the $k-\omega$ substitutes the dissipation rate equation equation with a transport equation for the specific dissipation rate (ω), which defines the rate at which turbulent kinetic energy is converted into thermal internal energy ($\omega = \epsilon/(C_\mu k)$) [11].

The ω transport equation is formulated as:

$$\frac{\partial(\rho \omega)}{\partial t} + \nabla \cdot (\rho \vec{u} \omega) = \nabla \cdot \left[\left(\mu + \frac{\mu_t}{\sigma_\omega} \right) \nabla \omega \right] + G_\omega - Y_\omega + S_\omega + G_{\omega b} + D_\omega$$

In this framework, G_ω represents the generation of ω, Y term represents the turbulent dissipation, and D_ω is a cross-diffusion modification [22]. The turbulent eddy viscosity is evaluated as:

$$\mu_t = \rho \frac{k}{\omega}$$

3.2.3 Model Adequacy and Selection

Spray drying chambers represent highly heterogeneous fluid dynamic environments, characterized by complex hydrodynamic behavior. Resolving all transient micro-scales of turbulence imposes an intractable

computational overhead, making them impractical for routine industrial design and scaling [17]. The two-equation RANS models provide optimal compromise, ensuring accurate solution at a viable computational cost.

The $k-\epsilon$ family is particularly useful for the bulk flow and free shear jets and is the industrial workhorse for spray drying [18]. However, since these models rely on an isotropic eddy viscosity assumption, they systematically fail to accurately predict boundary layer phenomena or low-velocity viscous sublayers.

The $k-\omega$ family is capable of accurately predicting near-wall hydrodynamics and flow separation. Prediction of the near-wall turbulent behavior is vital in spray drying as it governs the stochastic dispersion of droplets toward the chamber walls, directly dictating wall deposition and fouling rates [18]. The standard $k-\omega$ provides superior resolution of viscous sublayers and boundary layers without requiring complex empirical damping functions.

To overcome mathematical sensitivity of $k-\omega$ model to free-stream boundaries, engineers deploy the Shear Stress Transport (SST) $k-\omega$ variant. The SST model utilizes a mathematical blending function to enforce $k-\omega$ equations in the inner viscous sublayers while transitioning to the $k-\epsilon$ formulation in the free-stream drying medium [18].

Furthermore, these Eulerian turbulence models are required to parametrize the Discrete Random Walk models within the Lagrangian framework. The local values of k dictate the standard deviation of velocity fluctuations used to perturb the deterministic droplet trajectories, while ϵ dictate the eddy lifetime [24]. Therefore, accurate resolution of these two-equation models is a prerequisite for correctly predicting stochastic droplet dispersion, mean residence times, and the spatial distribution of interphase heat and mass transfer [25].

3.3 Discrete Phase Modeling

Within the Eulerian-Lagrangian multiphase framework, the discrete dispersed phase is modeled by tracking individual computational entries through the continuous fluid continuum by integrating Newton's second law of motion, presented in Equation (3.8) [9].

$$m_p \frac{d^2\vec{r}}{dt^2} = \sum \vec{F} \tag{3.8}$$

In Equation (3.8), m is the particle mass, $\vec{r}$ is the position vector, and $\sum \vec{F}$ represents the net force acting on the particle.

Due to the computational intractability of resolving millions of individual physical droplets, engineers normally deploy the Discrete Parcel Method. In this methodology, the spray is discretized into computational parcels, where each parcel represents a statistically significant cluster of physical droplets possessing identical physical properties, such as size, mass, velocity and temperature [26].

The spatial trajectories and thermodynamic states of these parcels are calculated iteratively, and their interaction with continuous phase may be resolved via two-way coupling mechanisms. This mathematically enforces the exchange of mass, momentum, and thermal energy through distributed volumetric source terms injected back into the Eulerian governing equations of the gas phase [19].

3.3.1 Forces Acting on a Particle

The $\sum \vec{F}$ term in Equation (3.8) represents the summation over different forces acting on a particle. It may be expanded as:

$$\sum \vec{F} = \vec{F}_D + \vec{F}_g + \vec{F}_b + \vec{F}_{vm} + \vec{F}_P + \vec{F}_B + \vec{F}_L + \vec{F}_{\text{other}}$$

The individual force vectors governing the particle's trajectory are defied as follow:

Aerodynamic Drag Force ($\vec{F}_D$)

The drag force constitutes the primary resistance exerted on the particle due to the relative velocity between the discrete phase and the continuous fluid. For a spherical particle, it is expressed as:

$$\vec{F}_D = \frac{1}{8}\pi d_p^2 \rho_f |\vec{u}_f - \vec{u}_p|(\vec{u}_f - \vec{u}_p) \tag{3.9}$$

In Equation (3.9), d_p is the particle diameter, ρ_f is the continuous fluid density, $\vec{u}_f$ is the local fluid velocity vector, and $\vec{u}_p$ is the particle velocity vector.

The drag coefficient (C_D) is typically evaluated using empirical correlations dependent on the particle Reynolds number (Re_p), such as the Schiller-Naumann correlation [27]:

$$C_D = \frac{24}{\mathrm{Re}_p}(1 + \mathrm{Re}_p^{0.687}) \quad \text{for} \quad \mathrm{Re}_p < 800$$

Gravitational and Buoyancy Forces ($\vec{F}_g + \vec{F}_b$)

The net body force driving the downward trajectory is the combination of the gravitational acceleration and the opposing fluid buoyancy, mathematical defined as [28]:

$$\vec{F}_g + \vec{F}_b = \frac{\pi d_p^3}{6}(\rho_p - \rho_f)\vec{g} \tag{3.10}$$

Virtual Mass Force ($\vec{F}_{vm}$)

When a particle accelerates relative to the continuous phase, it must overcome the inertia of the surrounding fluid boundary layer. This added mass force is calculated as [9]:

$$\vec{F}_{vm} = \frac{\pi d_p^3}{12}\rho_f \left(\frac{Du_f}{Dt} - \frac{du_p}{dt}\right) \tag{3.11}$$

Pressure Gradient Force ($\vec{F}_P$)

Macroscopic pressure gradients and shear stresses within the continuous fluid impart and additional force on the discrete phase. Assuming constant shear across the particle surface, this is calculated as [9]:

$$F_P = \frac{1}{6}\pi d_p^3 \rho_f \frac{Du_f}{Dt} \tag{3.12}$$

Basset History Force ($\vec{F}_B$)

The Basset force accounts for the temporal delay in the development of the viscous boundary layer around the particle as the relative velocity fluctuates. It relies on a complex convolution integral over the particle's entire trajectory history:

$$\vec{F}_B = \frac{3}{2} d_p^2 \rho_f \sqrt{\pi \nu_f} \int_0^t \Phi(\tau) d\tau \tag{3.13}$$

In Equation (3.13), ν_f indicates the kinematic viscosity of the fluid.

Transverse Lift Forces ($\vec{F}_L$)

Particles subjected to severe velocity shear gradients or rotational dynamics experience lift forces. The Saffman shear lift force is driven by non-uniform pressure distribution across the particle surface in shear flow, while the Magnus lift force is induced by particle rotation [9].

Other forces ($\vec{F}_{\mathbf{other}}$)

This term encapsulates all other forces acting on the particle.

3.3.2 Significant Forces in CFD

While the theoretical force balance is extensive, calculating every vector imposes an impractical computational load. Forces exerting negligible influence on the particle trajectory should be omitted.

The reasoning behind this simplification is based on the density ratio between the dispersed and the continuous phase. In typical spray dryer, the density of the liquid droplet is several orders of magnitude greated than the density of the drying medium, yielding a ratio (ρ_f/ρ_p) on the order of 10^{-3} [10].

Because the $\vec{F}_{vm}$, $\vec{F}_P$, and $\vec{F}_B$ forces are directly proportional to the fluid density or rely on the displacement of the fluid mass, their magnitudes are small compared to particle's inertia. As a consequence, the fluid displacement forces can be discarded [10].

Furthermore, as the discrete droplets are typically in the range from 10 to 200 μm, they exceed the submicron scales where Brownian forces become relevant. Similarly, Saffman and Magnus lift forces are ignored because the standard atomization models do not track particle rotation, and the velocity gradients in the bulk chamber flow are insufficient to generate significant shear lift [9].

By neglecting the mathematically insignificant forces, the trajectory equation deployed in typical CFD solvers for spray drying is reduced to balancing the particle's inertial momentum against the aerodynamic drag force, the gravitational force and buoyancy. Equation (3.8) can be simplfied to:

$$m_p \frac{d^2\vec{r}}{dt^2} = \frac{1}{8}\pi d_p^2 \rho_f |\vec{u}_f - \vec{u}_p|(\vec{u}_f - \vec{u}_p) + \frac{\pi d_p^3}{6}(\rho_p - \rho_f)\vec{g} \tag{3.14}$$

3.4 Coupling of Droplet Evaporation with Gas Dynamics

Within the Eulerian-Lagrangian framework, the transient thermal and mass histories of the discrete phase are mathematically resolved by integrating highly coupled, non-linear ordinary differential equations along the individual particle trajectories [28]. In SHS spray drying, the thermodynamic environment is characterized by a pure, single-component condensable fluid. The absence of non-condensable carrier gas alters the standard interphase transport phenomena governing these histories [12].

The thermodynamic interaction between the primary and secondary phases undergo shifts, hence the process is divided up into three distinct stages - condensing and heating, constant-rate evaporation, and falling-rate drying - governed by different equations, describing the heat transfer process.

3.4.1 Initial Condensation and Sensible Heating Regime

When the subcooled liquid feedstock is injected into high-enthalpy SHS environment, the surface temperature of the droplet is significantly below the saturation of the bulk steam. This thermal gradient induces the immediate condensation of the steam directly onto the cold droplet surface.

During this period, the droplet mass (m_p) increases due to the condensing steam, and the massive release of latent heat increases the droplet temperature. The temporal evolution of droplet temperature (T_p) is governed by the transient energy balance:

$$m_p c_p \frac{dT_p}{dt} = h_c A_p (T_\infty - T_p) \tag{3.15}$$

In Equation (3.15), c_p denotes the specific heat capacity of the particle, A_p is the droplet surface area, h_c is the localized film condensation heat transfer coefficient and T_∞ is the bulk temperature of the superheated steam.

The regime terminates the moment thermodynamic equilibrium is achieved at the droplet surface, meaning T_p reaches saturation temperature (T_{sat}) [16]. Due to the low thermal inertia of the droplet and the high latent heat of steam, this period is relatively short from the perspective of the whole process. Many simplified CFD simulations neglect the condensation mass-gain and resolve only the sensible heat-up [16]. The heat transfer coefficient h_c may be estimated using specialized correlations, such as the McAdams equation [11].

3.4.2 Constant Rate Evaporation

Once the droplet is heated to the boiling point, the phase-change dynamics invert. The initial condensation stops, and the unbound surface moisture undergoes rapid vaporization [11]. Throughout this regime, the droplet temperature remains strictly isothermal at the saturation point:

$$T_p = T_{\text{sat}} \implies \frac{dT_p}{dt} = 0 \tag{3.16}$$

Because sensible heating drops to zero, the entirety of the convective thermal energy transferred from the bulk steam is consumed as the latent heat of vaporization (H_{evp}). The governing mass transfer equation, coupling the droplet shrinkage to the external convective heat flux, is formulated as:

$$\frac{dm_p}{dt} = -\frac{hA_p(T_\infty - T_p)}{H_{\text{evp}}} \tag{3.17}$$

To achieve mathematical closure of Equation (3.17), the convective heat transfer coefficient (h) for forced convection around a spherical body is typically evaluated via empirical Nusselt number (Nu_p) correlation, such as the Ranz-Marshall equation [16]:

$$\text{Nu}_p = \frac{hd_p}{k_g} = 2.0 + 0.6\,\text{Re}_p^{1/2}\text{Pr}^{1/3} \tag{3.18}$$

In Equation (3.18), d_p is the droplet diameter, k_g is the thermal conductivity of steam, Re_p is the droplet Reynolds number defined as:

$$\text{Re}_p = \frac{d_p|U|}{\nu}$$

where d_p is the particle diameter, $|U|$ is the magnitude of particle's velocity vector and ν is the kinematic viscosity of the carrier phase. In Equation (3.18), Pr is the Prandlt number, defined as:

$$\text{Pr} = \frac{\nu\rho C_p}{k}$$

where C_p is the gas specific heat capacity, ρ is the gas density, and k is the gas thermal conductivity.

3.4.3 Falling-Rate Period

As the unbound surface solvent is depleted, the droplet reaches its critical moisture content (X_{cr}). In processing suspensions or solutions, this triggers the segregation and precipitation of solid constituents, establishing a porous solid crust. This crust imposes mass transfer resistance, shifting the rate-limiting step from external boundary layer convection to internal moisture diffusion [11].

The macroscopic evaporation rate decelerates. The restricted mass transfer is typically modeled as:

$$\frac{dX}{dt} = -kX^n \tag{3.19}$$

In Equation (3.19), X is the dry-basis moisture content, while k and n are empirical constants.

As the restricted vaporization rate can no longer absorb the entirety of the external convective heat flux as latent heat, the thermodynamic equilibrium is broken. The radial temperature profile of the particle begins to change towards the bulk steam temperature T_∞. The coupled energy conservation equation is expanded to balance the external convection against both the latent heat sink and the sensible heating of the solid matrix [16]:

$$m_p c_p \frac{dT_p}{dt} = hA_p(T_\infty - T_p) + H_{\text{evp}}\frac{dm_p}{dt} \tag{3.20}$$

3.5 Phase Coupling and Source Terms

In the context of CFD, phase coupling refers to the mathematical representation of the exchange of mass, momentum, and thermal energy between the continuous fluid medium and the discrete particles. This interphase interaction is classified into distinct regimes based on the volume fraction of the dispersed phase (α_p) and the dominance of specific transport mechanisms [13]:

- **One-way coupling**: The continuous gas phase dictates the trajectory of the discrete particles via hydrodynamic forces, but the particles exert no reciprocal influence on the gas. This assumption is only valid for extremely dilute, non-evaporating flows ($\alpha_p < 10^{-6}$).
- **Two-way coupling**: The dispersed phase reciprocally alters the continuous phase through interphase exchange terms.
- **Four-way coupling**: Applied in dense flow regimes ($\alpha_p > 10^{-3}$), this framework resolves stochastic particle-particle interactions, such as collisions and coalescence.

For most industrial spray drying simulations, two-way coupling is generally required to capture momentum and thermal feedback between phases [9]. In a spray dryer, the phase-change phenomena inherent to solvent vaporization cause significant hydrodynamic disruptions within the drying medium.

As droplets evaporate, they extract significant amounts of sensible heats from surrounding medium, at the same time injecting water vapor. This mass addition locally alters the gas density and dynamic viscosity, which leads to modified drag forces and turbulent flow field [19].

Neglecting two-phase coupling will lead to highly inaccurate predictions of both the macroscopic gas flow patterns and microscopic particles morphology. In particular zones of the drying chamber, such as the nozzle, where particle loading is higher, a four-way coupling may even be necessary [13].

3.5.1 Source Term Quantification

The source terms are quantified by treating the Lagrangian dispersed phase as distributed volumetric sources or sinks within the primary phase. As the solver tracks the trajectory of each computational parcel through the domain, the net change in mass, momentum, and enthalpy of the parcel is integrated over the tracking time step [17].

These integral changes are then accumulated for all individual particles residing within the control volume, and divided up by the cell's volume to yield localized volumetric source terms [29]. These computer source terms are then injected back into the Eulerian governing equations for the next iterative calculation of the gas phase [9].

The specific mathematical formulation defining these volumetric interphase exchange terms are extracted directly from the Lagrangian tracking histories.

Mass Source Term

This term accounts for the solvent vaporized from the droplets into the continuous phase. It is quantified by summing over the evaporative rates ($\dot{m}_{p,k}$) of all particles within the computational cell volume (V_{avg}):

$$S_{\text{mass}} = \frac{1}{V_{\text{avg}}} \sum_k \dot{m}_{p,k}$$

Momentum Source Term

Momentum coupling consists of the aerodynamic drag reaction force and the momentum flux induced by the mass transfer. The specific momentum flux transferred to the continuous phase strictly due to the velocity ($v_{i,k}$) of the evaporating mass is:

$$S_{\text{mom}} = -\frac{1}{V_{\text{avg}}} \sum_k m_{p,k} v_{i,k}$$

Thermal Source Term

This acts as thermal sink in the continuous phase energy equation, including both convective heat transfer to the droplet and the latent heat demand for vaporization. It is generalized as:

$$S_E = -\frac{1}{V_{\text{avg}}} \sum_k q_k$$

where q_k is the heat flux transferred to the discrete phase.

Chapter 4

Numerical Framework and Implementation

4.1 Hydrodynamic Tracking of Particles

4.1.1 Single Phase Flow

In the initial phase, the numerical simulation is limited to the pure hydrodynamic tracking of the dispersed particulate phase, neglecting the highly non-linear interphase heat, momentum and mass transfer mechanisms.

Before attempting to simulate coupled movement of discrete particles and continuous phase, a converged flow field of steam is necessary. This way the particles are introduced to a stable flow field, which eases convergence and improves accuracy of the solution. In this way the computational cost can be reduced.

Numerical Mesh

In CFD, spatial discretization requires partitioning the macroscopic continuous flow domain into finite, non-overlapping subdomains, called computational grid or mesh. The governing PDEs are numerically integrated and iteratively solved across these discrete control volumes.

The shape and spatial resolution of the mesh determine the accuracy, numerical stability, and physical fidelity of the CFD solution. The grid resolution govern the solver's capacity to capture flow features. A coarse mesh allows for lower computational overhead at the cost of numerical diffusion, damping of transient flow structures, fluctuations and high-frequency eddies. Using an insufficiently refined grid forces the flow to behave in a steady-state manner.

Specialized mesh topologies near solid boundaries are needed to accurately predict shear stresses and thermal boundary layers. Inflation layers are deployed adjacent to walls to capture severe velocity gradients.

Aside from sheer element density, the quality of the mesh elements governs numerical convergence and computational overhead. Parameters such as mesh orthogonality, skewness, and maximum aspect ratio must follow best industrial practices. Elements with extreme skewness or severe aspect ratios amplify truncation errors, increase required computational time, and may induce solver divergence.

Having the above constraints in mind, a set of numerical meshes varying in element size and shape has been prepared in order to analyze the dependence of the solution on the numerical grid. An example of a prepared numerical mesh is visible in Figure (4.1). The key characteristics of each mesh have been listed in Table (4.1).

Steady-State Simulation

An initial investigation was conducted to determine the feasibility of a steady-state solution for the continuous phase. It was necessary to assess whether the flow domain exhibited inherent unsteadiness or large-scale transient vortex shedding that would prevent the convergence of a steady-state simulation.

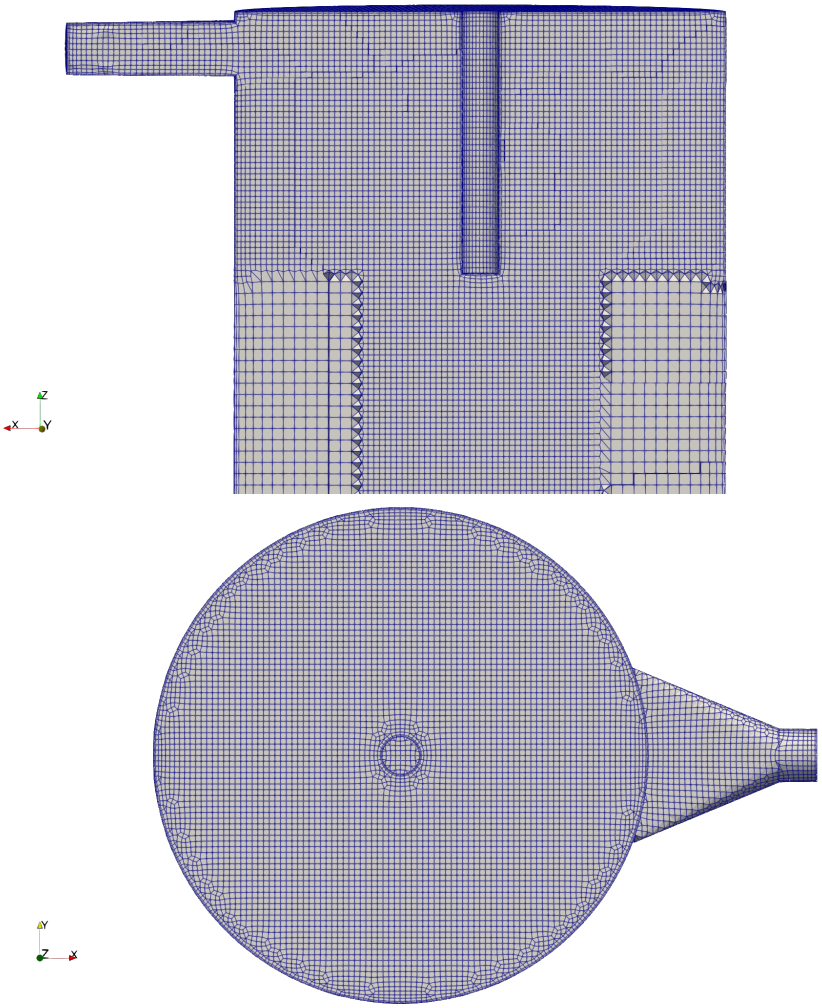


Figure 4.1: Cross section and top views of a refined hexahedral dominant mesh.

Table 4.1: Quality metrics of prepared numerical meshes.

	Element #	**Orthogonality Max/Avg.**	**Max Skewness**	**Max Aspect Ratio**
Coarse Mesh	254k	63.66/ 3.47	2.42	11.85
Refined Mesh	591k	59.10/ 3.07	2.39	9.70
Finest Mesh	1040k	58.62/ 2.91	2.39	12.94

The selection of a steady-state framework over a fully transient approach offers significant computational savings, particularly for extensive sensitivity studies and parametric optimizations. By reducing the total CPU time required per iteration, a broader range of operating conditions can be evaluated to determine the influence of specific variables on the overall drying performance.

To resolve the steady-state flow field, the **simpleFoam** solver was employed. This solver utilizes the Semi-Implicit Method for Pressure-Linked Equations (SIMPLE) algorithm to achieve pressure-velocity coupling in incompressible flows . The assumption of an incompressible fluid is justified given the near-isothermal conditions and the low Mach number characteristic of the bulk chamber flow, where local pressure variations

remain negligible relative to the operating pressure.

Steady State Numerical Setup and Boundary Conditions

The numerical case was configured within the OpenFOAM environment using a Reynolds-Averaged Navier-Stokes approach . Turbulence closure was achieved via the Shear Stress Transport (SST) $k-\omega$ model, selected for its superior performance in resolving both free-stream shear layers and near-wall boundary layer separations . The kinematic viscosity was specified as $3.20 \times 10^{-5}\,\mathrm{m}^2/\mathrm{s}$.

The definition of the computational domain's boundary conditions is summarized as follows:

- **Inlet**: A fixed velocity of $\vec{u} = (21.55, 1.0, 0)\,\mathrm{m/s}$ was prescribed. Turbulence quantities were initialized with a 5% turbulence intensity condition for the kinetic energy (k), while the specific dissipation rate (ω) was defined using a mixing length of 0.01 m.
- **Outlet**: To prevent numerical backflow, an inletOutlet condition was applied to the velocity field, coupled with a fixed static pressure of 0 Pa.
- **Walls**: A no-slip condition was enforced for the velocity field. Standard wall functions were utilized for k and ω to ensure proper boundary layer treatment and the correct calculation of near-wall turbulent stresses .

Steady State Discretization Schemes and Solution Control

The numerical integration of the governing equations utilized a steady-state time discretization scheme. Spatial discretization of the gradient terms was resolved using Gauss linear schemes, while convection terms for the velocity field employed a second-order linear upwind scheme. For the turbulence quantities, a first-order upwind scheme was selected to enhance numerical stability during the initial convergence phase.

The pressure field was solved using the Geometric-Algebraic Multigrid (GAMG) solver, while velocity and turbulence quantities were resolved using a smooth solver with Gauss-Seidel smoothing. To ensure stability in the presence of non-orthogonal mesh elements, the SIMPLE loop was executed in a consistent mode. Convergence was strictly monitored via normalized residuals, with target limits set at 10^{-5} for pressure and 10^{-4} for the velocity and turbulence fields (k, ω). To facilitate stable convergence, under-relaxation factors were applied as follows: 0.5 for velocity, 0.4 for pressure, and 0.6 for the turbulence variables.

Transient Simulation

Initial attempts to resolve the flow field using a steady-state framework encountered persistent convergence instabilities, suggesting the presence of inherent transient phenomena or large-scale unsteady structures within the drying chamber. To accurately capture these temporal fluctuations and ensure a physically representative solution, the numerical framework was transitioned to a fully transient formulation.

The **rhoPimpleFoam** solver was selected for this phase. This pressure-based, transient solver is designed for compressible flows and utilizes the PIMPLE algorithm — a hybrid of the Pressure-Implicit with Splitting of Operators (PISO) and Semi-Implicit Method for Pressure-Linked Equations methods — to resolve the pressure-velocity coupling in compressible regimes. The boundary conditions for the transient simulations remained consistent with those defined in the previous steady-state investigations to allow for direct comparative analysis.

Transient Temporal and Spatial Discretization

Temporal discretization was achieved using a first-order implicit Euler scheme. The simulation was initialized with a time step (Δt) of 1×10^{-4} s. To maintain numerical stability while optimizing computational efficiency, adaptive time-stepping was employed. The maximum time step allowed to be taken by the solver is set by the definition of the Courant number.

The Courant number is a dimensionless metric in CFD that dictates the stability and temporal accuracy of transient simulations. For a given computational cell, it is defined as:

$$Co = \frac{\delta t |U|}{\delta x}$$

where δt is simulation time step, $|U|$ is the magnitude of the fluid velocity passing through that cell, and δx is the physical cell size in the direction of velocity.

The maximum Courant number (Co) was limited to 5.0, though the mean Courant number throughout the stable portion of the simulation remained significantly below 1.0.

Spatial discretization followed a second-order approach where possible to maintain high fidelity. Gradient terms were resolved using Gauss linear schemes. For momentum divergence terms, a linear upwind scheme with deferred corrections was implemented to mitigate numerical diffusion. To prioritize numerical robustness, the energy and turbulence transport equations utilized a pure upwind differencing scheme. Laplacian operators and surface normal gradients employed corrected Gauss linear formulations to account for mesh non-orthogonality.

Transient Solution Control and Convergence Criteria

The linear systems were resolved using a segregated approach. The pressure equation was solved via the GAMG algorithm with Gauss-Seidel smoothing, targeting an absolute tolerance of 1×10^{-6}. For the velocity, enthalpy, and turbulence fields, a smooth solver with symmetric Gauss-Seidel smoothing was utilized, also converging to an absolute tolerance of 1×10^{-6}.

The PIMPLE loop configuration was optimized for transient stability as follows:

- **Iterations**: Four outer correctors per time step were specified, followed by two inner pressure corrections and zero non-orthogonal corrections.
- **Predictors**: The momentum predictor was enabled to accelerate convergence, and a consistent formulation was maintained.
- **Stability**: Pressure bounds were restricted to a range of 0.1 to 2.0 times the reference pressure to prevent unphysical oscillations during the initial transient startup.
- **Residuals**: Convergence within each time step was monitored through residual control, with limits of 10^{-5} for pressure and 10^{-4} for velocity and turbulence quantities.

In contrast to the steady-state approach, no under-relaxation factors were applied during the transient simulations to preserve the temporal accuracy of the solution.

4.1.2 Multiphase Flow Implementation

Following the establishment of a converged single-phase flow field and the selection of an optimal computational mesh, the numerical investigation was advanced to incorporate multiphase flow dynamics.

To estimate the appropriate interphase coupling regime prior to simulation, the global average particle volume fraction (α_{avg}) was calculated. In accordance with established industrial guidelines, the required phase coupling architecture is dictated by the dispersed phase volume fraction:

- $\alpha_p \leq 10^{-6}$: One-way coupling.
- $10^{-6} < \alpha_p \leq 10^{-3}$: Two-way coupling.
- $\alpha_p > 10^{-3}$: Four-way coupling.

The global average volume fraction was approximated using the following analytical relation:

$$\alpha_{\text{avg}} = \frac{\dot{M}\tau}{\rho_p V_{\text{domain}}} \tag{4.1}$$

where $\dot{M}$ denotes the mass flow rate of the liquid feedstock, τ represents the continuous gas residence time, ρ_p is the discrete particle density, and V_{domain} is the total volume of the drying chamber. Based on the specific operating conditions of the pilot facility, this preliminary evaluation indicated that a two-way coupling framework is the appropriate baseline assumption. However, because spray drying chambers exhibit spatial gradients this global assumption requires subsequent verification through the analysis of local volumetric cell fractions upon simulation completion.

Solver Selection and Thermodynamic Framework

Multiphase simulations were executed using the **reactingParcelFoam** [30] solver. As an Eulerian-Lagrangian extension of the previously utilized **rhoPimpleFoam** solver, **reactingParcelFoam** is fundamentally designed to handle reacting or combusting sprays within a compressible continuous medium, making its underlying multiphase architecture highly suitable for superheated steam applications.

The macroscopic boundary conditions, as well as the temporal and spatial discretization schemes, were maintained from the transient single-phase model to ensure a consistent comparative baseline. The continuous phase thermodynamic framework was defined using the **heRhoThermo** model coupled with a **reactingMixture** [31] composition. Transport properties were evaluated via Sutherland's law, while caloric properties were derived from JANAF thermodynamic tables [32]. For this specific intermediate phase of the investigation, the energy transport equation was formulated in terms of sensible enthalpy, and the pure superheated steam environment was modeled using an ideal gas Equation of State.

Discrete Phase Modeling and Injection

During this phase, particles were tracked as inert computational parcels. The interphase coupling was restricted strictly to momentum exchange; heat and mass transfer mechanisms were temporarily deactivated to isolate hydrodynamic behaviors. The discrete phase represents a composite matrix of an undisclosed solid suspended in an aqueous solvent, with the resulting thermophysical properties computed via mass-fraction-weighted averaging. Parcel kinematics were governed exclusively by aerodynamic sphere drag and gravitational body forces.

The discrete phase was introduced into the computational domain via a solid cone injection model. Key atomization parameters — specifically the parcel injection rate, initial velocity magnitude, and initial spray angle — were designated as independent variables for a subsequent sensitivity analysis to evaluate their impact on residence time distributions.

Particle Kinematics and Boundary Interactions

The Lagrangian trajectories — encompassing particle position and velocity — were integrated using an explicit Euler scheme, while particle temperatures were held constant. To accurately evaluate the momentum exchange source terms, continuous phase quantities (density, pressure, dynamic viscosity, and thermodynamic state) were mapped to the parcel centroids using standard cell-value interpolation. Conversely, the continuous phase velocity field utilized a higher-order cell-point interpolation to enhance the accuracy of the relative slip velocity used in the aerodynamic drag calculations.

Particle-wall interactions were governed by the **localInteraction** model. Upon impingement with the chamber boundaries, parcels underwent inelastic rebound, characterized by a normal restitution coefficient of 0.7 and a tangential wall friction coefficient of 0.09. Parcels successfully navigating the flow field to the exhaust outlet were subjected to an "escape" boundary condition, which formally terminated their Lagrangian tracking sequence.

4.2 Hydrodynamic and Thermal Simulation

Following the purely hydrodynamic particle tracking, the numerical framework was expanded to incorporate coupled interphase heat and mass transfer. A limitation of the native solvers within OpenFOAM (v2412) is their inability to simulate phase change within a superheated steam environment. Standard libraries are formulated for evaporation into an inert carrier gas via concentration-driven diffusion and lack the specific thermodynamic mechanisms for pure-vapor boiling. Consequently, it was necessary to develop a custom phase-change library and formulate a modified Eulerian-Lagrangian solver. Additionally, none of the libraries have the capability of modeling crust formation when particles are dried.

The physical model assumes the injection of a composite droplet comprising both an aqueous solvent and a suspended solid phase. The transient thermodynamic and morphological evolution of this droplet encompasses three distinct kinetic regimes:

1. **Sensible Heating Regime**: The subcooled droplets extract thermal energy from the surrounding superheated steam, increasing their internal temperature as governed by Equation (3.15). To maintain solver stability and reduce computational stiffness, the transient mass addition from initial steam condensation is neglected; heating is driven purely by convective sensible heat transfer, resulting in a localized temperature sink within the continuous phase.

   The Biot number is a dimensionless quantity used in transient heat transfer calculations. It is defined as:

   $$Bi = \frac{hL_c}{k_s}$$

   where h is the convective heat transfer coefficient at the surface of the body, L_c is the characteristic length of the body, and k_s is the thermal conductivity of the material. It measures the ratio of the heat transfer resistance inside the solid body to the heat transfer resistance at its surface.

   Assuming a sufficiently low Biot number ($Bi < 0.1$), internal thermal gradients are considered negligible, allowing the droplet to heat uniformly.

2. **Constant Rate Evaporation**: This phase initiates once the particle reaches the saturation temperature of the solvent. The droplet temperature remains strictly isothermal, and the phase-change kinetics transition to a purely heat-flux-limited boiling mechanism. The rate of solvent vaporization is evaluated according to Equation (3.17).

3. **Falling-Rate Period**: The onset of this final stage is triggered when the particle's moisture content falls below a critical threshold, prompting the precipitation of solid constituents to form a porous crust, as illustrated in Figure (2.1). Consequently, unbound surface moisture is depleted, and the evaporation rate is no longer governed solely by external convective heat transfer. The newly formed solid matrix introduces a significant internal mass transfer resistance. Because the reduced evaporation rate can no longer consume the entire convective heat flux as latent heat, a portion of the thermal energy elevates the sensible temperature of the solid crust according to Equation (3.20).

Standard OpenFOAM phase-change libraries cannot resolve this purely heat-transfer-controlled boiling mechanism, hence a custom C++ library designated as **SuperheatedEvaporationBoil** was developed. This customized thermodynamic library was subsequently integrated into a newly compiled solver, **crustReactingParcelFoam**, which operates as an extended derivative of the standard **reactingParcelFoam** architecture.

The solver is governed by the following core assumptions:

- **Spherical Symmetry & Dilute Phase**: Droplets remain perfectly spherical throughout all drying regimes. Secondary breakup, non-spherical deformation, and droplet-droplet interactions (coalescence and collision) are neglected under the assumption of a dilute discrete phase.
- **Lumped-Capacitance Approach**: Internal thermal gradients are neglected based on a low Biot number, assuming uniform droplet temperature. Bulk thermophysical properties (ρ_p, C_p, k_p) are evaluated on a mass-fraction-averaged basis.
- **Unidirectional Mass Transfer**: Mass transfer occurs from the discrete phase to the continuous phase. Transient steam condensation onto subcooled droplets ($T_p < T_{\text{sat}}$) and its associated latent heat release are neglected to prevent stiffness in the pressure-velocity matrix; initial heating is driven purely by convective sensible heat transfer.
- **Rigid Shell Kinetics**: Following crust onset at a critical moisture content, the particle outer diameter remains constant, while internal moisture depletion continues through the porous matrix.

4.2.1 Model Architecture

The new parcel cloud model is built within OpenFOAM's Lagrangian Discrete Phase Model (DPM) framework using C++ class templating and runtime selection mechanisms. The architecture comprises of two main layers:

1. The custom submodel (**SuperheatedEvaporationBoil**): Inherits from OpenFOAM's **PhaseChangeModel** to govern superheated boiling dynamics coupled with a critical moisture fraction limit (X_{critical}) for crust formation.
2. The custom cloud and parcel types (**CrustReactingMultiphaseParcel**): Built via OpenFOAM's C++ class templating and runtime selection, wrapping base Lagrangian parcel layers.

The top down code architecture is presented in Figure (4.2).

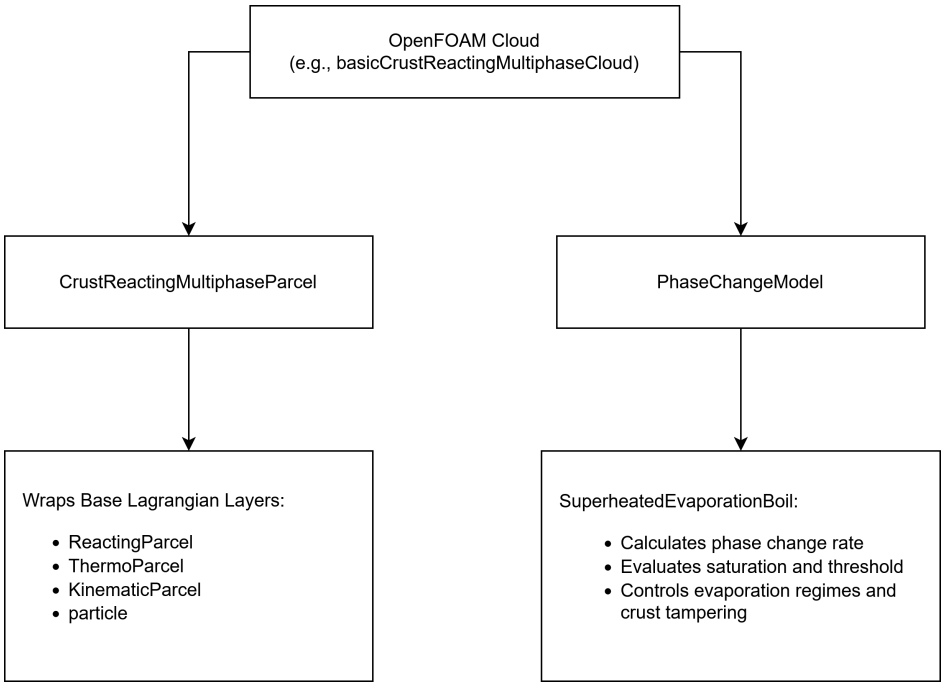


Figure 4.2: Parcel Cloud Class architecture.

Class Structure

The particle system is defined by a multi-layered template hierarchy:

1. **particle**: Base point-location and tracking class.
2. **KinematicParcel**: Handles particle momentum, velocity, and drag forces.
3. **ThermoParcel**: Manages sensible heat transfer and thermal equilibrium.
4. **ReactingParcel**: Manages multicomponent species composition and phase change.
5. **CrustReactingMultiphaseParcel**: Extends the reacting parcel to incorporate solid crust growth dynamics and modified mass transfer interfaces.

The phase change dynamics are encapsulated in a custom submodel class **SuperheatedEvaporationBoil** inheriting from **PhaseChangeModel**.

Phase Change and Crust-Formation Governing Equations

The mass transfer rate for liquid species i during a timestep Δt is governed by the heat-flux-limited evaporation rate:

$$\dot{Q} = h_c A_p (T_c - T_p)$$

where the heat transfer coefficient h_c is determined via the Nusselt number Nu:

$$h_c = \frac{Nu \cdot \kappa_g}{d_p}, \quad Nu = 2 + 0.74 Re^{1/2} Pr^{1/3}$$

To account for crust formation during drying, a moisture-fraction threshold X_{critical} is evaluated on a wet basis:

$$X_{\text{water}} = \frac{m_{\text{liquid}}}{m_{\text{solid}} + m_{\text{liquid}}}$$

The effective heat transfer is scaled by a tapering factor η:

$$\eta = \begin{cases} 1.0 & \text{if } X_{\text{water}} > X_{\text{critical}} \quad \text{(Equilibrium Regime)} \\ \frac{X_{\text{water}}}{X_{\text{critical}}} & \text{if } X_{\text{water}} \leq X_{\text{critical}} \quad \text{(Diffusion-Limited Regime)} \end{cases}$$

The mass evaporated during the timestep Δt is bounded by the available liquid mass:

$$\Delta m_i = \min\left(\frac{\dot{Q} \cdot \eta}{h_{\text{fg},i}} \Delta t,\ m_{\text{liquid},i} \right)$$

The custom parcel class and phase change library are essentially tools used by the written custom solver **crustReactingParcelFoam**. This is a transient, compressible, turbulent CFD solver for multiphase Lagrangian particle clouds coupled with Eulerian carrier-phase fluid dynamics. The code architecture of the new solver is presented in Figure (4.3).

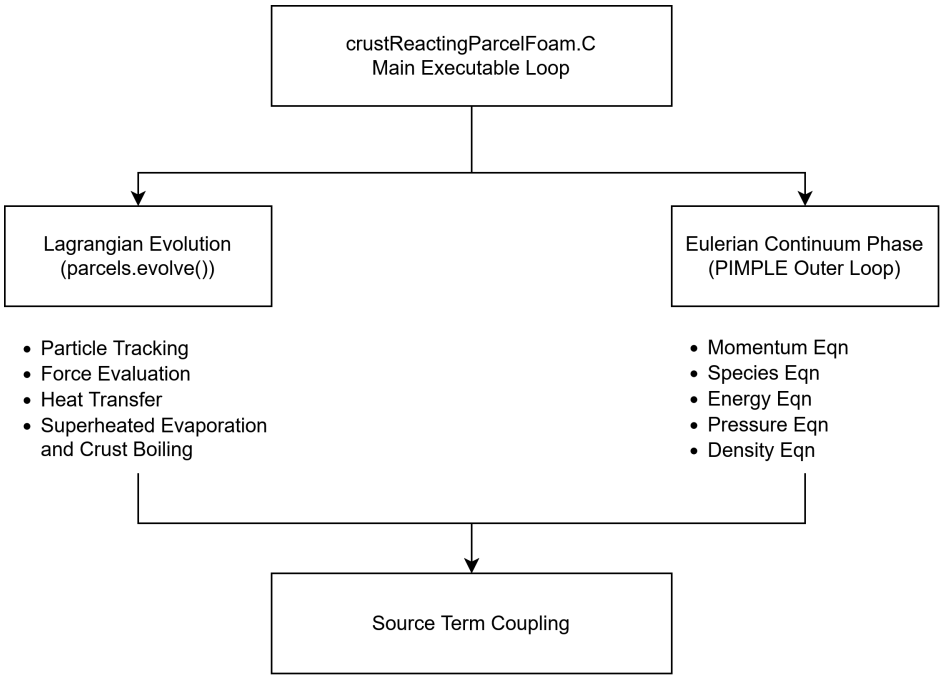


Figure 4.3: Custom multiphase solver architecture.

During each time step, the executable executes an evolution loop where the Lagrangian cloud updates parcel tracking, forces, heat transfer, and custom submodels, specifically the **SuperheatedEvaporationBoil** model, which governs phase change and crust formation transitions.

The resulting exchange of mass, momentum, species, and thermal energy is explicitly coupled into the Eulerian continuum equations as source terms. The gas-phase flow solution is then advanced using OpenFOAM's PIMPLE algorithm, which iteratively corrects pressure and velocity fields while maintaining dynamic time-step control based on flow Courant number.

Following the verification of the developed solver package, the fully coupled transient simulation was initiated. The temporal and spatial discretization schemes, as well as the macroscopic boundary conditions and turbulence models, were retained from the preliminary hydrodynamic verification phase to ensure numerical consistency. The base thermophysical framework remains unchanged. The injection parameters for the discrete phase mirror the prior setup, with the addition of the initial particle temperature ($T_{p,0}$) and critical moisture content (X_{crit}). The influence of this specific thermal boundary condition on the drying kinetics will be systematically examined within the subsequent parametric sensitivity study.

Chapter 5

Verification and Validation

To establish a baseline before executing the mesh sensitivity study, it is necessary to first evaluate the macroscopic flow fields and the convergence behavior of the continuous phase.

5.1 Single Phase Flow

5.1.1 Flow Regime Assessment

Initial attempts to resolve the flow field utilizing a steady-state solver failed to achieve the specified convergence criteria. As depicted in Figure (5.1), the equation residuals exhibited an initial decay but subsequently stalled, with further iterations incapable of diminishing the numerical error. This asymptotic residual behavior indicates that the continuous phase is characterized by large-scale unsteadiness and asymmetric flow structures. Consequently, a fully transient simulation framework was necessary.

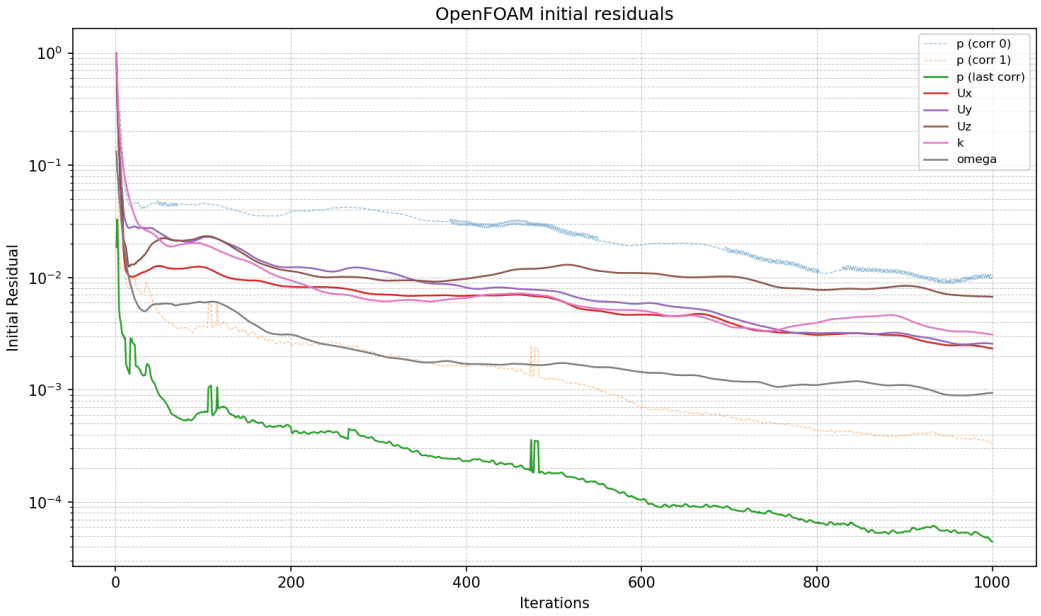


Figure 5.1: Residuals of a steady state simulation run.

The implementation of a transient solver successfully mitigated these numerical instabilities, allowing the residuals to converge within the prescribed tolerance during each temporal integration step, as illustrated in Figure (5.2).

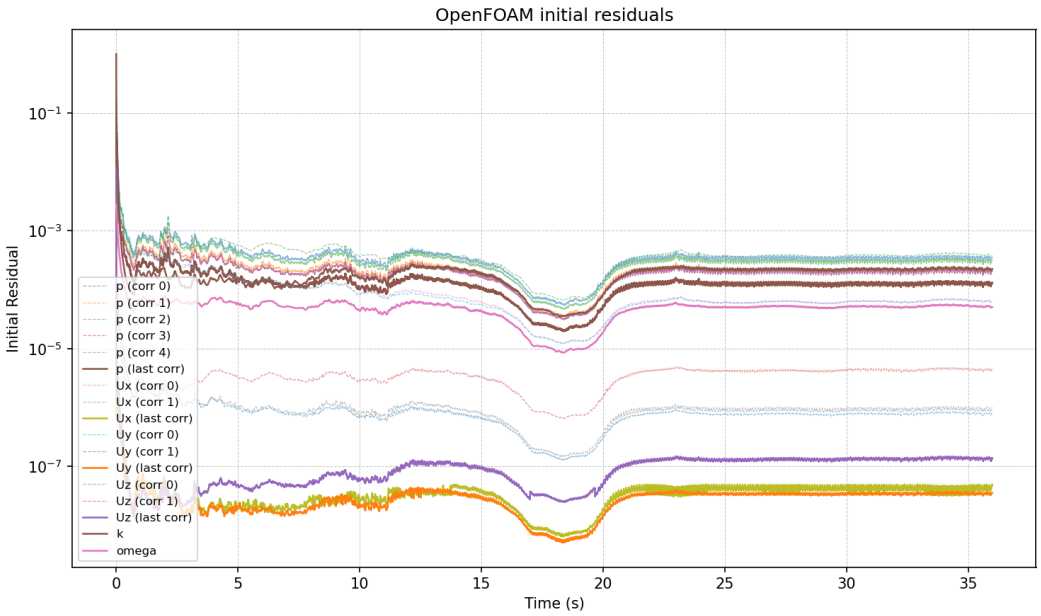


Figure 5.2: Residuals of a transient simulation run.

The macroscopic hydrodynamics of the gas phase within the spray dryer are dominated by a rotational flow regime as seen in Figure (5.3a). The tangential injection of the continuous phase induces a swirl component as the fluid propagates downward through the chamber. Near the central axis, an asymmetric Central Recirculation Zone is established.

The asymmetry of this core vortex is evident in the pressure distribution depicted in Figure (5.3b) and correlates with the velocity contour plot, where localized velocity magnitudes is diminished within the vortex center. The velocity vector plot in Figure (5.3a) further details the swirling kinematics; the highest velocity magnitudes are concentrated at the upper inlet region and within the outer annulus surrounding the central vortex.

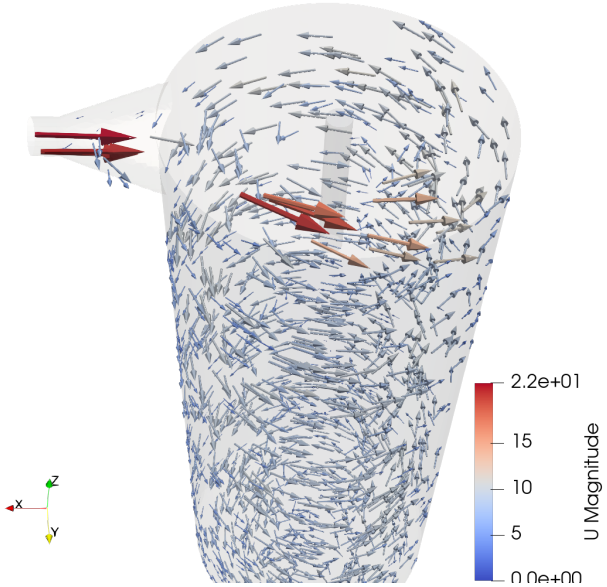
Concurrently, Figure (5.3d) demonstrates a pronounced radial pressure gradient. The centrifugal forces induced by the swirl direct the gas mass toward the chamber walls, generating a localized high-pressure zone at the periphery. From a multiphase perspective, it is highly probable that discrete particles subjected to this flow field will experience substantial centrifugal acceleration, increasing the likelihood of particle-wall impingement.

A closer look at pressure iso-surfaces reveals that this core structure is not characterized by high-frequency precession around the geometric axis; rather, it shows as a quasi-stable volumetric pulsation. Successive temporal snapshots of this pressure gradient are presented in Figure (5.4).

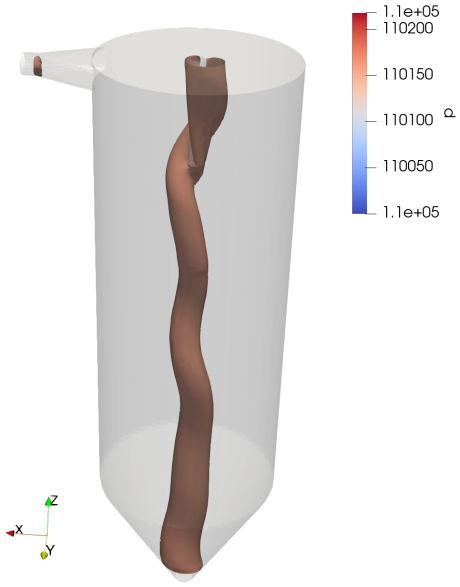
The pulsating vortex undergoes continuous spatial expansion and contraction, which consequently induces low-frequency oscillations within the surrounding velocity field. From a process engineering perspective, this transient shifting is advantageous; the continuous perturbation of the flow field prevents the formation of persistent, static stagnation zones. This temporal instability mitigates the risk of particles becoming indefinitely trapped in local recirculation eddies, thereby preventing localized product degradation or scorching in the superheated steam environment.

Furthermore, it is observed that the upper boundary of the vortex anchors itself to the physical geometry of the atomization nozzle lance. The nozzle functions as a bluff body within the flow field. It is hypothesized that the aerodynamic wake generated by this physical intrusion stabilizes the vortex core, preventing the severe lateral vortex sliding. This bluff-body stabilization generates a localized region of relatively stagnant, recirculating steam adjacent to the nozzle exit, as illustrated in the velocity contours in Figure (5.5).

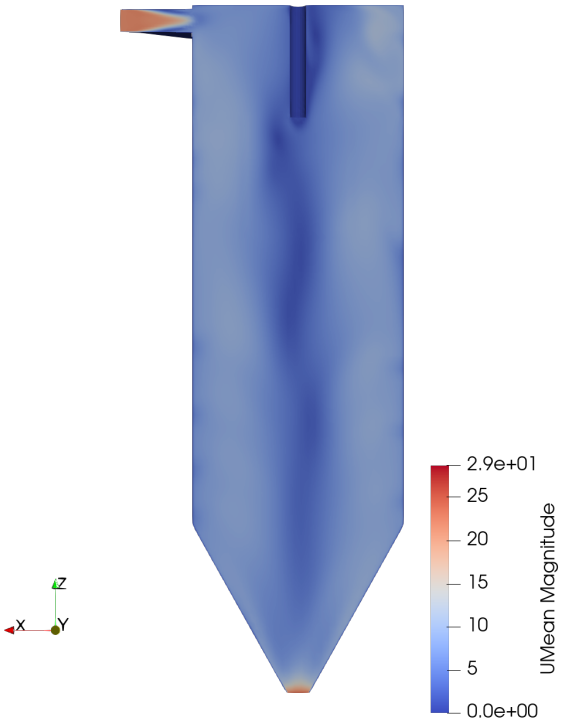
The velocity slices in Figure (5.5) further demonstrate the macroscopic flow topology, revealing a distinct helical structure rather than a perfectly axisymmetric swirling flow. The momentum distribution is skewed,



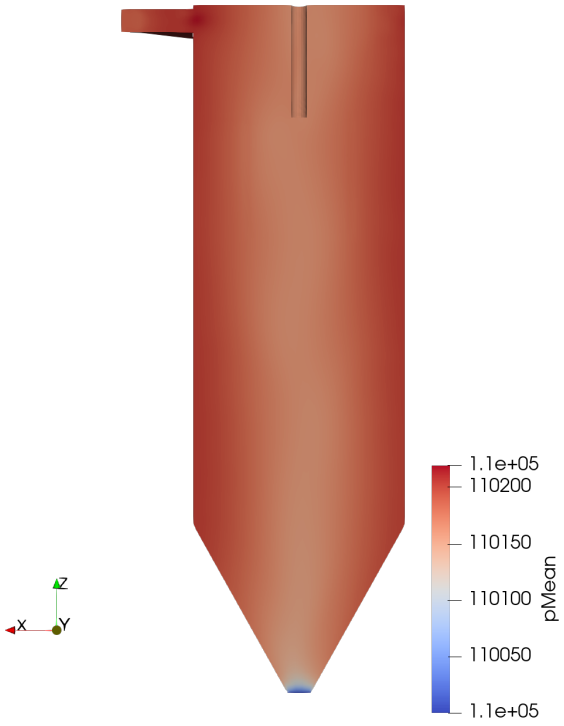
(a) Velocity Vector Plot



(b) Pressure Swirl



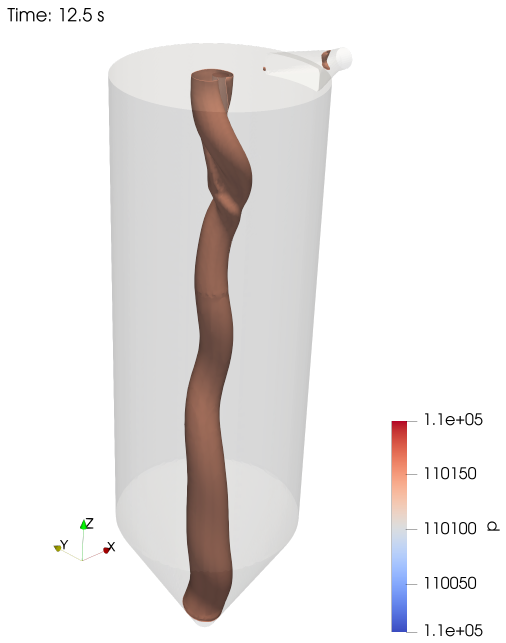
(c) Velocity Contour



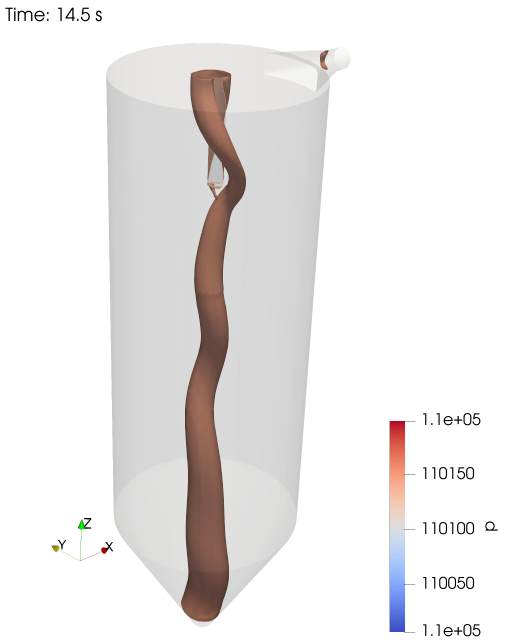
(d) Pressure Contour

Figure 5.3: Flow fields inside the domain.

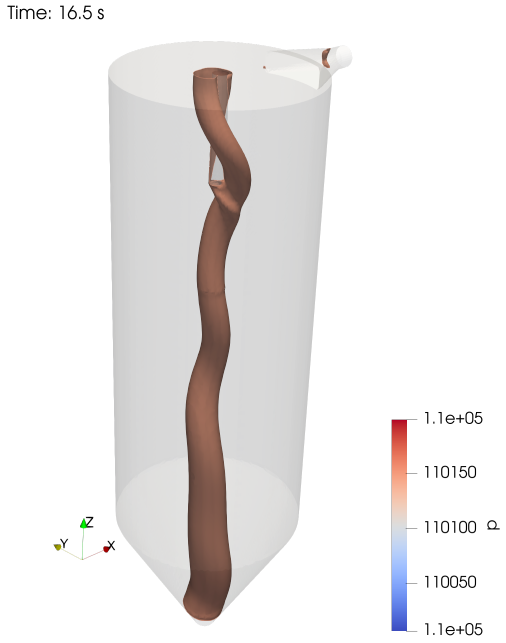
resulting in higher velocity magnitudes along one specific hemisphere of the outer cylindrical wall. This flow asymmetry holds significant implications for the subsequent multiphase simulations. It indicates that particle-wall interaction frequencies will not be uniformly distributed around the Z-axis; instead, deposition and fouling patterns will be anisotropic, governed by the dominant helical momentum bias of the continuous



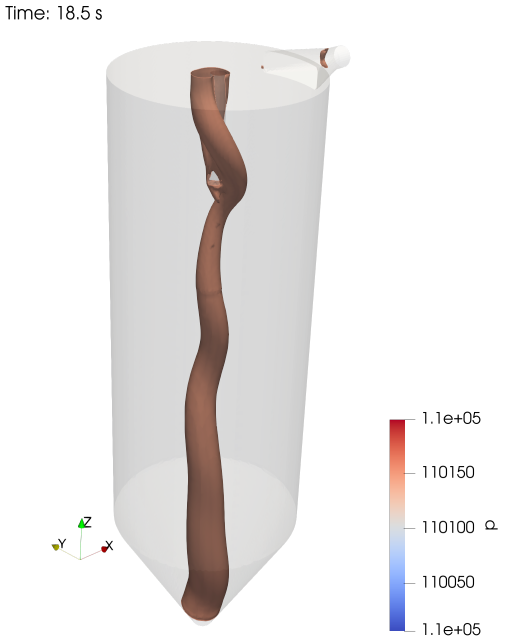
(a) Isosurface of the pressure swirl at $t = 12.5$ s



(b) Isosurface of the pressure swirl at $t = 14.5$ s



(c) Isosurface of the pressure swirl at $t = 16.5$ s

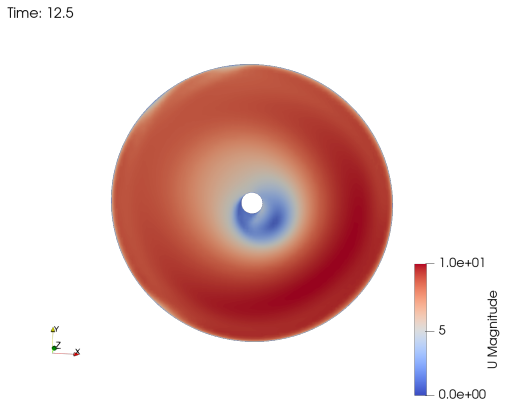


(d) Isosurface of the pressure swirl at $t = 18.5$ s

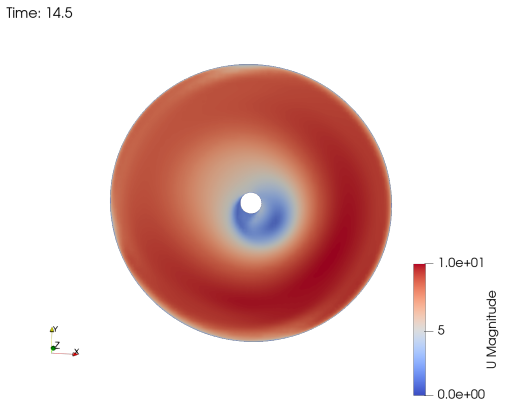
Figure 5.4: Temporal evolution and volumetric pulsation of the Central Recirculation Zone.

phase.

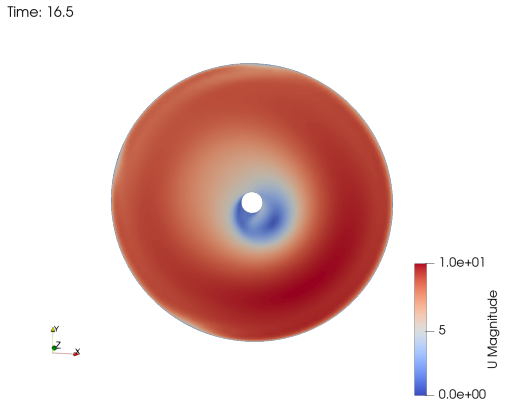
A temporal analysis of the flow field, presented in Figure (5.3), revealed that the asymmetric swirling core does not precess around the domain axis, but rather exhibits a localized volumetric pulsation. To determine whether this quasi-stable behavior was a physical characteristic of the specific chamber geometry or an artificial dampening artifact of the turbulence model, the assumptions of the standard Reynolds-Averaged



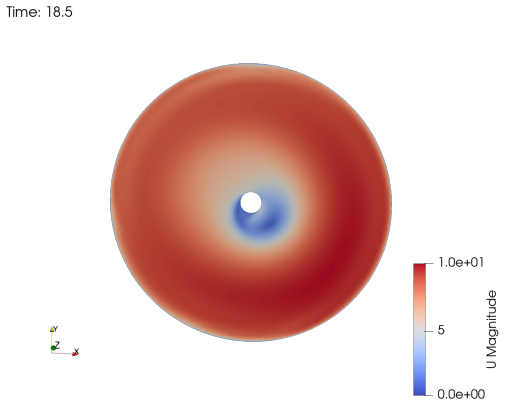
(a) Pressure swirl at $t = 12.5$ s



(b) Pressure swirl at $t = 14.5$ s



(c) Pressure swirl at $t = 16.5$ s



(d) Pressure swirl at $t = 18.5$ s

Figure 5.5: Temporal oscillations of the pressure swirl.

Navier-Stokes framework were evaluated.

The baseline $k-\omega$ SST model relies on the Boussinesq approximation, which assumes isotropic turbulence and treats turbulent momentum transfer analogously to molecular viscosity. In highly swirling flows, this assumption often leads to an over-prediction of turbulent eddy viscosity, effectively dampening macroscopic flow instabilities such as a Precessing Vortex Core. To investigate this potential numerical dampening, a rotation and curvature correction was implemented into the $k-\omega$ SST model. In curved streamlines, centrifugal forces create regions of stabilizing and destabilizing stratification. The curvature correction modifies the turbulence production terms, preventing the solver from erroneously dissipating severe velocity shear as isotropic turbulent kinetic energy, theoretically allowing dynamic vortex precession to develop.

However, subsequent simulations utilizing the curvature-corrected model did not yield significant morphological deviations in the flow field; the asymmetric vortex maintained its quasi-stable position as previously observed in Figure (5.3b). Furthermore, analysis of the turbulent kinetic energy fields confirmed that turbulence generation was predominantly confined to the upper chamber near the gas disperser. The lack of precession can therefore be attributed to the specific geometric constraints and the resulting macroscopic momentum balances, rather than artificial numerical dissipation.

5.1.2 Mesh Sensitivity Study

Following the initial validation of the continuous-phase solver settings, a mesh sensitivity study was conducted.

In computational fluid dynamics, the numerical mesh represents the spatial discretization of the governing partial differential equations. The resolution of this spatial grid controls the approximation error

of the solution. While a coarse mesh introduces significant numerical diffusion, excessively refining the grid increases the computational overhead with diminishing returns in physical accuracy. Therefore, it is necessary to identify an optimal grid density that sufficiently captures the dominant aerodynamic structures without imposing an additional computational burden for subsequent transient multiphase simulations. The topological details of the evaluated numerical meshes were outlined in the preceding chapter.

Methodology and Time-Averaging

Because the continuous flow field is transient and characterized by a quasi-stable, asymmetric swirling core, comparing instantaneous flow snapshots across different spatial discretizations would yield inconsistent conclusions. To ensure a comparative baseline, the spatial profiles must be evaluated using time-averaged fields.

The procedure for each candidate mesh involved a two-stage integration process. First, the simulation was run for a duration equivalent to one complete residence time of the gas phase to allow the flow field to develop and equilibrate after initial instabilities. Subsequently, the simulation was extended for a second complete residence time, during which the Eulerian velocity and pressure fields were temporally averaged.

To systematically compare the grid resolutions, spatial data from these time-averaged fields were extracted along radial lines spanning the entire chamber diameter at two axial elevations: immediately below the primary atomization nozzle (Figure 5.6) and directly above the conical discharge section (Figure 5.7).

Flow Field Analysis: Near-Nozzle Region

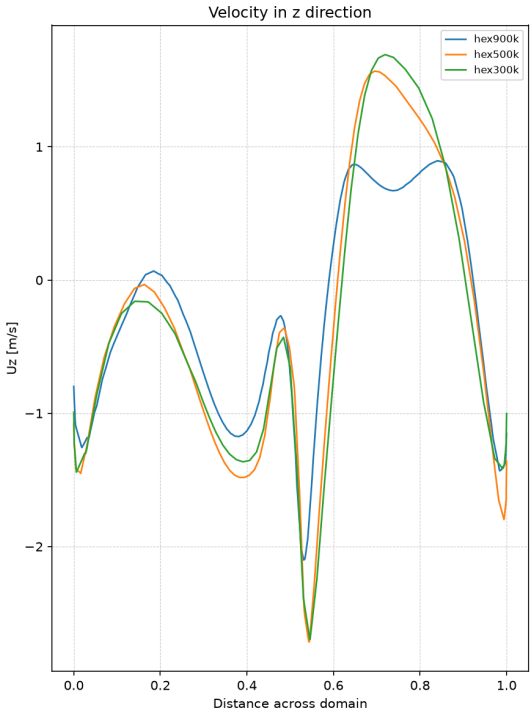
The flow profiles in the dryer are characteristic of a strongly vortex-dominated confined flow. The flow topology near the nozzle exhibits pronounced asymmetry. Conversely, the flow field above the conical base demonstrates a more stabilized, symmetrical profile.

Analysis of the axial velocity (U_z) below the nozzle (Figure 5.6a) indicates a downward-directed flow at the periphery, transitioning to a strong upward recirculation zone between the 0.6 m and 0.9 m radial coordinates. This confirms that the internal hydrodynamics are not unidirectional; significant internal recirculation zones exist, which increase the residence time of the discrete phase. The radial velocity (U_x) plot (Figure 5.6b) shows velocity vectors predominantly directed toward the chamber walls, with localized regions drawn back toward the central vertical axis.

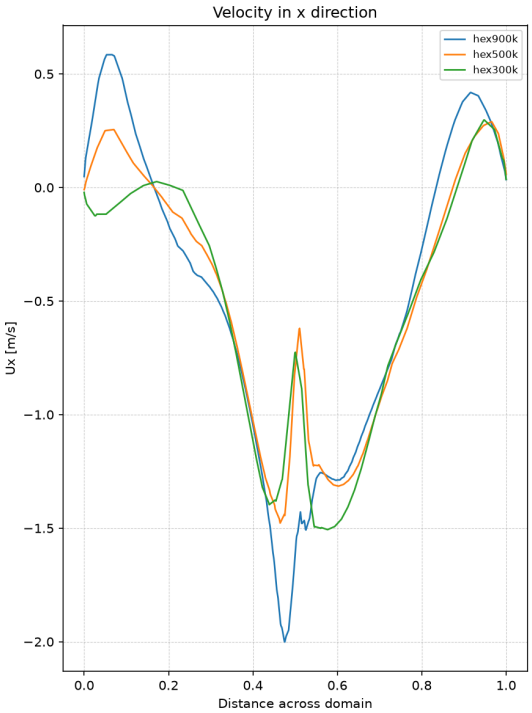
Most notably, the tangential (swirl) velocity (U_y) profile (Figure 5.6c) illustrates the severe rotation of the continuous phase. The magnitude of the tangential velocity significantly exceeds both the axial and radial components, peaking in the annular region adjacent to the chamber walls. From a multiphase perspective, this indicates that the Lagrangian droplets will be subjected to significant tangential acceleration. The resulting centrifugal forces will drive the discrete phase toward the walls, suggesting that localized zones of high particle concentration — and potential wall fouling — should be anticipated.

The static pressure profile (Figure 5.6d) reveals a classical parabolic gradient consistent with a Rankine vortex structure [33]. Maximum pressure is observed near the bounding walls due to centrifugal compression, while a pronounced pressure deficit occurs at the geometric center, corresponding to the low-velocity vortex core.

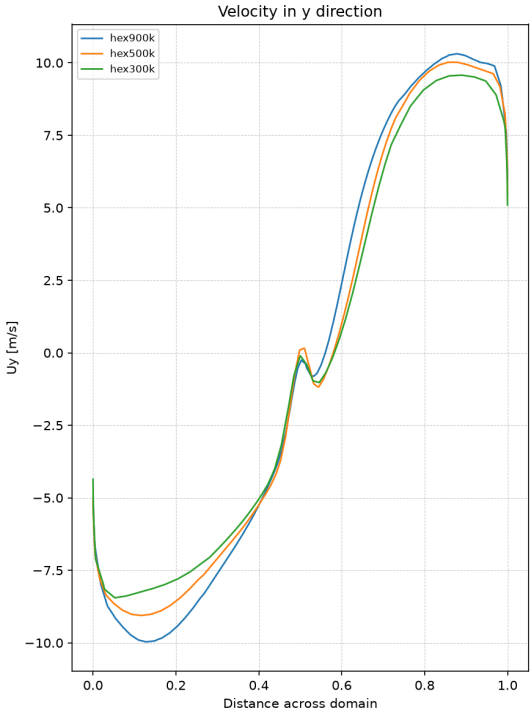
Across all evaluated grids, the macroscopic shapes of the solution profiles are highly consistent, with discrepancies isolated primarily to the absolute peak values within high-shear regions. The most important parameter for defining droplet trajectories, the tangential velocity (U_y), demonstrates good grid convergence. For the axial (U_z) and radial (U_x) components, the coarse and intermediate meshes exhibit strong agreement, while the finest mesh resolves minor localized deviations (e.g., near the 0.7 m mark for U_z and the 0.4 m mark for U_x). The pressure field similarly shows good agreement between the intermediate and fine meshes, with the coarsest mesh slightly over-predicting the central pressure deficit. Nonetheless, this relative discrepancy remains insignificant.



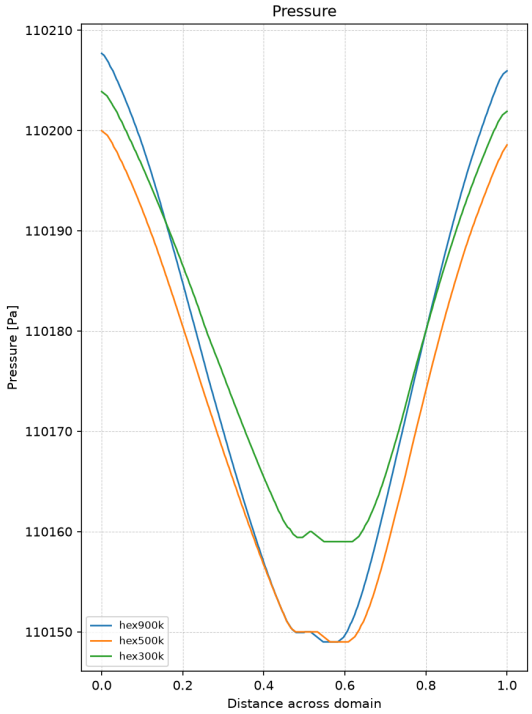
(a) Z-direction velocity below the nozzle



(b) X-direction velocity below the nozzle

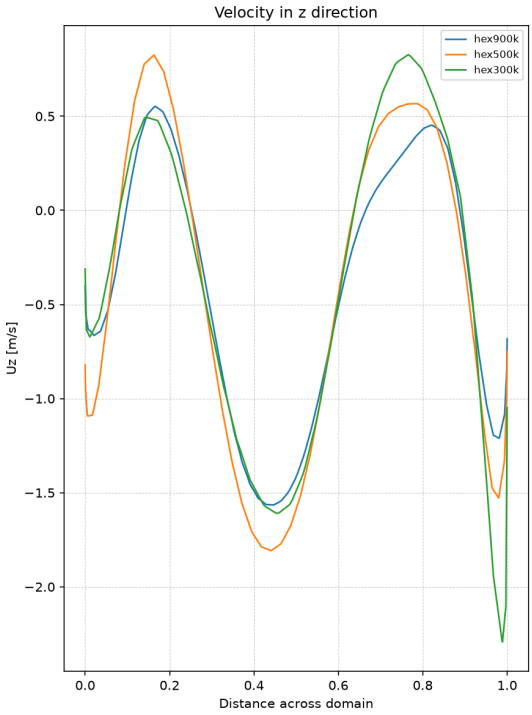


(c) Y-direction velocity below the nozzle

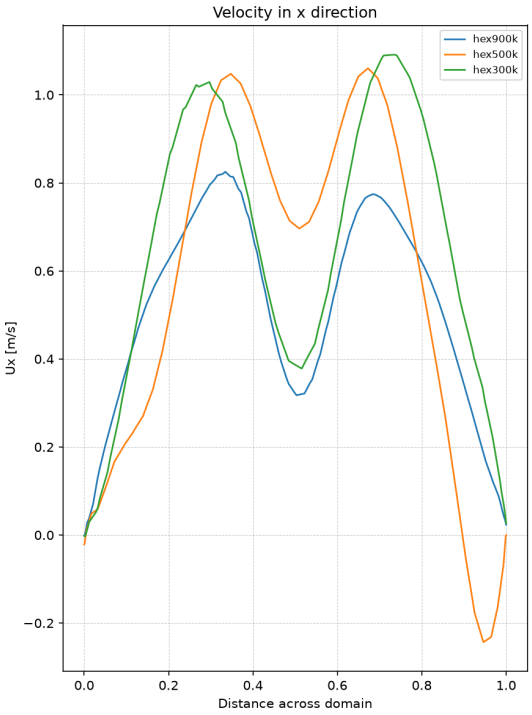


(d) Pressure below the nozzle

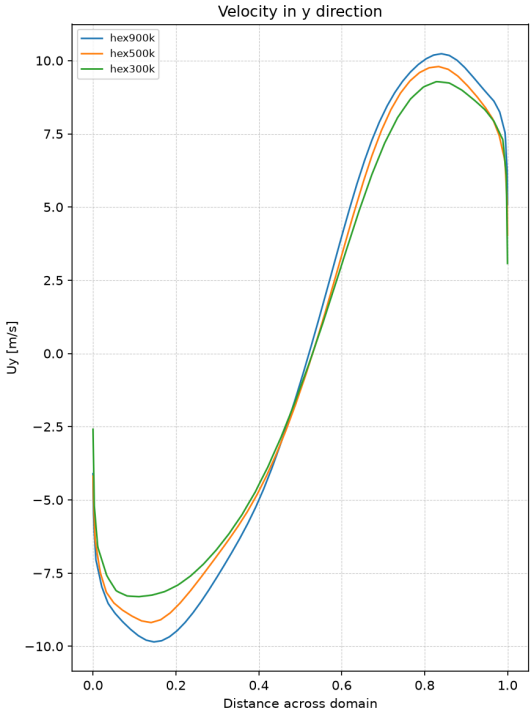
Figure 5.6: Velocity and pressure comparison across meshes below the nozzle.



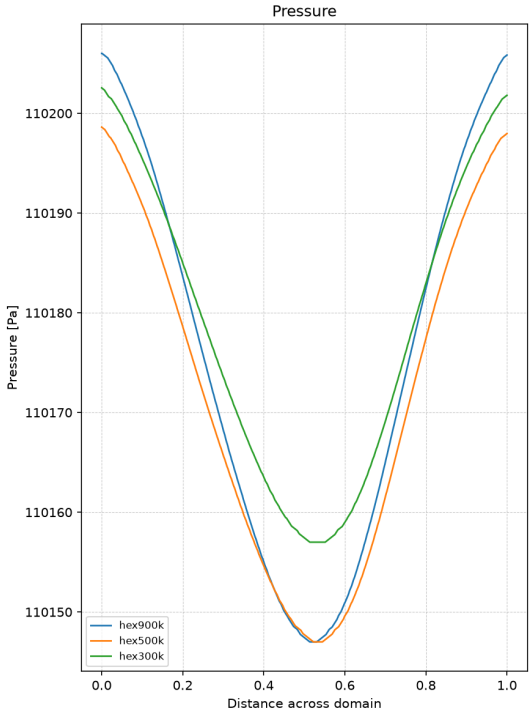
(a) Z-direction velocity above the conical base



(b) X-direction velocity above the conical base



(c) Y-direction velocity above the conical base



(d) Pressure above the conical base

Figure 5.7: Velocity and pressure comparison across meshes below above the conical base.

Flow Field Analysis: Conical Base Region

A parallel assessment was conducted for the profiles extracted above the conical discharge section (Figure 5.7). In this lower domain, the swirling flow has largely stabilized. Furthermore, the geometric expansion and the relatively coarser mesh strategy utilized in this region act as a spatial filter, dampening localized micro-instabilities.

The radial and axial profiles (Figures 5.7b and 5.7a) exhibit a high degree of symmetry. Spatial convergence in this region is robust, with variations strictly limited to absolute peak magnitudes. For instance, the intermediate mesh captures a slight flow reversal around the 0.9 m mark in the radial plot that is smoothed out in alternate grids. Nevertheless, both the tangential velocity (Figure 5.7c) and static pressure (Figure 5.7d) confirm stable grid independence.

Final Grid Selection

The ultimate objective of this spatial discretization is not to analyze the continuous phase in isolation, but rather to establish a reliable hydrodynamic transport medium for the subsequent coupled Eulerian-Lagrangian modeling. While minor localized variations exist between the intermediate and finest grids, these discrepancies are insufficient to alter the macroscopic quantities of interest, specifically the overall particle RTDs and spatial deposition patterns. Furthermore, upon activation of the two-way phase coupling, the injection of the discrete phase will act as a momentum sink, introducing a degree of physical dampening that further stabilizes the continuous flow field.

Based on these physical insights and the results of the spatial convergence analysis, the intermediate mesh consisting of roughly 590k hexahedral elements was selected for all production runs. This topology provides an optimal engineering compromise between spatial resolution of the dominant swirling hydrodynamics and computational throughput. All production simulations were executed within a Windows Subsystem for Linux (WSL) environment on a dedicated workstation equipped with an AMD EPYC 9834X 32-core processor and 192 GB of system memory.

The domain was partitioned using the automatic `scotch` decomposition algorithm across 12 physical CPU cores, yielding a targeted workload of approximately 49k cells per core. This setup aligns with established high-performance computing guidelines for parallel finite-volume solvers ($\approx$ 50k cells/core), maximizing parallel execution speed while avoiding the memory bandwidth saturation and inter-core MPI boundary communication overhead associated with higher core allocations on meshes of this scale.

5.2 Verification of Multiphase Hydrodynamics

Following the mesh sensitivity study and the establishment of a stable single-phase flow field, the investigation advanced to the verification of the Eulerian-Lagrangian two-way coupled hydrodynamic tracking simulations. While the results will be analyzed in the subsequent chapter, this section focuses on the numerical verification of the multiphase architecture. The integrity of the discrete phase modeling is evaluated against two primary metrics: the spatial distribution of the particle volume fraction, to justify the coupling regime, and the sensitivity of the solution to the Lagrangian discretization meaning the parcel count independence.

Particle Volume Fraction and Coupling Assumptions

The first verification metric, the Eulerian volume fraction field of the discrete phase (α_p), is necessary for validating the baseline coupling assumptions. If the local volume fraction significantly exceeds the dilute regime threshold across large regions of the computational domain, the standard two-way coupling assumption is invalidated. Such a violation would necessitate the implementation of a four-way coupling scheme or a Multiphase Particle-In-Cell approach [34] to accurately resolve particle-particle collisions and dense-phase interactions.

To evaluate this, three simulations were executed utilizing an identical parcel injection rate but varying the total mass flow rate of the liquid feedstock (Small, Intermediate, and Large). Each case was allowed to reach a quasi-steady state via an 11-second initialization phase, after which the temporal evolution of the

particle volume fraction was analyzed over a subsequent 11-second integration period. The objective was to quantify the number of computational cells where the local particle volume fraction exceeded the dense-flow threshold of 0.1%. The results of this analysis are summarized in Table (5.1).

Table 5.1: Quantification of computational cells violating the two-way coupling dilute assumption.

Slurry Mass Flow Rate	**# cells $\alpha_p > 0,1\%$**	**Total cell count share**
5 kg/h	412	0.07%
10 kg/h	1301	0.22%
15 kg/h	2544	0.43%

A volumetric threshold analysis of the Eulerian particle fraction confirmed that, across all evaluated mass flow rates, more than 99.5% of the domain operates within the dilute regime, thereby satisfying the prerequisite for two-way coupling. As anticipated, highly localized dense zones were identified strictly in the near-wall regions, visible in Figure (5.8), where particles accumulate due to centrifugal acceleration. While the two-way coupling framework neglects particle-particle collisions within these boundary layers, this limitation was deemed acceptable as it does not compromise the core interphase drying kinetics or the macroscopic Residence Time Distribution of the spray.

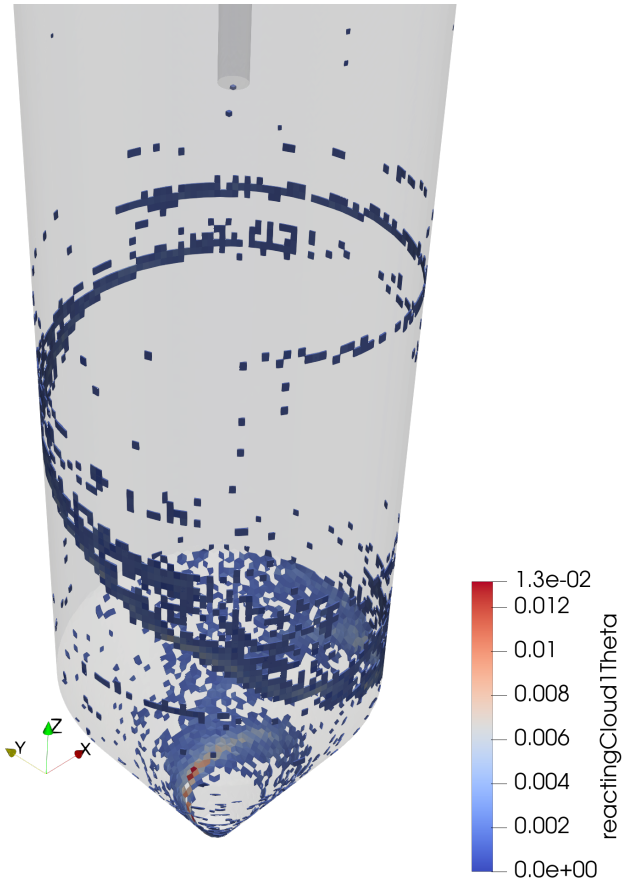


Figure 5.8: Spatial distribution of computational cells where the local particle volume fraction violates the two-way coupling assumption.

Lagrangian Discretization and Parcel Independence

The second verification metric addresses the Lagrangian discretization, defined as the statistical factor determining the number of physical droplets represented by a single computational parcel. For a constant mass flow rate, the continuous feedstock can be arbitrarily discretized into varying parcel injection rates. A numerically robust Eulerian-Lagrangian simulation must exhibit statistical independence from this parcel count; specifically, macroscopic quantities of interest - such as the RTD and the continuous phase velocity field - must not deviate when the number of tracked discrete elements is altered.

To assess parcel independence, three equivalent simulations were prepared utilizing injection rates of 20,000, 35,000, and 50,000 parcels per second. Consequently, the statistical mass weighting per parcel varied inversely across the cases. Following flow stabilization, the temporal histories of the discrete phase and the time-averaged Eulerian flow fields were extracted for comparison.

Parcels are injected from an atomizer located at the top of the chamber, propagating downward under the influence of gravitational body forces and aerodynamic drag from the swirling gas phase. Because particle trajectories are subject to stochastic turbulent dispersion and variable injection parameters, the total time a particle spends within the domain is a random variable. Therefore, residence time cannot be treated as a deterministic scalar but must be evaluated as a statistical distribution.

The resulting RTD profiles for the three discretization levels are presented in Figure (5.9). The superimposed density curves exhibit near-perfect agreement, proving that the statistical representation of the spray has converged and the macroscopic transport behavior is independent of further Lagrangian refinement.

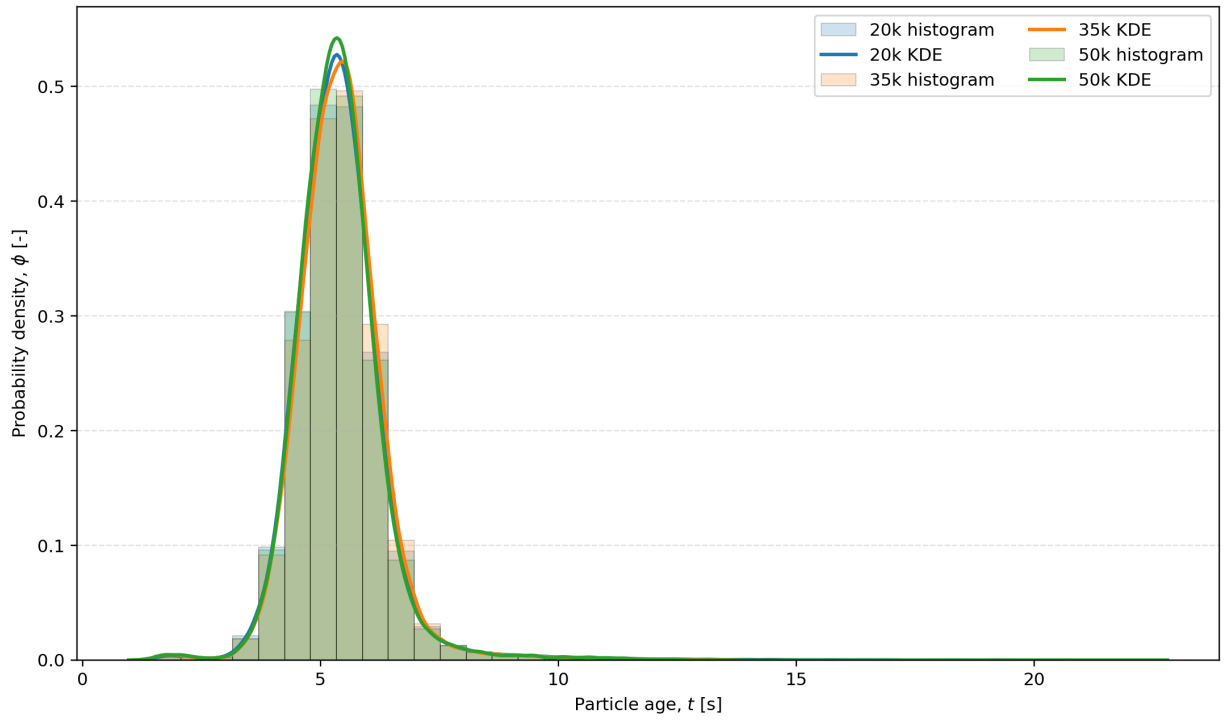


Figure 5.9: Comparison of RTD across simulations with varying Lagrangian parcel discretization levels.

The spatial independence of the numerical setup is further supported by the time-averaged continuous phase velocity and pressure fields, presented in Figure (5.10). Across all discretization levels, the Eulerian fields demonstrate good agreement, indicating that the dispersed phase imparts a consistent, aggregated aerodynamic feedback onto the continuous phase regardless of the parcel count.

Notably, Figure (5.10a) highlights the significant hydrodynamic impact of the two-way coupling. Immediately downstream of the atomization nozzle, the injection of the discrete phase acts as a localized

momentum sink. This intense interphase momentum exchange alters the axial velocity profile (U_z) of the gas, demonstrating the necessity of the fully coupled framework.

Having verified both the validity of the dilute volume fraction assumption and the numerical independence of the Lagrangian discretization, the underlying multiphase framework is considered mathematically stable and physically sound. The verified model provides a foundation for the detailed analysis of heat and mass transfer phenomena in the subsequent chapters.

5.3 Verification of crustReactingParcelFoam

As established in the preceding chapter, accurately modeling solvent evaporation into a superheated steam environment, coupled with transient solid crust formation, necessitated the development of a custom phase-change library and a modified Eulerian-Lagrangian solver. To ensure numerical stability of these implementations prior to executing full-scale, fully coupled multiphase simulations, a verification and validation study was required.

To systematically manage the computational complexity, the verification process was initiated by developing an independent, standalone Python script designed to numerically integrate the isolated heat and mass transfer governing equations. The output of this analytical model served as a baseline to verify the C++ implementation within the OpenFOAM framework. The phase-change model was validated against established experimental data from contemporary literature regarding superheated steam drying. Finally, the source code was profiled and optimized to ensure computational feasibility for large-scale transient simulations.

5.3.1 Baseline verification

The baseline verification involved simulating the drying trajectory of a single, isolated particle suspended in a superheated steam environment. The process kinetics were governed by the mathematical formulations detailed in Chapter 3. The specified boundary and initial conditions for this baseline case were defined as follows:

- **Geometry**: A two-dimensional, elongated vertical channel.
- **Continuous Phase (Steam)**: An upward-directed superheated steam flow with an inlet temperature of 473 K at standard atmospheric pressure and initial velocity of 1 m/s corresponding to Reynolds number equal 1.44.
- **Discrete Phase (Particle)**: A single 50 µm composite droplet (consisting of liquid water and a suspended solid fraction) initialized at a uniform temperature of 300 K.

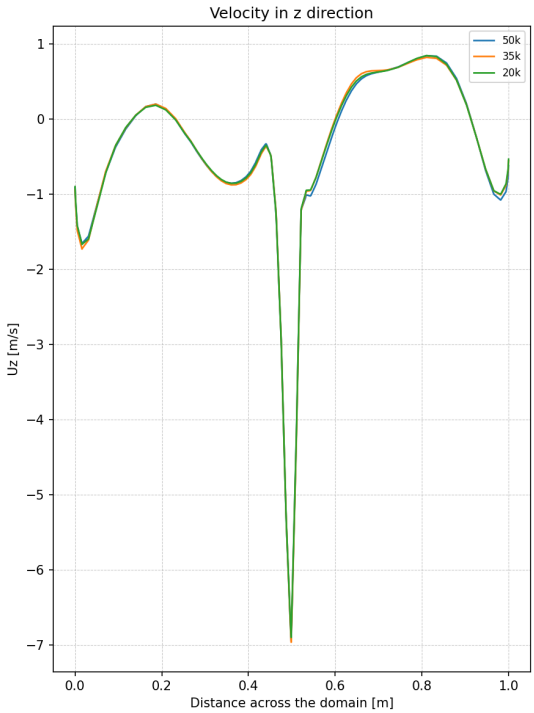
The numerical script employs a time-stepping scheme to iteratively resolve the interphase heat fluxes and corresponding mass transfer rates, updating the thermophysical and morphological properties of the particle at each integration step. The resulting temporal evolution of these properties is presented in Figure (5.11).

The temperature profile in Figure (5.11) clearly delineates the three characteristic kinetic stages of superheated steam drying. The first stage represents the sensible heating of the subcooled droplet. Upon reaching the saturation temperature, the particle enters the constant-rate evaporation period, characterized by isothermal conditions as all convective heat flux is consumed by the latent heat of vaporization.

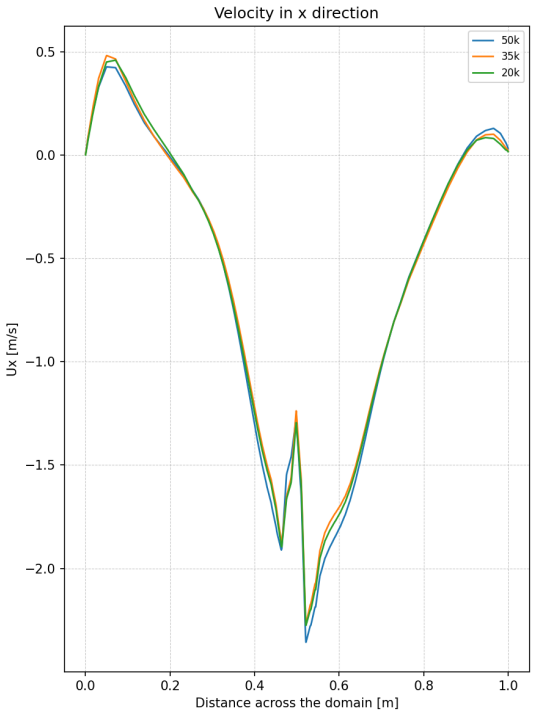
Following the critical moisture threshold, a solid crust precipitates. During this falling-rate period, internal mass transfer resistance decelerates evaporation, causing the particle temperature to elevate toward the bulk steam temperature. As thermal equilibrium is achieved between the particle surface and the surrounding gas, interphase heat transfer asymptotically approaches zero.

Analysis of the water mass fraction profile confirms that the moisture content remains constant during the brief initial heating phase. As explicitly defined in the theoretical framework, this represents a mathematical simplification; the transient mass-gain associated with initial steam condensation is neglected to enhance numerical stability, and the droplet is assumed to heat solely via sensible convection.

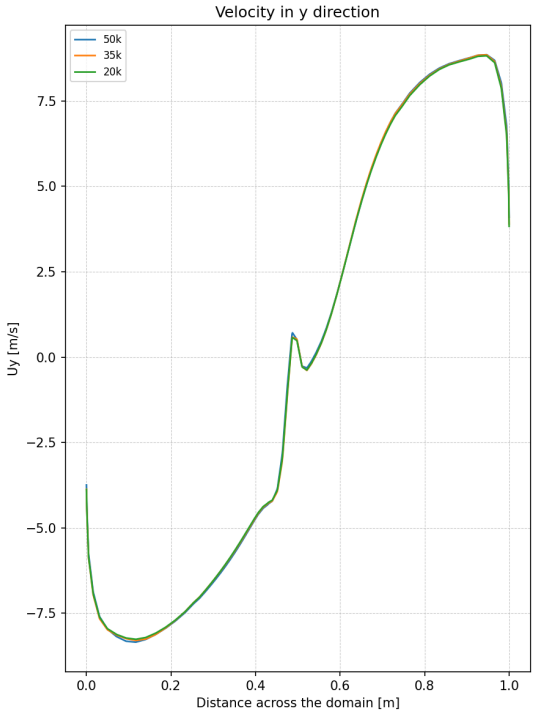
Subsequent to this heating phase, the particle undergoes the constant-rate drying period, exhibiting a near-linear reduction in moisture content. The onset of crust formation triggers the falling-rate period,



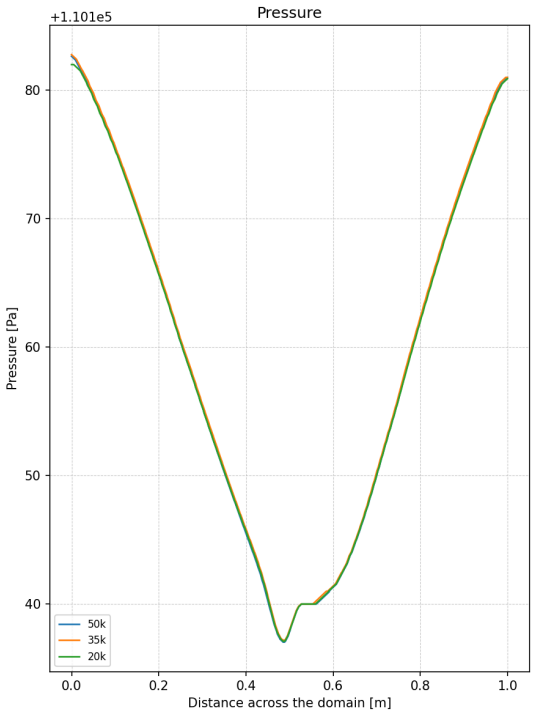
(a) Z direction velocity below the nozzle



(b) X direction velocity below the nozzle



(c) Y direction velocity below the nozzle



(d) Pressure below the nozzle

Figure 5.10: Velocity and pressure fields for 3 different parcel discretization levels.

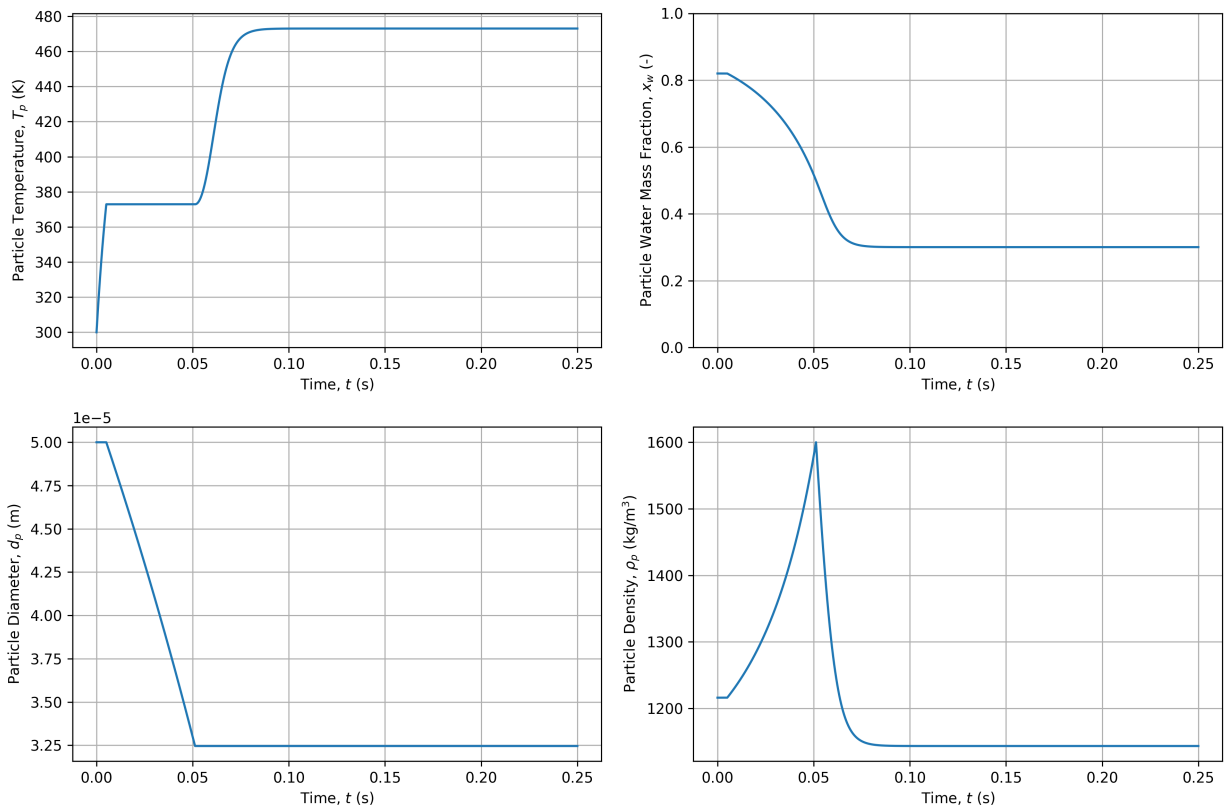


Figure 5.11: Particle properties evolution.

during which the vaporization rate diminishes and the moisture content asymptotically approaches a final equilibrium state determined by the critical moisture boundary conditions.

The particle diameter profile illustrates ideal shrinkage behavior during the constant-rate period, reflecting the continuous depletion of unbound surface moisture. However, at the transition point corresponding to crust formation, macroscopic geometric shrinkage ceases. The external diameter becomes fixed, and subsequent moisture removal leads to the development of an internal porous solid matrix.

This morphological evolution directly correlates with the observed density profile, which exhibits a sharp maximum precisely at the point of crust formation. During the initial shrinkage phase, the preferential evaporation of the lower-density solvent progressively increases the mass fraction of the denser solid constituents, driving an increase in overall particle density. Once the geometric volume becomes fixed by the rigid crust, the continued extraction of internal moisture generates void spaces (porosity), causing the effective bulk density of the particle to decay toward a final asymptotic limit.

To verify the custom Eulerian-Lagrangian implementation, an OpenFOAM simulation was configured with boundary and initial conditions strictly matching the Python baseline model. The C++ source code was iteratively refined to ensure numerical consistency with the analytical baseline, yielding the comparative results depicted in Figure (5.12).

The temporal evolutions of particle temperature, moisture content, and diameter computed by the custom OpenFOAM solver exhibit good agreement with the baseline analytical profiles. The only noticeable deviation occurs in the absolute values within the density profile. This discrepancy is a physical artifact of OpenFOAM utilizing more sophisticated, temperature-dependent polynomial regressions for fluid and solid densities, whereas the baseline script employed simplified constant parameters. Ultimately, the comprehensive alignment of the coupled transport dynamics confirms the successful verification of the custom phase-change library and establishes its reliability for full-scale simulation.

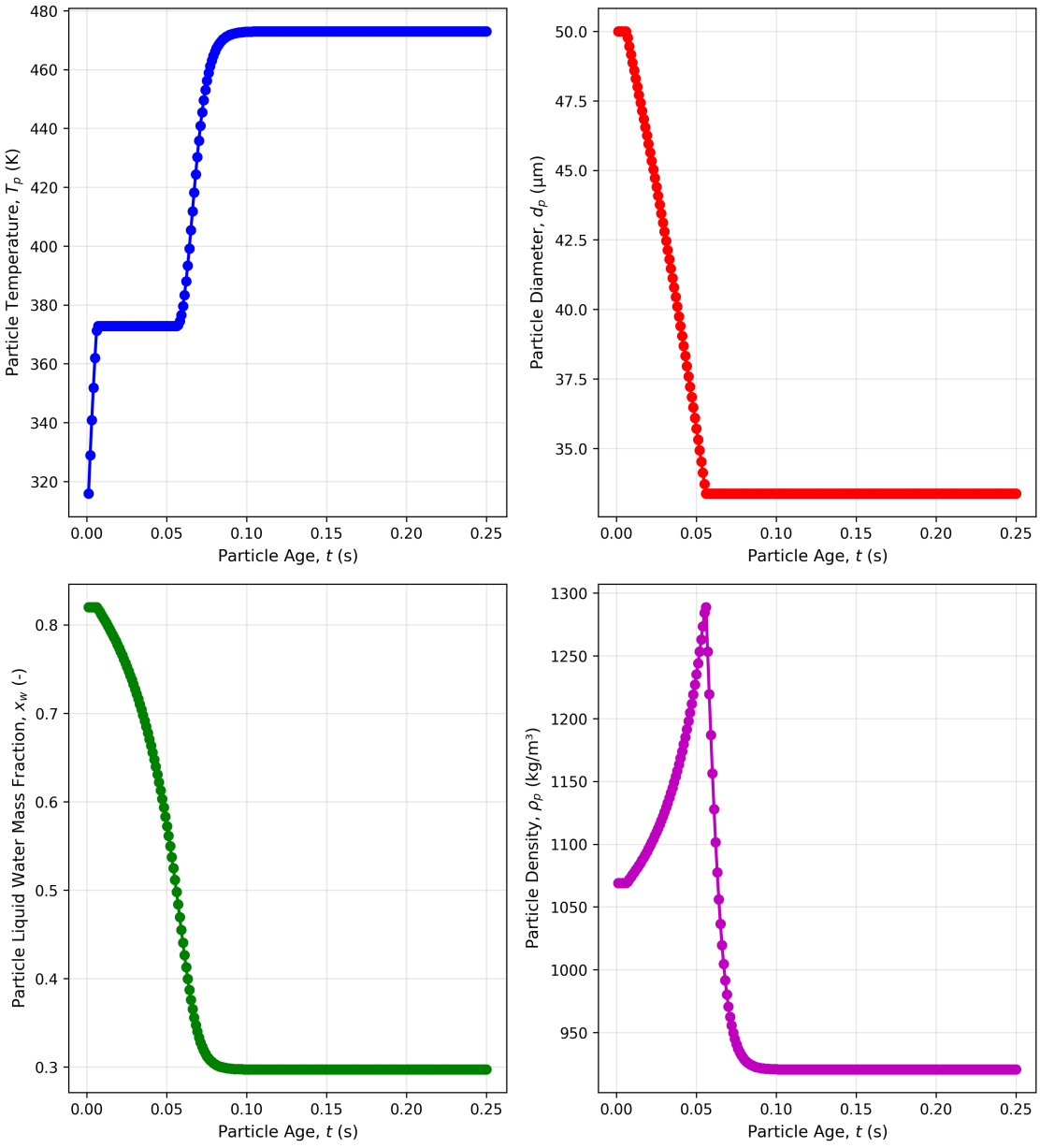


Figure 5.12: OpenFOAM solver simulation results of baseline study.

5.3.2 Code Validation

To validate the physical fidelity of the newly developed phase-change library, the numerical predictions were checked against benchmark experimental data. Due to the scarcity of comprehensive empirical studies detailing single-droplet superheated steam drying, the validation was performed using the dataset published by Lee et al. (1968) [35]. In this study, the transient diameter reduction of a suspended water droplet evaporating within a superheated steam environment was continuously measured under well-defined hydrodynamic and thermodynamic conditions.

To ensure consistency with the experimental boundary conditions, the specific empirical correlation for the Nusselt number proposed by the authors of the reference study was integrated into the OpenFOAM solver framework, defined as:

$$\mathrm{Nu} = 2 + 0,74\,\mathrm{Re}^{0,5}\mathrm{Pr}^{0,33} \tag{5.1}$$

The reference investigation evaluated the vaporization kinetics utilizing a constant free-stream steam velocity while systematically varying the degree of thermal superheat ($\Delta T = T_\infty - T_{sat}$). The temporal evolution of the droplet diameter predicted by the customized OpenFOAM solver was compared against the semi-empirical solutions derived from the experimental data by the original authors. This comparison is presented in Figure (5.13).

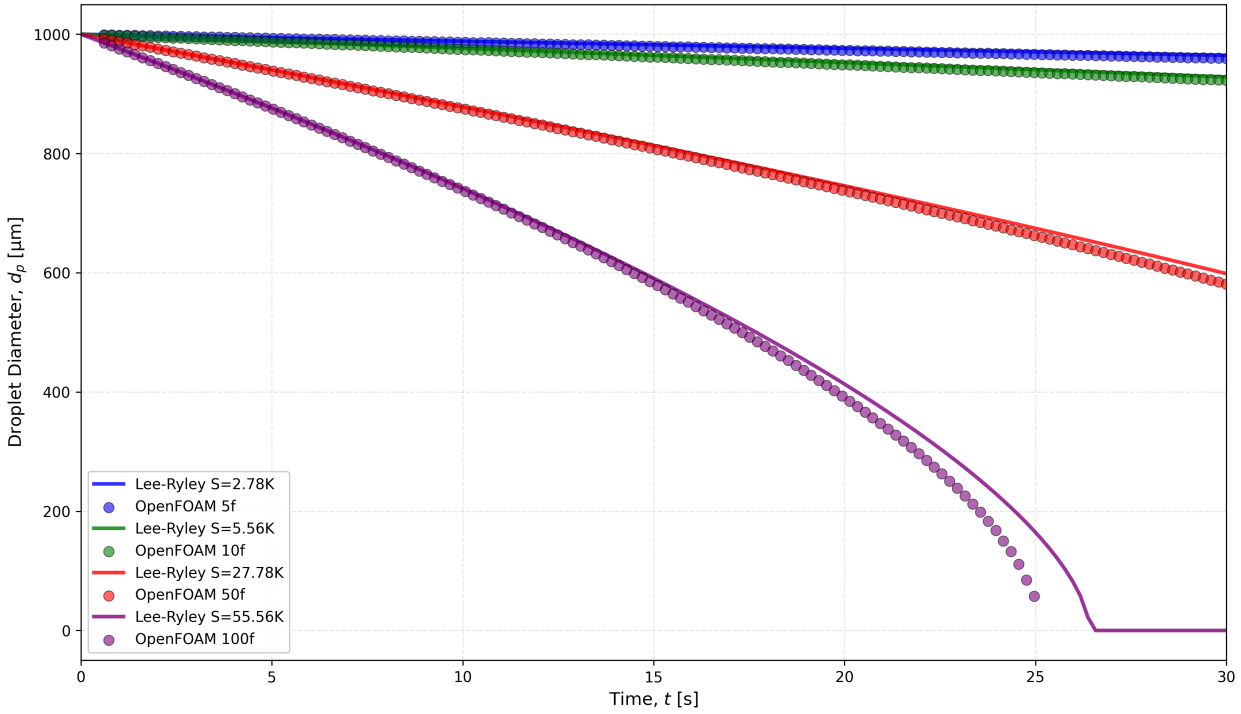


Figure 5.13: Comparison of the temporal droplet diameter evolution between the numerical solver predictions and the semi-empirical benchmark data.

For low to moderate degrees of superheat, the numerical predictions exhibit near-perfect agreement with the benchmark data. A minor divergence emerges at the highest evaluated superheat of 55.56 K. Under these specific conditions, the numerical model predicts a marginally accelerated evaporation rate, resulting in total droplet depletion approximately 1.0 second earlier than the benchmark projection. Given the inherent uncertainties in high-temperature transport properties and the otherwise robust alignment across multiple thermal gradients, the custom phase-change library is considered successfully validated for simulating pure-vapor droplet evaporation.

Due to a lack of available experimental data characterizing transient solid crust formation in superheated steam environments, the falling-rate kinetics could not be subjected to direct empirical validation. Specifically, the critical moisture content (X_{cr}) - the parameter triggering the morphological phase transition - is highly material-dependent and difficult to estimate analytically. To address this uncertainty, a parametric sensitivity study will be conducted in subsequent sections to quantify the macroscopic impact of varying the critical moisture threshold on the final drying kinetics and residence time distributions.

5.3.3 Computational Profiling and Code Optimization

Despite the successful physical validation of the custom phase-change library, initial test simulations exhibited prohibitively slow execution speeds. To systematically identify the underlying numerical bottlenecks within the newly implemented heat and mass transfer models, the C++ source code was subjected to computational profiling utilizing Valgrind on a simplified validation case.

In the initial implementation, the convective heat transfer model necessitated the evaluation of the thermal conductivity of the continuous gas phase. This parameter was originally retrieved utilizing standard OpenFOAM thermodynamic lookup functions. However, OpenFOAM's primary continuous-phase thermodynamic libraries are designed and optimized for Eulerian volume fields. Consequently, invoking a standard property lookup from a discrete Lagrangian parcel triggered a global evaluation; the solver computed the complex polynomial thermodynamic functions for every computational cell across the entire three-dimensional mesh, allocated the results to a temporary volume field, and only then extracted the requisite localized value.

This mechanism induced a severe computational bottleneck. Profiling analysis via Valgrind demonstrated that this single operation forced the CPU to execute a massive volume of redundant thermodynamic calculations, ultimately consuming over 61% of the total processing time.

To resolve this algorithmic inefficiency, the global mesh evaluation was entirely deprecated within the custom library. It was replaced by referencing a pre-interpolated variable natively available within the OpenFOAM Lagrangian framework, which directly maps the continuous-phase thermal conductivity to the discrete particle's surface film boundary. This modification successfully shifted the property evaluation from a global volumetric operation to a localized cell-point lookup, completely eliminating the redundant thermodynamic calls and ensuring the solver's computational viability for full-scale transient simulations.

Chapter 6

Results and Discussion

6.1 Passive Particle Transport in Steam Environment

This section is concerned with the macroscopic behavior of the dispersed phase. Specifically, this analysis investigates the influence of injection parameters and operating conditions on the resulting Residence Time Distributions. Furthermore, representative particle trajectories and spatial deposition patterns along the drying chamber walls are evaluated.

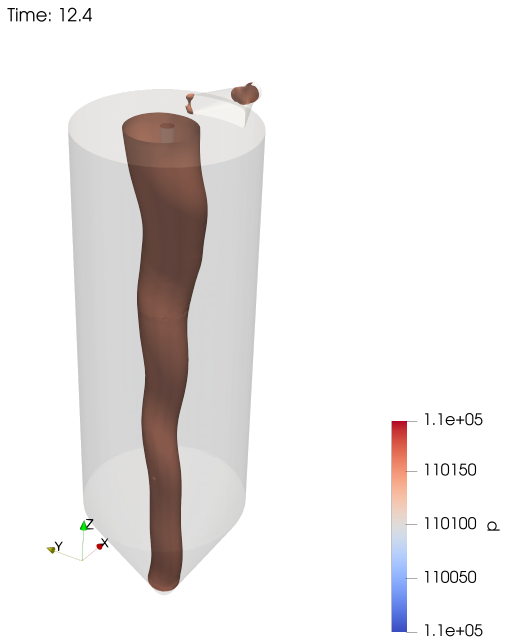
6.1.1 Effect on the Continuous Phase Hydrodynamics

Within the two-way coupled Eulerian-Lagrangian framework, the discrete phase is not only passively advected by the carrier gas; rather, the particles exert a reciprocal aerodynamic influence on the continuous phase. Functioning as localized momentum sources and sinks, the injected droplets accelerate or decelerate the surrounding steam, thereby modifying the baseline flow fields established during the single-phase analysis.

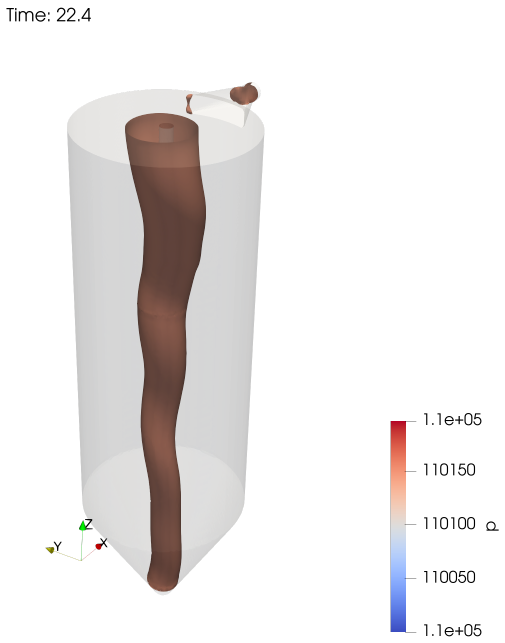
The impact of the dispersed phase on the continuous flow field is illustrated in Figure (6.1). In the uncoupled single-phase simulations, the Central Recirculation Zone exhibited pronounced temporal pulsations while being anchored by the nozzle lance. The introduction of the discrete phase effectively dampens these transient oscillations. An examination of the pressure swirl isosurfaces reveals that the upper diameter of the vortex expands to completely engulf the atomization lance, subsequently tapering as it propagates axially downward through the chamber. Furthermore, the volumetric pulsations of the vortex are largely eliminated; temporal snapshots of the pressure isosurfaces indicate that the CRZ maintains a quasi-steady, continuous topology in the presence of the particle spray.

The time-averaged pressure contour largely mirrors the profile observed in the single-phase study, though it demonstrates a higher degree of axisymmetry, albeit with a residual spatial skew. A similar stabilizing effect is evident in the velocity contours. While the bluff-body wake region trailing the nozzle lance persists, its volumetric footprint is noticeably reduced. The velocity magnitude contours also indicate the aerodynamic footprint of the particle injection cone. Immediately downstream of the atomizer, a localized region of flow acceleration is generated; particles injected at high initial velocities transfer their kinetic energy to the adjacent continuous phase, forcing the entrained steam to accelerate axially downward.

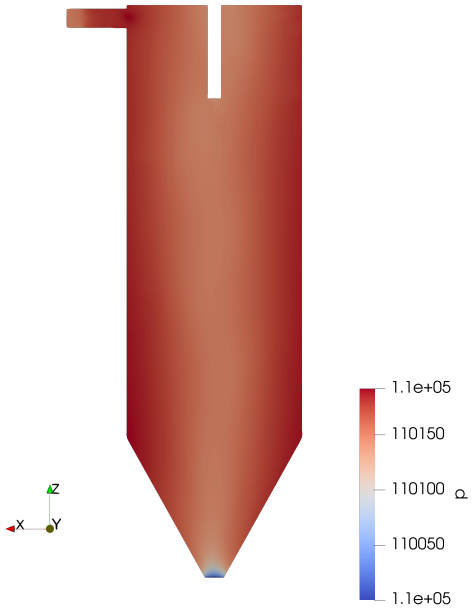
Overall, while two-way coupling induces observable modifications to the localized flow fields, it does not fundamentally reorganize the macroscopic aerodynamics of the drying chamber. Because the system operates well within the dilute regime, the dispersed phase lacks sufficient cumulative momentum to override the dominant swirling structures of the continuous steam phase. Consequently, the carrier gas remains the primary driver of internal transport phenomena. Based on this hydrodynamic hierarchy, it is hypothesized that varying the injection parameters will exert only a marginal influence on the ultimate particle trajectories and Residence Time Distributions, as the overall kinematics will remain subordinate to the bulk gas aerodynamics.



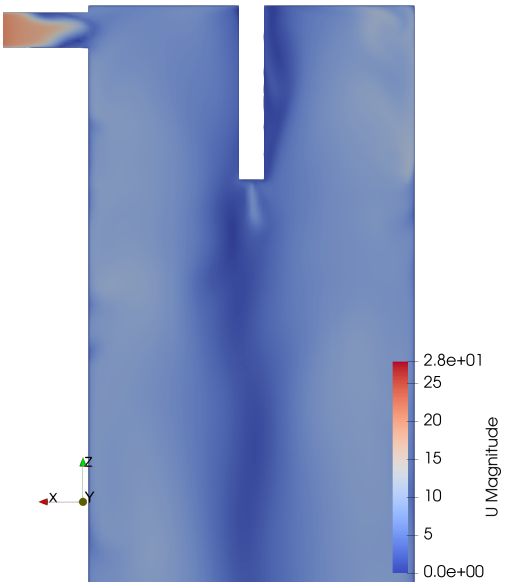
(a) Isosurface of the pressure swirl at $t = 14.4$ s



(b) Isosurface of the pressure swirl at $t = 22.4$ s



(c) Pressure contour



(d) Velocity contour

Figure 6.1: Continuous phase flow fields as modified by the two-way momentum coupling of the dispersed particles.

6.1.2 Particle Kinematics and Spatial Deposition Patterns

The kinematic trajectory of the dispersed phase within the computational domain is governed by the local drag relative to the particle relaxation time. Particles with larger diameters possess significant inertia, characterized by higher Stokes numbers, and therefore exhibit greater deviation from the continuous phase

streamlines. Conversely, finer particles demonstrate higher flow adherence, closely tracking the gas pathlines. This size-dependent spatial deviation is illustrated in Figure (6.2), which maps the trajectories of four representative discrete elements of varying initial diameters.

As depicted in Figure (6.2), the smallest particles exhibit tight adherence to the continuous flow structures. These finer droplets complete multiple high-velocity orbits around the primary injection axis before migrating radially toward the chamber periphery, where they undergo a series of inelastic wall collisions. Consequently, these particles remain entrained within the high-shear, high-velocity regions of the domain for an extended duration.

With increasing particle diameter, the number of orbital revolutions decreases. The heightened mass of the coarser particles results in a proportionally greater centrifugal force, causing them to rapidly overcome the aerodynamic drag and escape the primary swirling core. In the case of particles exceeding 100 µm in diameter, the discrete elements fail to complete a single full orbital revolution. Instead, they are rapidly propelled outward and downward toward the chamber walls, where their kinetic energy is sharply dissipated upon initial inelastic impact.

Interestingly, trajectory analysis reveals that once particles escape the central high-swirl region and reach the boundary layer, their subsequent downward paths become largely independent of initial size. Driven by gravity and the downward axial velocity component, particles descend along the wall in a pronounced helical pattern, experiencing repeated collisions at concentrated spatial coordinates. To quantify this phenomenon, a collision density heatmap was generated by unwrapping the cylindrical wall boundary into a two-dimensional Cartesian plane (azimuthal angle versus axial height), as presented in Figure (6.3).

The localized collision density supports the discrete trajectory observations. The presence of distinct, high-density diagonal bands sloping axially downward is a classic signature of particle roping. This phenomenon occurs as the centrifugal force pins the discrete phase to the boundary wall, while gravitational acceleration and the downward axial vortex core simultaneously drag the concentrated particulate structures toward the discharge hopper.

Furthermore, the heatmap identifies a significant, chaotic high-density zone between the axial coordinates z = 0 m and z = -0.5 m, which corresponds to the geometric transition from the cylindrical chamber body to the conical hopper. The sudden reduction in cross-sectional area forces the helical particulate ropes to compress, elevating the local collision frequency.

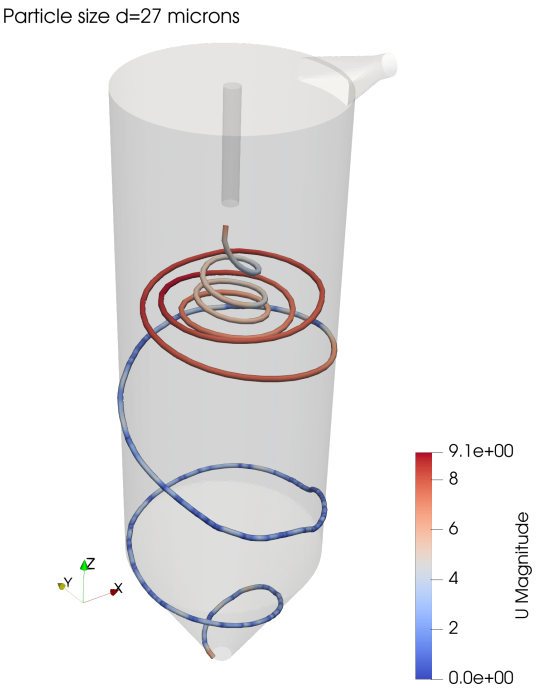
While this spatial mapping highlights regions of high fouling potential, actual wall accretion (fouling) cannot be definitively predicted in the absence of coupled heat and mass transfer. Adhesion depends upon the thermodynamic state of the particle upon impact; if the moisture content has been sufficiently depleted such that a solid crust is fully formed prior to collision, the particle will rebound. This dynamic will be investigated via fully coupled thermal simulations in the subsequent sections.

Ultimately, resolving these Lagrangian trajectories showcases the forces acting upon the discrete phase and provides the spatial foundation for understanding the macroscopic Residence Time Distribution, which is quantitatively analyzed in the following subsection.

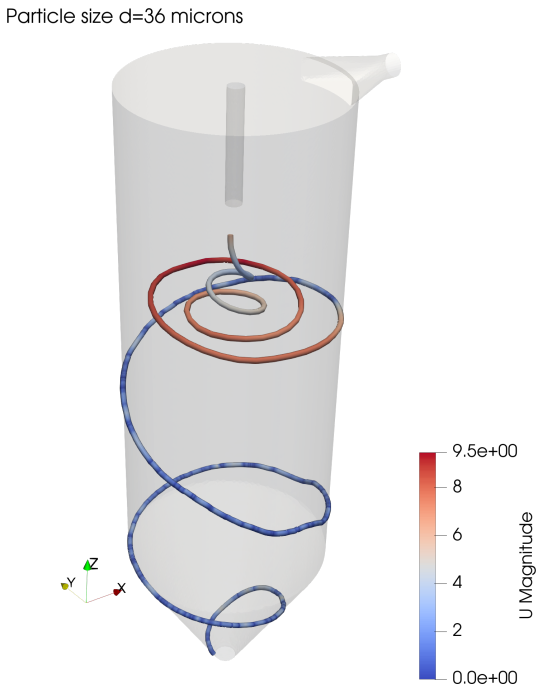
6.1.3 Particle Residence Time Distribution

The residence time distribution of the dispersed phase is an important parameter governing the overall performance of a spray drying unit. The duration a particle resides within the continuous flow field dictates its thermal exposure time, which determines the final product's residual moisture content, structural morphology, and potential for thermal degradation [36]. Evaluating the statistical variance and the mean residence time provides insights into the macroscopic hydrodynamics of the drying chamber. It allows for the identification of anomalous flow phenomena, such as localized dead zones characterized by particle accumulation, excessive backmixing, or short-circuiting, wherein droplets prematurely exit the system before achieving the desired moisture threshold [37].

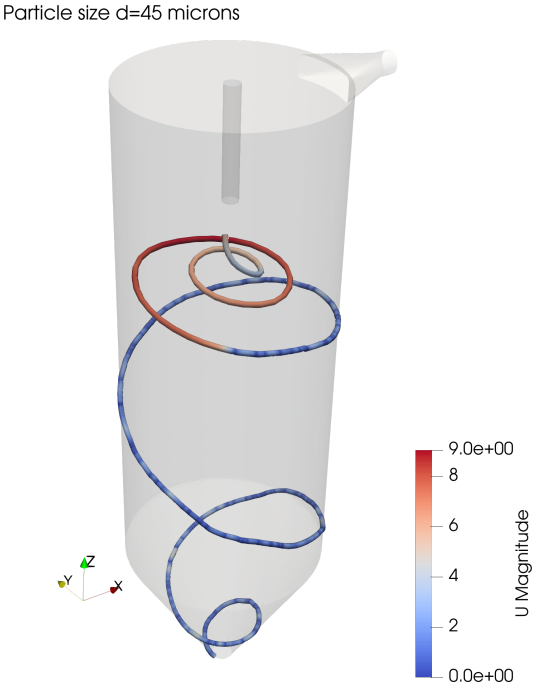
From an empirical perspective, quantifying the RTD within an operational spray dryer remains a complex and capital-intensive endeavor. While standard chemical reactors readily accommodate RTD extraction by conventional tracer pulse injections, capturing the transient dynamics of a multiphase spray necessitates more sophisticated methodologies [38]. Experimental diagnostic techniques typically rely on the injection of specialized markers or pulsed dyes, coupled with advanced optical photomultiplier detection systems [36]. However, these empirical tracer methods are limited by low resolution regarding spray polydispersity; they



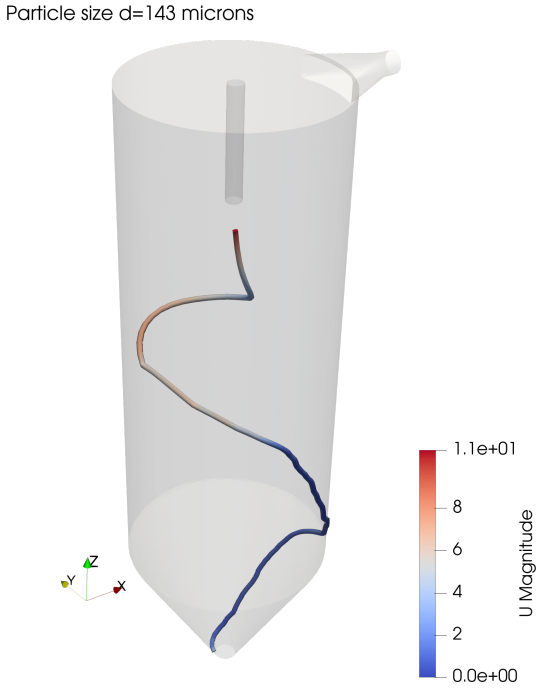
(a) Path traced by a sample particle of size $d = 27$ μm



(b) Path traced by a sample particle of size $d = 36$ μm



(c) Path traced by a sample particle of size $d = 45$ μm



(d) Path traced by a sample particle of size $d = 143$ μm

Figure 6.2: Lagrangian trajectories of individual discrete particles as a function of initial diameter.

yield a macroscopic, bulk-averaged residence time but fail to explicitly delineate how discrete particle size fractions govern the overall RTD. Furthermore, executing experimental trials to systematically evaluate the

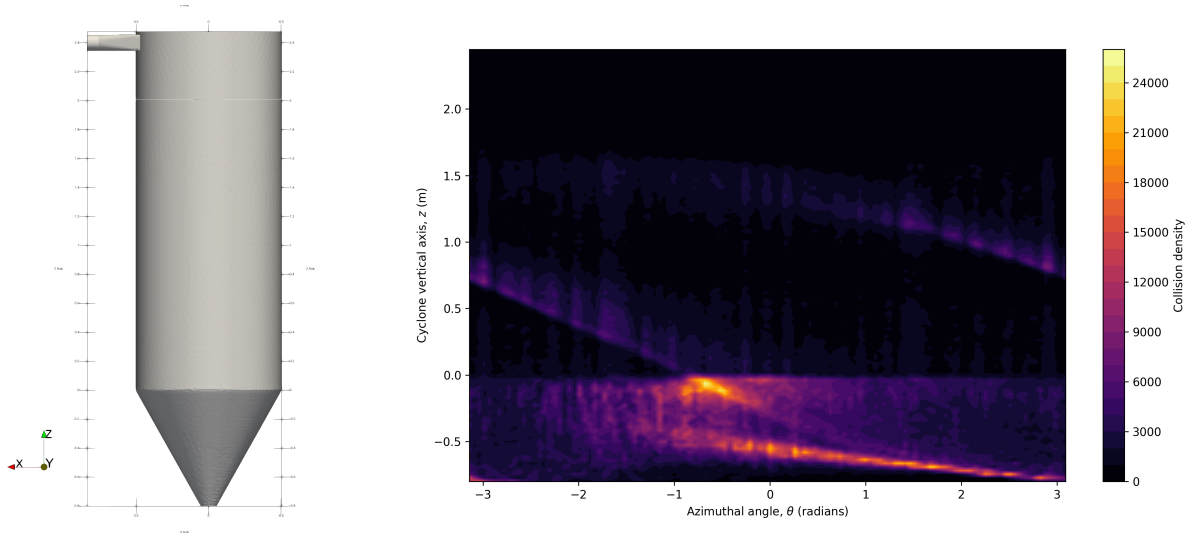


Figure 6.3: Collision heat map.

influence of fluctuating operational parameters or alternative nozzle configurations is both economically challenging and highly time-consuming [39].

CFD frameworks effectively circumvent these empirical constraints, providing the mathematical capability to extract high-fidelity RTD data. The numerical solver integrates the individual spatial trajectories of every Lagrangian parcel from its injection point until it physically exits the computational domain. This deterministic tracking yields a highly precise RTD that can be systematically partitioned into specific particle size classes, thereby enabling a deeper mechanistic understanding of how distinct droplet diameters dictate varying residence times within the continuous phase.

Influence of Injection Angle

As previously detailed, industrial spray drying atomizers generate a polydisperse droplet population characterized by specific initial velocity profiles and spray cone angles. To isolate the aerodynamic influence of the atomizer's geometric spray pattern, a parametric study was conducted to evaluate the sensitivity of the final RTD to the injection cone angle. For this analysis, the initial droplet velocity magnitude and the injected PSD were held constant across all evaluated cases; the spray cone angle served as the only independent variable.

The numerical investigation evaluated three distinct injection configurations: narrow, intermediate, and broad spray angles. Each simulation was initialized for an 11-second integration period to achieve a quasi-steady multiphase flow field. Subsequently, the Lagrangian tracking data was recorded over a secondary 11-second data acquisition phase, during which the individual residence times of the particles escaping through the domain outlet were logged. The superimposed global RTD curves for these cases are presented in Figure (6.4).

An analysis of Figure (6.4) reveals that the global, mass-averaged RTD is virtually invariant with respect to the injection angle. The macroscopic distribution profiles are nearly identical across the three configurations, having a mean residence time centered at approximately 6 seconds. The temporal bounds of the distributions indicate that very few particles reside within the chamber for longer than 10 seconds, while the earliest particle exits occur near the 1.5-second mark. Notably, a minor secondary peak emerges between 1 and 2 seconds; this localized perturbation showcases a degree of aerodynamic short-circuiting within the chamber geometry, wherein a fraction of the dispersed phase prematurely bypasses the primary recirculation zones and exits the domain.

An advantage of the Eulerian-Lagrangian computational framework is the mathematical capacity to decompose this bulk-averaged RTD into discrete, size-specific subpopulations. This segregation is illustrated in Figures (6.5 through 6.7), which presents the specific RTD contributions of the fine and coarse particle

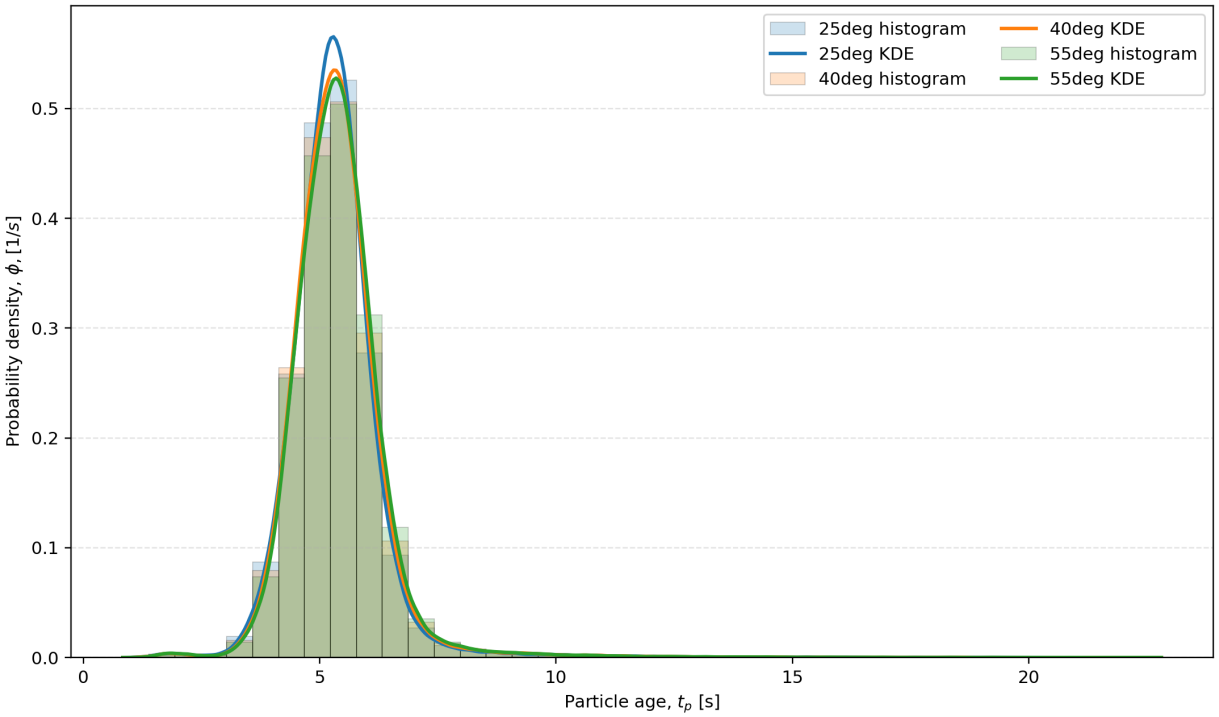


Figure 6.4: Comparison of global RTD curves across narrow, intermediate, and broad injection angles.

fractions.

The decomposed profiles highlight a pronounced separation in kinematic behavior based on particle inertia. On average, the coarse droplet population experiences a prolonged residence time relative to the finer droplets. Due to their lower Stokes numbers, smaller particles closely trace the continuous gas streamlines and are rapidly advected toward the outlet. Conversely, larger particles possess sufficient inertia to decouple from the primary gas flow. These heavier droplets traverse the swirling flow field and impact the chamber walls, undergoing inelastic collisions. This dissipation of kinetic energy alters their transport mechanism; rather than remaining aerodynamically suspended, the coarse particles undergo a slow, gravity-driven sliding motion along the boundary walls toward the discharge hopper, thereby extending their domain residence time.

Across all injection angles, the RTD profile of the fine particle population remains consistent. However, the kinematic response of the coarse particle population goes through a minor morphological change. The large particle RTD is a distinct bimodal distribution, suggesting that this fraction can be further divided into intermediate particles (e.g., sub-100 µm) and extreme-coarse particles (>100 µm).

As the injection angle is broadened, this bimodality becomes more noticeable. In the broad-angle configuration, the two peaks are far apart, whereas they partially blend in the narrow-angle configuration. This phenomenon can be explained by the radial placement of the particles relative to the Central Recirculation Zone. A broader injection angle propels the intermediate particles (sub-100 µm) deeper into the highly swirling vortex core, increasing their entrainment and accelerating their exit relative to the extreme-coarse particles. In contrast, the secondary peak — governed by the extreme-coarse fraction — remains stagnant across all configurations. Because these massive droplets quickly impact the upper cylindrical walls regardless of the initial injection angle, their subsequent boundary-layer descent is decoupled from the central gas dynamics.

In conclusion, the initial spray cone angle has a negligible influence on the macroscopic RTD of the spray dryer under the evaluated operating conditions. Because the volumetric particle size distribution is heavily weighted toward finer droplets, the bulk mass transport remains entirely subordinate to the continuous phase hydrodynamics. The dilute nature of the spray guarantees that the initial injection momentum is rapidly

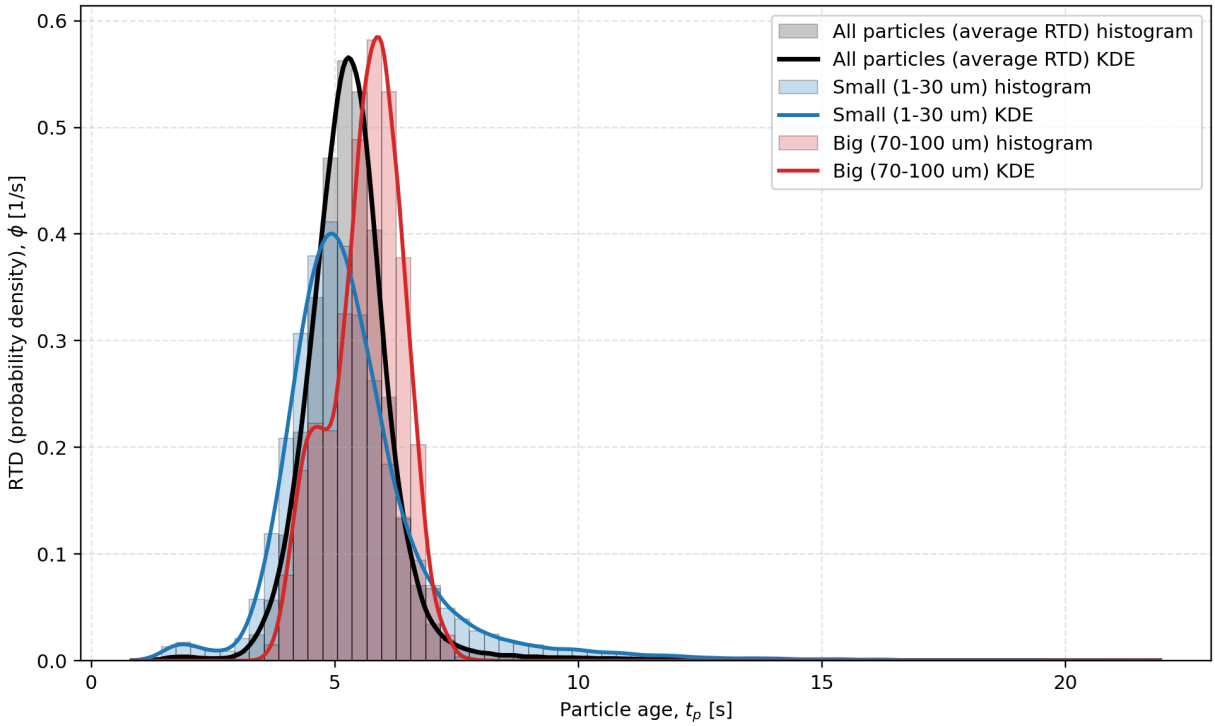


Figure 6.5: Size-segregated residence time distribution for the narrow injection angle configuration.

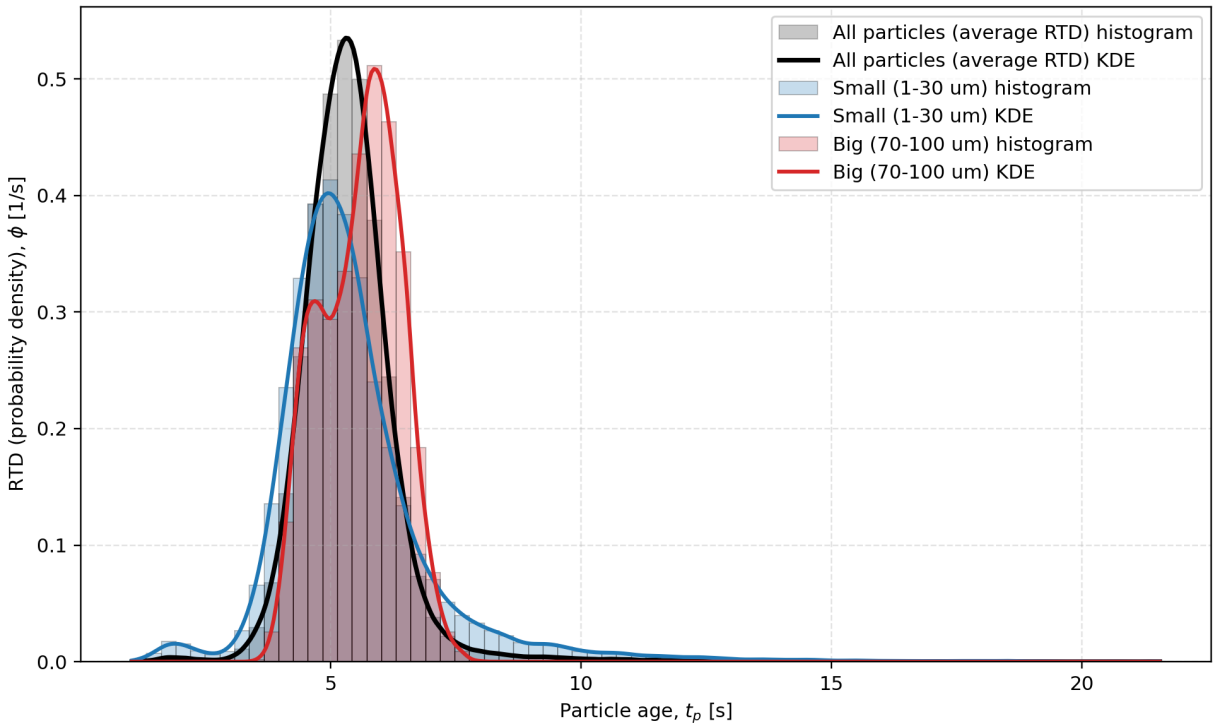


Figure 6.6: Size-segregated residence time distribution for the intermediate injection angle configuration.

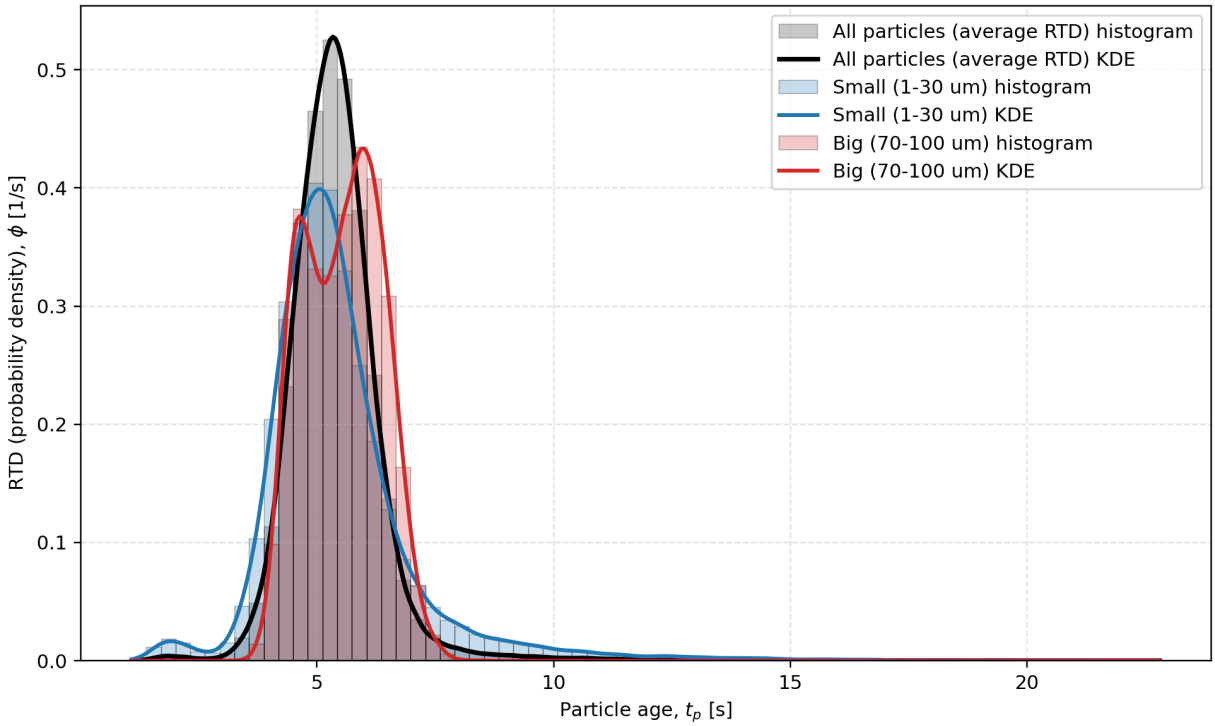


Figure 6.7: Size-segregated residence time distribution for the broad injection angle configuration.

dissipated without impacting the bulk swirling motion of the continuous gas. Meanwhile, the coarsest particles are governed by wall-friction and gravity following their initial impact with the walls, making them insensitive to variations in the initial injection trajectory.

Influence of Injection Velocity

Following the evaluation of the spray cone angle, the parametric study focused on the assessment of the influence of the initial particle injection velocity. Theoretically, a higher initial velocity increases the kinetic energy of the dispersed phase, potentially enhancing radial penetration into the Central Recirculation Zone and promoting a more uniform spatial dispersion. Conversely, excessive injection velocities risk driving the particles through the continuous phase streamlines directly into the chamber walls, thereby causing localized fouling and compromising long-term operational efficiency.

The numerical methodology was identical as previously described. Three distinct simulations were executed, varying the initial injection velocity across slow, intermediate, and fast regimes, while maintaining a constant mass flow rate, initial spray angle, and Particle Size Distribution. The resulting global RTD curves for these configurations are compared in Figure (6.8).

Consistent with the findings regarding the injection angle, the initial injection velocity has a negligible influence on the macroscopic, mass-averaged RTD curve. The overall distribution remains insensitive to the initial kinetic energy of the spray. However, an examination of the size-segregated RTD profiles reveals the same inertial segregation phenomena identified previously. The coarse particle fraction continues to exhibit a bimodal distribution, with the degree of bimodality amplifying at higher injection velocities, whereas the fine particle subpopulation remains completely unaffected.

This kinematic behavior can be explained by examining the momentum relaxation times of the respective size classes. Small droplets, characterized by low Stokes numbers, undergo rapid deceleration immediately upon injection. The free-stream aerodynamic drag swiftly dissipates their initial kinetic energy, forcing them to assume the velocity of the local continuous phase. Consequently, their transport remains heavily dominated by the bulk gas hydrodynamics, rendering their initial injection velocity irrelevant.

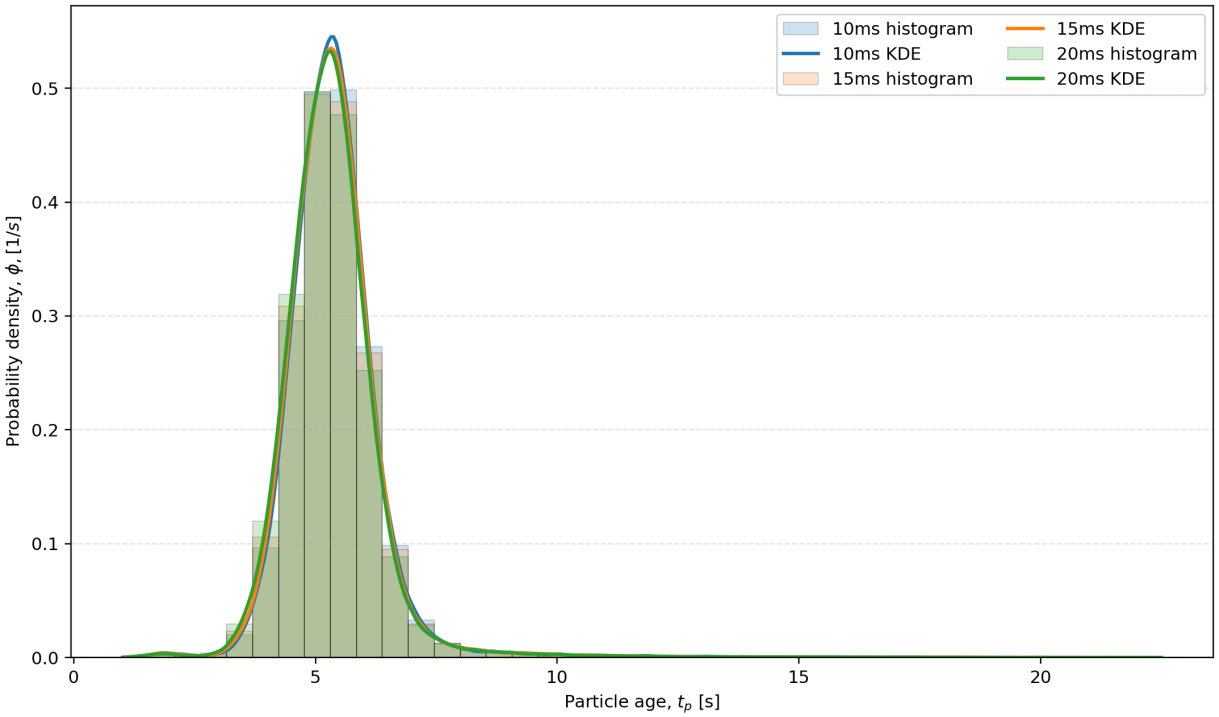


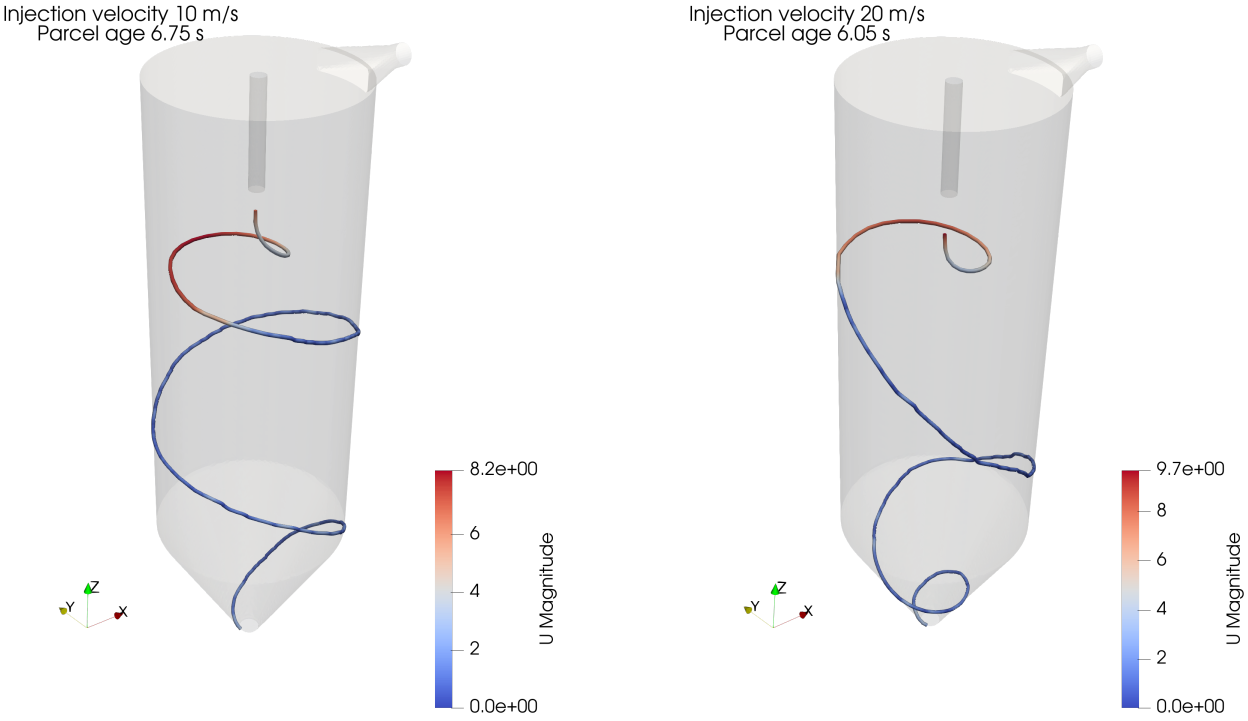
Figure 6.8: Comparison of global RTD curves across slow, intermediate and fast injection velocities.

Similarly, the extreme-coarse particles possess sufficient initial inertia to traverse the core of the pulsating vortex and impact the chamber walls rapidly, regardless of the starting velocity magnitude. As established before, upon inelastic collision, their transport mechanism transitions from free-stream entrainment to a near-wall boundary-layer transport regime. Their subsequent descent is governed by a balance of gravitational acceleration, wall friction, and near-wall tangential aerodynamic drag, effectively decoupling their total residence time from their initial injection conditions.

In contrast, the intermediate-sized particles (e.g., sub-100 μm) experience some degree of sensitivity to the injection velocity. For this specific inertial class, varying the initial velocity directly alters their radial penetration depth and subsequent Lagrangian trajectories, thereby modulating their average residence time. This phenomenon is illustrated by the representative particle pathlines in Figure (6.9).

As depicted in Figure (6.9), an intermediate particle injected at 20 m/s possesses enough momentum to impact the peripheral wall earlier in its trajectory, transitioning to the boundary-layer transport regime sooner. On the other hand, the equivalent particle injected at 10 m/s completes an entire additional revolution within the primary swirling flow before undergoing wall impingement. In this specific representative sample, the delayed wall impact extends the total residence time by 0.7 s compared to the high-velocity case. While individual discrete trajectories are subject to stochastic turbulent dispersion, the aggregated statistical effect of this altered penetration depth governs the shifting bimodality of the intermediate subpopulation's RTD.

Based on the combined analyses of injection angle and velocity, one might wrongly conclude that atomizer selection has a minimal impact on the macroscopic RTD. However, the most important operational parameter governed by the atomizer is not the initial kinematic state of the spray, but rather the generated Particle Size Distribution. Because discrete populations of varying diameters exhibit radically divergent transport mechanisms — ranging from aerodynamic entrainment to inertia-driven boundary sliding — the underlying PSD surely dictates the resulting global RTD. The specific hydrodynamic parameters of the injection (velocity and angle) are of secondary importance, as the initial kinetic energy of the dominant fine-particle fraction is quickly dissipated, yielding to the prevailing aerodynamic forces of the continuous swirling steam environment.



(a) Path traced by a sample particle of size $d = 84$ μm injected at 10 m/s.

(b) Path traced by a sample particle of size $d = 84$ μm injected at 20 m/s.

Figure 6.9: Comparison of particle paths injected at two different velocities.

Influence of Particle Size Distribution

To confirm the hypothesis that the atomizer-defined Particle Size Distribution is the primary determinant of macroscopic multiphase transport, an alternative PSD profile was formulated. This modified distribution maintained the statistical variance of the baseline population but featured a mean diameter intentionally shifted toward the coarser size fraction.

Two independent multiphase simulations were executed utilizing this modified PSD, applying initial injection velocities of 15 m/s (intermediate) and 20 m/s (fast). Consistent with the established numerical methodology, Lagrangian tracking data was extracted only after the two-way coupled flow field had achieved a quasi-steady state. The resulting global RTD curves for these configurations are presented in Figure (6.10).

As depicted in Figure (6.10), the morphological characteristics of the resulting RTD curves deviate significantly from those generated by the baseline particle population. The mean residence time is distinctly delayed. Furthermore, the statistical distribution has severe positive skewness, characterized by a pronounced right-hand tail extending up to the 20-second mark. Whereas the baseline RTD approximated a symmetric, normal distribution centered around the fine-droplet entrainment time, the coarse-shifted PSD generates a highly asymmetric profile heavily weighted toward longer residence times.

These results support the hypothesis established in the preceding analysis: the underlying PSD is the dominant operational parameter dictating the global RTD within the drying chamber. By shifting the bulk spray mass to the coarse fraction — which, as previously demonstrated, rapidly escapes the primary gas streamlines and transitions into a slower, friction-dominated boundary-layer transport regime — the overall mass-averaged residence time is extended.

The precise hydrodynamic parameters of the injection remain of secondary importance. This is evidenced by the near-perfect superimposition of the RTD curves for the 15 m/s and 20 m/s injection velocities. The alignment of these curves confirms that for coarse-dominated sprays, the initial droplet kinetic energy is quickly dissipated upon wall impact, rendering the extended boundary-layer descent entirely decoupled from the initial atomizer velocity.

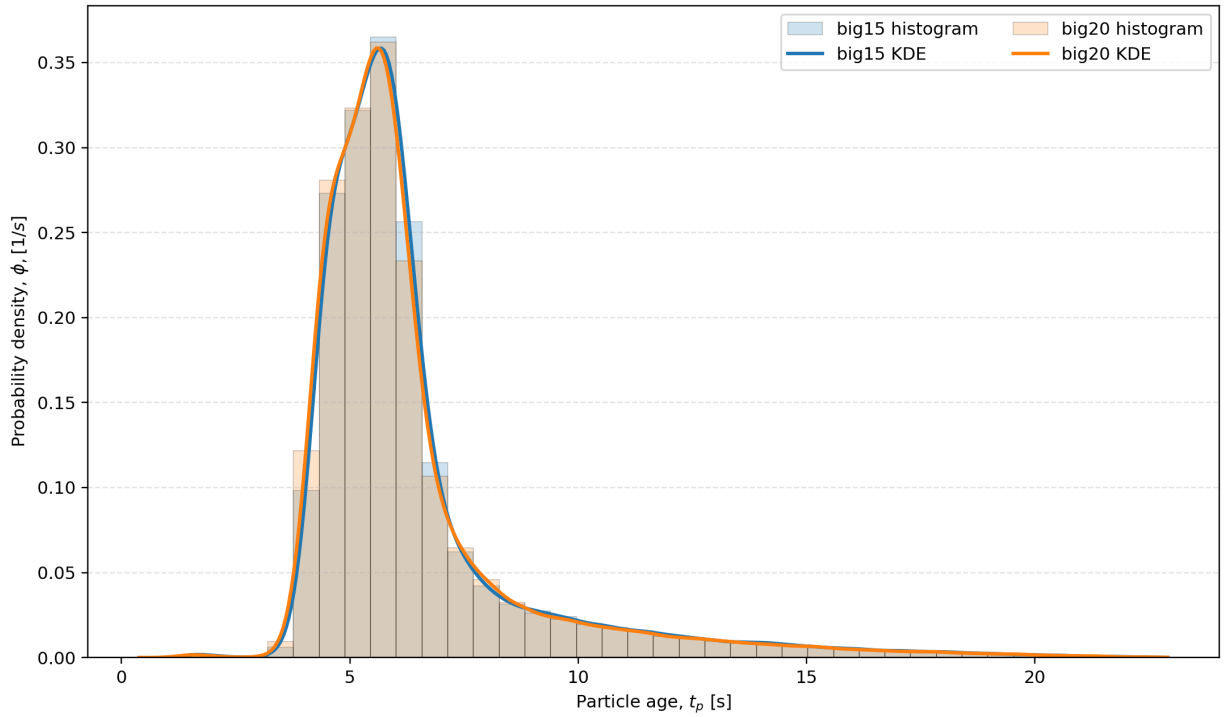


Figure 6.10: Comparison of global residence time distribution curves for the coarse-shifted particle population across intermediate and fast injection velocities.

Influence of Feedstock Mass Flow Rate

The final operational parameter evaluated in this parametric study was the mass flow rate of the liquid feedstock. Within the Eulerian-Lagrangian framework, the total mass of the dispersed phase dictates the magnitude of the interphase momentum source terms applied to the continuous phase. By reducing the liquid feedstock mass flow rate, the aerodynamic dampening exerted by the particles is minimized, allowing the bulk gas hydrodynamics to exert greater dominance over the resulting Residence Time Distribution.

Three independent multiphase simulations were executed, varying the feedstock mass flow rate across small, intermediate, and high regimes. The numerical methodology and stabilization protocols remained consistent with the preceding parametric evaluations. The resulting global RTD curves for these configurations are presented in Figure (6.11).

As depicted in Figure (6.11), the mass flow rate of the dispersed phase has a large influence on the macroscopic RTD. At higher flow rates, the global RTD is distinctly shifted toward shorter residence times and exhibits a reduced statistical variance. Conversely, lower mass flow rates produce an extensively broadened RTD profile characterized by a delayed mean residence time.

This divergence in kinematic behavior confirms that the cumulative mass of the dispersed phase significantly alters the macroscopic hydrodynamics of the drying chamber. Furthermore, it further validates the necessity of employing a fully two-way coupled interphase momentum framework when modeling this class of multiphase systems.

This phenomenon is driven by the axial momentum transfer between the phases. In the low mass flow rate configuration, the discrete phase introduces fewer momentum sources to accelerate the gas axially downward. Consequently, the high-swirl, tangential velocity component of the continuous phase remains dominant, increasing the prevalence of local turbulent eddies and radial dispersion. The interaction with these turbulent structures supports the stochastic dispersion of the particles, thus broadening the RTD variance.

At the other hand, at higher mass flow rates, the continuous phase is aerodynamically dragged by

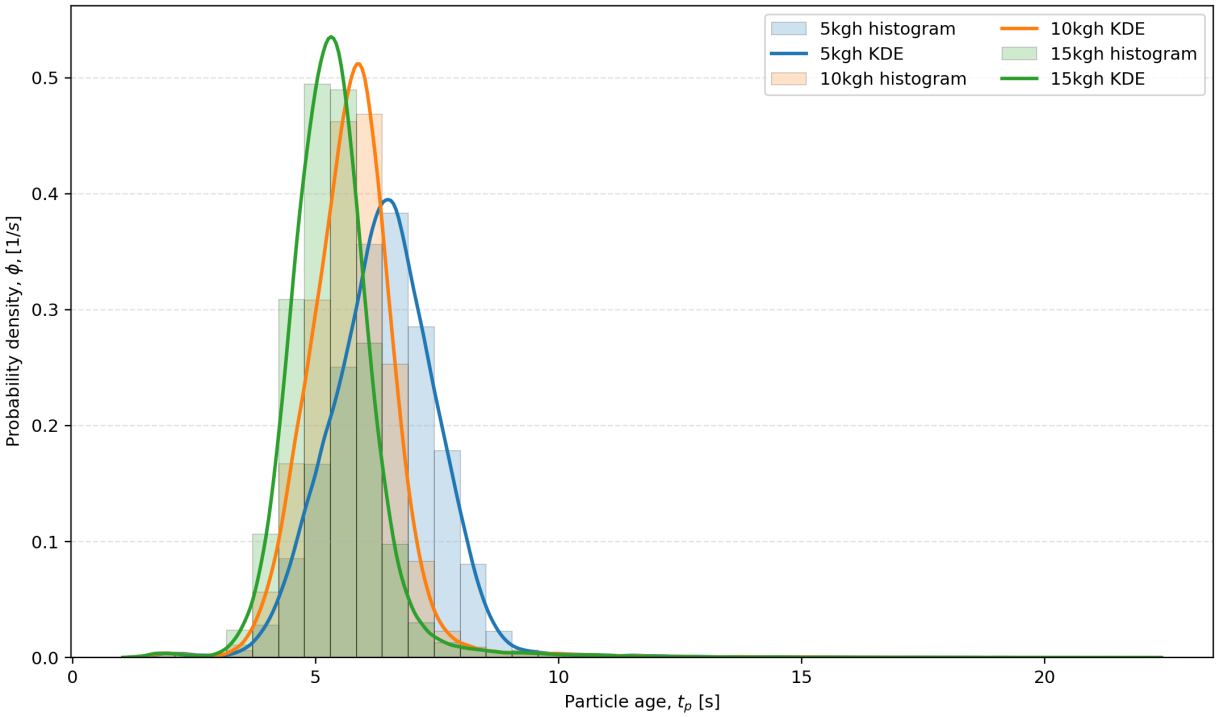


Figure 6.11: Comparison of global residence time distribution curves across varying mass flow rates of the liquid feedstock.

the substantial downward momentum of the injected particulate phase. This enhances the axial velocity component, to some extent suppressing the swirling structures and accelerating the combined multiphase mixture toward the exhaust, yielding a sharper, shorter RTD.

From a process engineering perspective, this finding holds practical value. It demonstrates that operators can actively tune the mean residence time — and, by extension, the corresponding thermal exposure of the product — by regulating the feedstock mass flow rate, without necessitating structural modifications to the atomization hardware or chamber geometry.

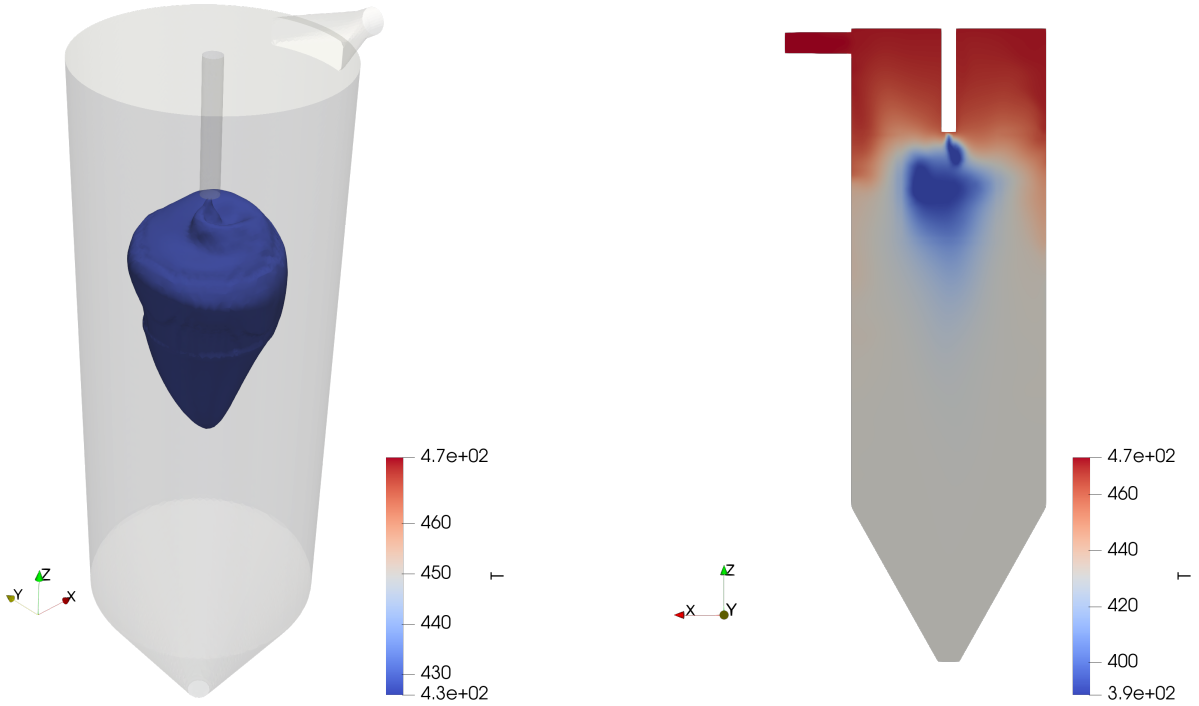
6.2 Coupled Heat and Mass Transfer Simulation

Following the hydrodynamic verification of the discrete phase, the numerical framework was extended to incorporate fully coupled interphase heat and mass transfer models. This section evaluates the thermodynamic impact of particle evaporation on the continuous steam phase, analyzes the spatial deposition patterns along the chamber walls, and concludes with an assessment of the product's final moisture content and the Residence Time Distribution.

6.2.1 Effect on the Continuous Phase

The primary consequence of activating the phase-change models is a measurable temperature drop within the continuous steam phase. The magnitude of this temperature gradient is governed by the initial subcooling of the injected feedstock, the latent heat of vaporization, and the specified critical moisture parameter. The spatial influence of solvent evaporation on the continuous phase temperature field — simulated with an initial droplet temperature of 370 K and a critical moisture fraction of 0.5 — is presented in Figure (6.12).

Figure (6.12) illustrates a distinct thermal drop downstream of the atomization nozzle. This localized zone corresponds to the primary injection region, where the superheated steam transfers a substantial portion of its sensible heat to the dispersed phase to drive vaporization. The spatial morphology of this cooling zone



(a) Temperature isosurface of the continuous phase.

(b) Cross-sectional temperature contour.

Figure 6.12: Effect of coupled droplet evaporation on the macroscopic continuous phase temperature field.

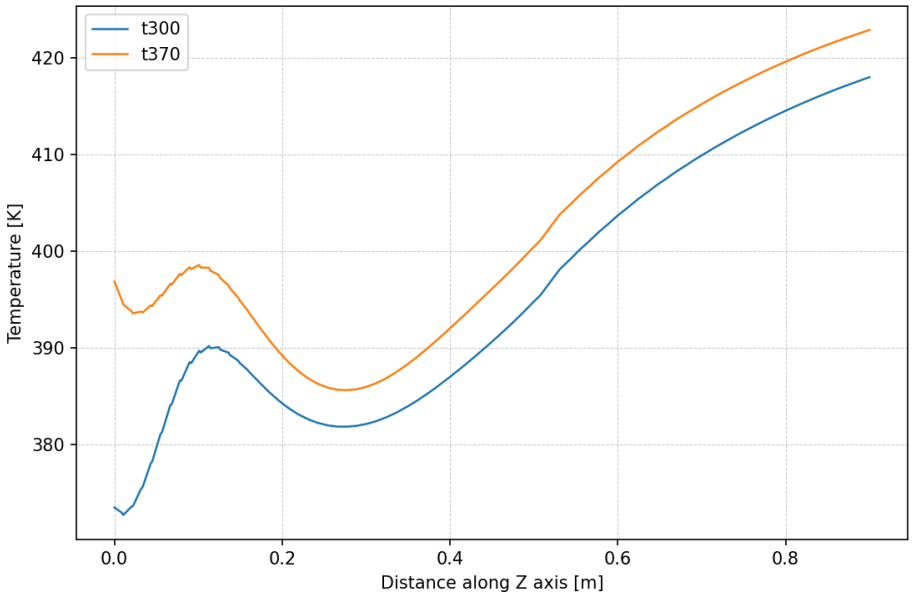
is a concentrated, oval structure along the central axis. This lower temperature region does not extend radially to the chamber walls. This implies that intense evaporation is mostly constrained to the central core. As a result, particles traveling radially toward the peripheral walls are likely to have already surpassed the critical moisture threshold, initiating solid crust formation and mitigating the risk of wet-particle wall fouling upon impact.

Asides from the primary injection zone, a macroscopic thermal gradient is established across the drying chamber. The superheated steam enters the upper domain, maintaining its initial inlet temperature of approximately 473 K until it encounters the atomization plume. At this axial cutoff point, the bulk steam temperature undergoes a decline up to approximately 430 K. The lower regions of the geometry exhibit an uniform thermal profile, indicating thorough convective mixing between the cooled central gas and the hotter peripheral flow. The uniformity of the temperature field below this primary vaporization zone suggests that negligible latent heat transfer occurs in the lower portion of the spray dryer, marking the completion of the active drying kinetics.

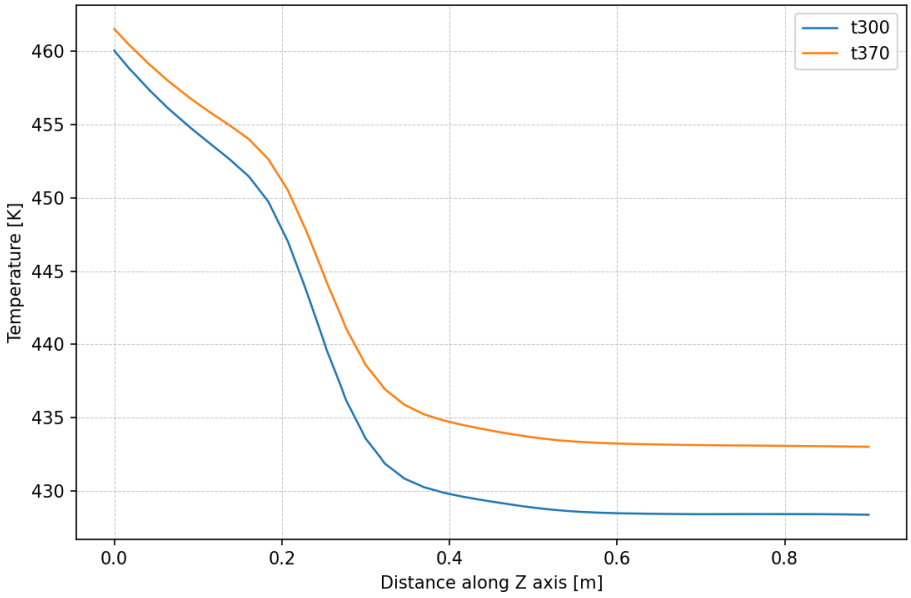
This spatial thermodynamic behavior is further quantified by the axial temperature profiles presented in Figure (6.13).

Along the central geometric axis (Figure 6.13a), the steam temperature experiences a sudden drop below the nozzle before stabilizing at the bulk average temperature. The profile extracted closer to the chamber wall (Figure 6.13b) demonstrates a steep thermal gradient corresponding to the radial expansion of the vaporization zone, after which it asymptotically approaches the bulk steam temperature. A comparative analysis of temperature profiles confirms that reducing the initial temperature of the liquid feedstock lowers the final equilibrium temperature of the continuous phase. This is physically consistent, as additional sensible heat must be extracted from the steam to raise the subcooled droplets to their saturation temperature prior to the onset of boiling.

Finally, an evaluation of the continuous phase velocity contours and pressure isosurfaces confirms that the macroscopic aerodynamics remain largely unchanged by the thermodynamic coupling; the domain is still characterized by a swirl-dominated, quasi-stable Central Recirculation Zone stabilized by the dispersed



(a) Temperature profile along the central Z-axis, originating immediately below the nozzle.



(b) Temperature profile along a vertical axis offset toward the chamber wall.

Figure 6.13: Continuous phase (steam) temperature profiles evaluated at two different injection temperatures.

phase. However, because the phase-change kinetics induce transient particle shrinkage and subsequent density variations within the rigid crust, the Lagrangian momentum balances of the dispersed phase are altered. These dynamic morphological changes will modify the droplet trajectories, a phenomenon that is expected to exert a measurable impact on the final Residence Time Distributions analyzed in the subsequent subsections.

6.2.2 Particle Kinematics and Spatial Deposition Patterns

As discussed in the preceding section, the continuous phase experiences significant macroscopic temperature gradients. This thermal variance induces localized fluctuations in the thermodynamic and transport properties of steam - such as dynamic viscosity and density - thereby it is a highly transient environment for the dispersed phase. At the same time, the discrete particles undergo rapid morphological changes; as the solvent evaporates, both the particle diameter and the effective bulk density decrease non-linearly.

This evaporative mass loss alters the balance of forces acting upon the discrete elements. As a droplet loses mass, its inertial response time decreases, leading to a corresponding reduction in its Stokes number. These evaporating particles experience lowered centrifugal forces adhere closer to the continuous phase streamlines. This effect of the shifting continuous phase properties and the transient particle morphology modifies the Lagrangian trajectories and spatial deposition patterns, as illustrated in Figure (6.14).

An analysis of these trajectories reveals kinematic behaviors that differ from the pure hydrodynamic tracking previously presented in Figure (6.2). In the thermally coupled simulations, the finer droplets remain entrained within the Central Recirculation Zone for extended durations. For instance, the particle with an initial diameter of 27 µm executes multiple orbital revolutions not only around the injection lance but also within the lower conical hopper. Similarly, the 42 µm particle demonstrates complex orbital kinematics; although it occasionally impinges upon the peripheral wall, it is far more frequently suspended within the central vortex than its non-evaporating counterpart.

For the coarser fraction (initial diameters of 79 µm and 118 µm), the trajectories remain relatively direct. Despite undergoing evaporation, their initial mass is sufficient to overcome radial aerodynamic drag, allowing centrifugal forces to propel them toward the lower chamber walls. Nevertheless, due to progressive mass depletion during their descent, even these massive droplets complete more orbital revolutions than inert particles of equivalent initial dimensions. This overall reduction in particle inertia suggests that wall collisions should be less frequent and that the global residence time distribution will shift toward longer durations.

In order to asses the risk of wall fouling, a deterministic adhesion criterion was applied: wall deposition is assumed to occur only if a particle impacts the boundary prior to the formation of its solid crust. Particles that have surpassed the critical moisture threshold and developed a rigid outer matrix are assumed to undergo inelastic rebound without adhering. Crust formation is sensitive to the specified critical moisture parameter, hence the collision mapping was evaluated under two distinct thresholds: $X_{cr} = 30\%$ and $X_{cr} = 50\%$. The resulting spatial collision density is presented in Figure (6.15).

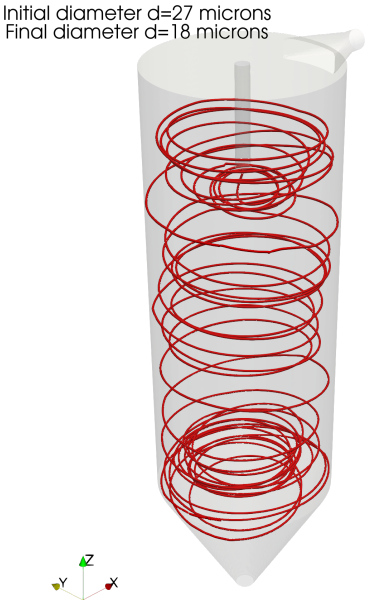
As observed in Figure (6.15), the macroscopic collision pattern in the coupled simulation retains the characteristic helical particle roping identified in the purely hydrodynamic case. However, the distinct high-density collision transition between the cylindrical body and the conical outlet is substantially dampened, and the severe localized hotspot near the 0.0 m elevation mark is eliminated. These morphological shifts in the collision map agree with the trajectory analysis: the continuous reduction in particle inertia mitigates intensive centrifugal wall-impingement, allowing a larger fraction of the dispersed phase to remain aerodynamically suspended in the bulk flow.

In order to quantify the fouling potential, a post-processing filter was applied to the collision data to isolate impingement events involving particles that had not yet reached the critical moisture threshold. Remarkably, zero such collisions were detected under both evaluated X_{cr} criteria. The evaporation kinetics within the primary injection zone are sufficiently rapid that all droplets undergo crust formation well before their radial trajectories intersect with the chamber walls. This conclusion is consistent with the Eulerian thermal fields detailed in the previous section, which demonstrated that the latent heat sink is heavily concentrated immediately below the nozzle and does not propagate to the 430 K peripheral boundaries.

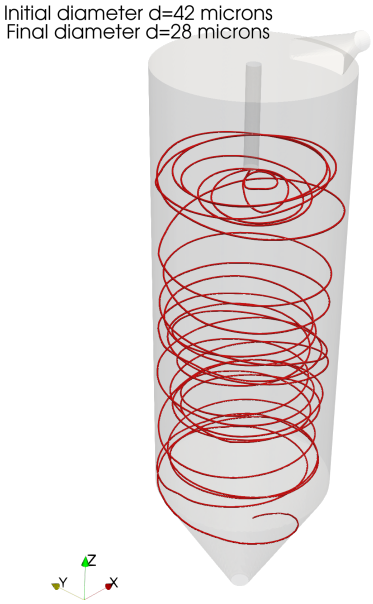
Despite the highly rotational hydrodynamics driving the dispersed phase toward the chamber walls, the large thermal gradients of the superheated steam environment ensure rapid surface drying, thereby theoretically eliminating the risk of wet-particle wall fouling.

6.2.3 Residence Time Distribution and Product Properties Analysis

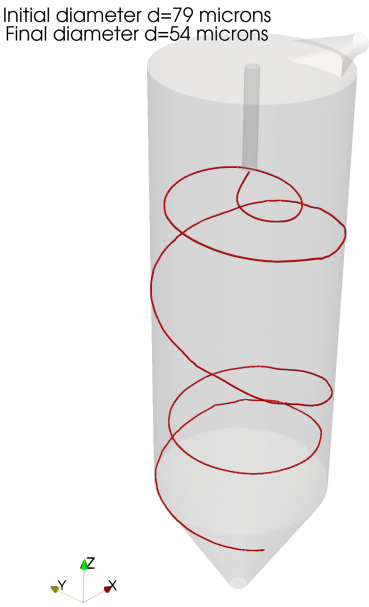
Preliminary kinematic analysis suggests that the implementation of fully coupled phase-change thermodynamics affects the Particle Residence Time Distribution as compared to the uncoupled



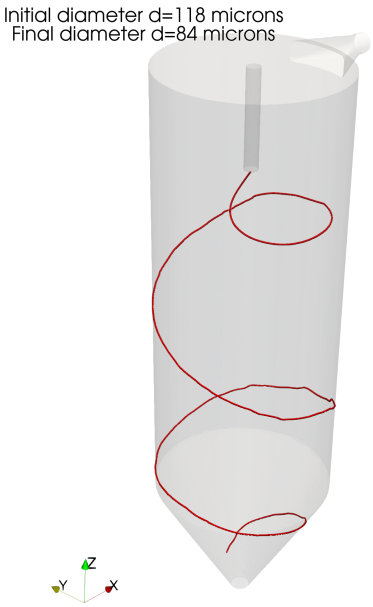
(a) Path traced by a sample particle of initial size $d = 27\ \mu$m



(b) Path traced by a sample particle of initial size $d = 42\ \mu$m



(c) Path traced by a sample particle of initial size $d = 79\ \mu$m



(d) Path traced by a sample particle of initial size $d = 118\ \mu$m

Figure 6.14: Lagrangian trajectories of individual discrete particles as a function of initial diameter within the coupled heat and mass transfer environment.

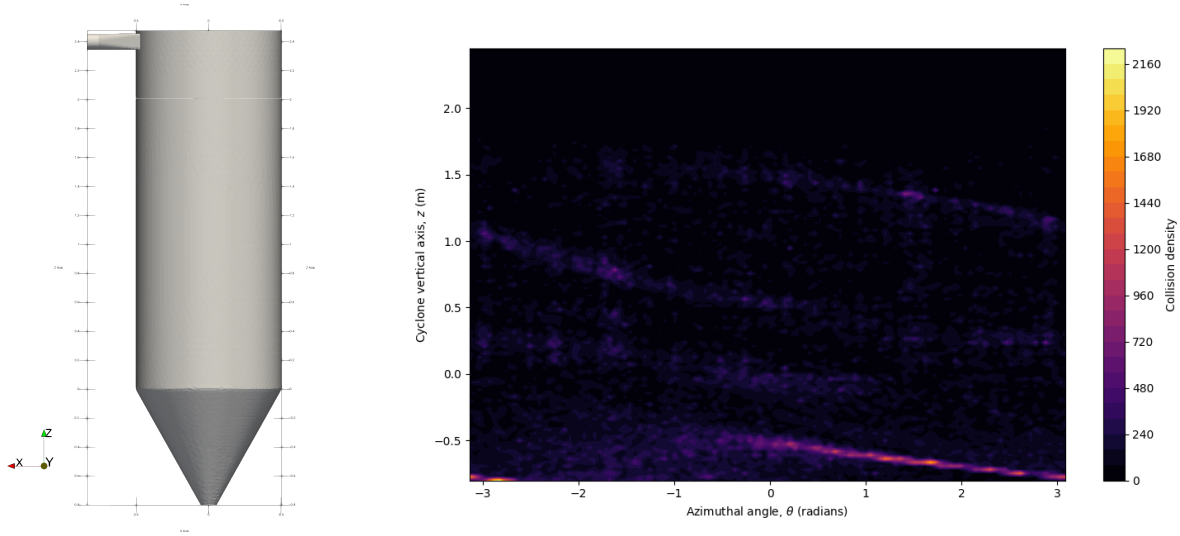


Figure 6.15: Overall spatial collision density heatmap for a critical moisture parameter of 50%.

hydrodynamic models. This section evaluates the sensitivity of the RTD and the resultant product morphology to variations in critical drying parameters.

Influence of the Critical Moisture Parameter

As described in the theoretical framework, the critical moisture content (X_{cr}) is an important parameter determining the final residual moisture of the dried powder. This threshold marks the transition from constant-rate evaporation to the falling-rate drying period, triggering the precipitation of a solid crust around the receding wet core, as previously illustrated in Figure (2.1). Because X_{cr} is highly material-specific and must typically be derived empirically, a parametric sensitivity study was executed to quantify its influence on the macroscopic simulation results.

Three independent multiphase simulations were conducted, isolating X_{cr} as the only independent variable, evaluated at thresholds of 0.3, 0.5, and 0.7 (wet basis). Following the standard methodology, the Lagrangian data was extracted and analyzed. The superimposed global RTD curves for these varying X_{cr} cases are presented in Figure (6.16).

As depicted in Figure (6.16), the global RTD profiles across the three discrete X_{cr} evaluations overlap almost perfectly. This invariance is advantageous from a computational modeling perspective; it demonstrates that the bulk residence time of the dispersed phase is statistically independent of a thermodynamic boundary condition that carries empirical uncertainty. The macroscopic aerodynamic transport can be analyzed with high confidence irrespective of the precise X_{cr} value.

However, when compared to the purely hydrodynamic baselines, the thermally coupled RTD experiences a pronounced shift toward extended residence times. Furthermore, the distribution variance is increased, indicating a broader statistical spread in the Lagrangian transport times. Unlike the symmetric, quasi-normal profiles observed in the uncoupled cases, the thermally coupled RTD possesses a positive skew, characterized by an extended right-hand tail. Additionally, the localized peak corresponding to initial short-circuiting is enlarged, suggesting that a larger fraction of particles prematurely bypasses the primary recirculation zones.

To illustrate the mechanics driving this statistical spread, the global RTD was decomposed into size-specific subpopulations, as illustrated in Figure (6.17).

Figure (6.17) shows that the fine-fraction population (characterized by final diameters between 1 and 15 m) is subject to pronounced kinematic variability. While the mode of this subpopulation's RTD is centered near 2.5 seconds, the distribution has a visible tail extending beyond the 20-second threshold. These droplets are susceptible to early domain exit, yet simultaneously possess the potential for significant entrapment durations. This bimodal behavior is governed by their minimal Stokes numbers; fine particles exhibit high fidelity to the continuous phase streamlines and are easily entrained by turbulent eddies, frequently becoming

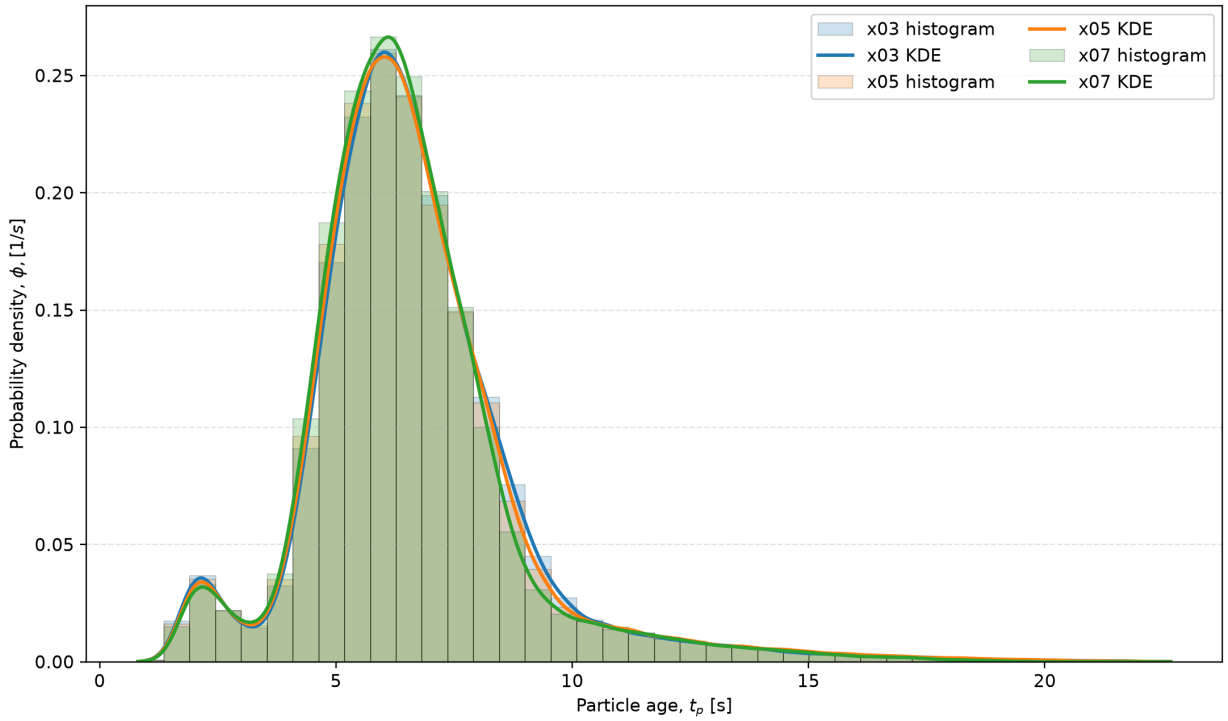


Figure 6.16: Comparison of the global mass-averaged Residence Time Distribution across varying critical moisture parameter thresholds.

trapped within the Central Recirculation Zone for extended orbital periods.

At the other hand, the coarse particle fraction (final diameters between 20 and 50 μm) have much smaller statistical variance. Almost no particles within this specific subpopulation exit prior to 3 seconds or persist beyond 10 seconds. Retaining a higher effective inertia, these particles decouple from the high-frequency turbulent eddies and the primary gas swirl, facilitating a more direct, gravity-assisted descent toward the discharge outlet.

Given the large variance introduced by the fine-droplet entrainment, it is hypothesized that the final Particle Size Distribution of the dried product is heavily skewed toward the lower size fractions. This hypothesis is verified by comparing the initial injection PSD against the final product PSD, as presented in Figure (6.18).

Figure (6.18) illustrates a shift in the volumetric PSD resulting from the evaporative kinetics. The final numerical distribution is narrower and shifted toward the fine spectrum, having a primary peak near the 15 μm mark, with a negligible volumetric fraction exceeding 70 μm. This final PSD is consistent with the size-segregated RTD (Figure 6.17). As droplets vaporize, the simultaneous reduction in physical diameter and bulk density makes them susceptible to turbulent dispersion.

While Figure (6.16) demonstrated that varying X_{cr} yields identical macroscopic RTD profiles, its thermodynamic impact on the final morphological properties is significant. The resulting product PSDs for the evaluated critical moisture thresholds are compared in Figure (6.19).

Figure (6.19) demonstrates a direct proportionality between X_{cr} and the final particle diameter. An increase in the critical moisture threshold accelerates the temporal onset of solid crust formation. Because macroscopic geometric shrinkage is physically halted once the rigid crust precipitates, earlier crust formation preserves a larger final particle volume.

This preservation of larger diameters suggests a marginal reduction in the kinematic variance of the RTD. A re-examination of Figure (6.16) confirms this subtle effect; the distribution curve corresponding to $X_{cr} = 70\%$ is slightly narrower and has a marginally elevated peak. However, these kinematic deviations are minor.

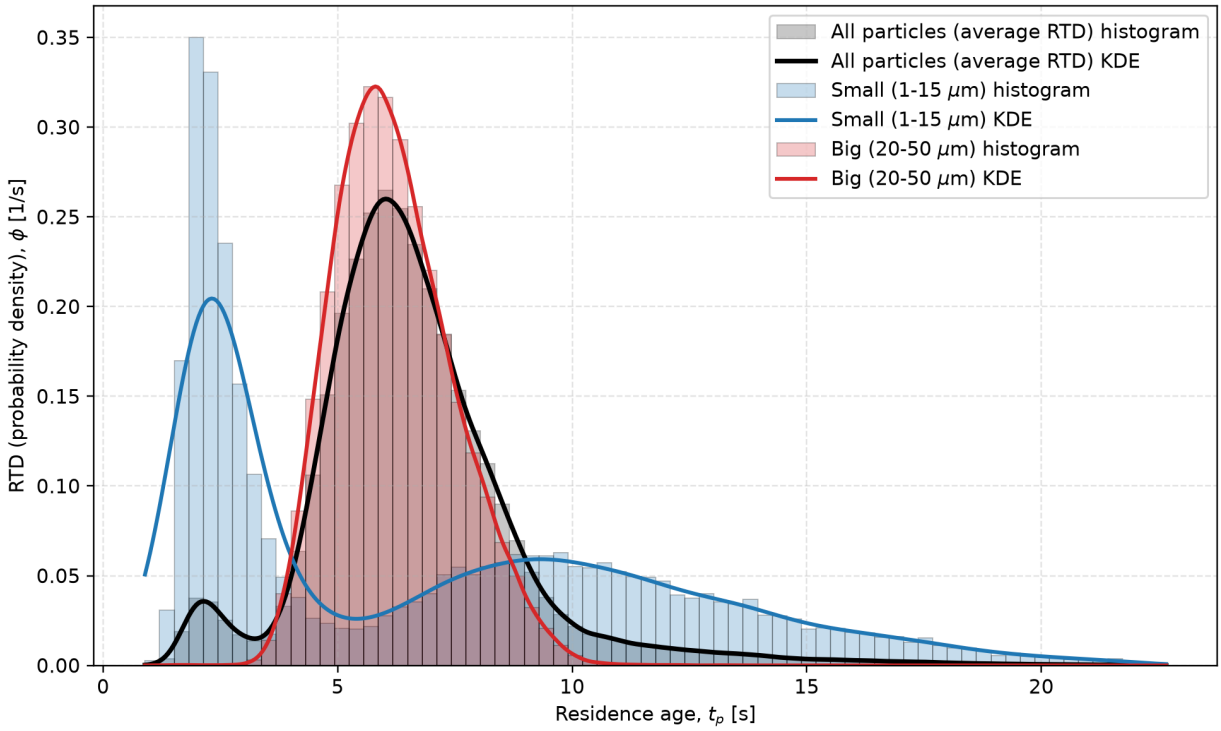


Figure 6.17: Residence Time Distribution segregated by final particle diameter classifications (fine vs. coarse fractions).

Furthermore, the preservation of larger geometric volumes due to early crust formation directly correlates with elevated residual moisture within the final product, as a larger volume of unbound solvent is trapped within the developing porous matrix. This is confirmed by the final moisture content distributions depicted in Figure (6.20).

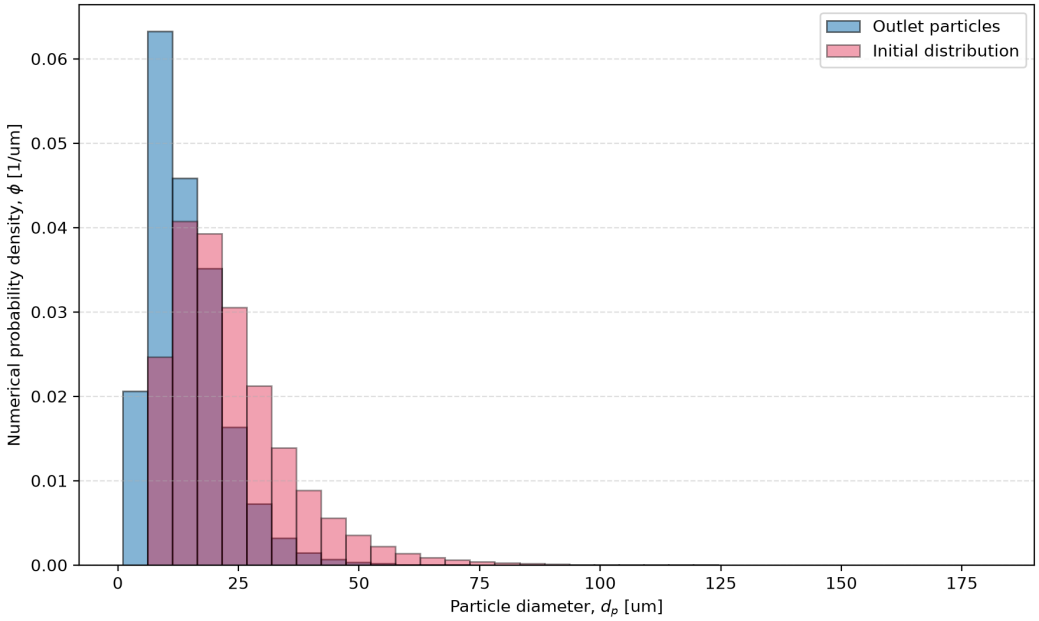
Figure (6.20) clearly indicates that increasing X_{cr} yields both a higher mean residual moisture and a broader statistical distribution of moisture across the product population.

The physical mechanism driving this result is tied to the internal heat and mass transfer balances during the falling-rate drying period. A higher X_{cr} induces premature crust precipitation, establishing a severe internal mass transfer resistance. Subsequently, the convective heat flux supplied by the superheated steam is no longer entirely consumed as latent heat of vaporization; instead, a substantial fraction is partitioned into the sensible heating of the solid matrix. As the particle surface temperature elevates toward the continuous phase temperature, the thermal driving gradient (ΔT) diminishes, decreasing the vaporization rate. Ultimately, thermal equilibrium is achieved between the particle and the superheated steam, ceasing all evaporative mass transfer and permanently locking the residual solvent within the solidified structure.

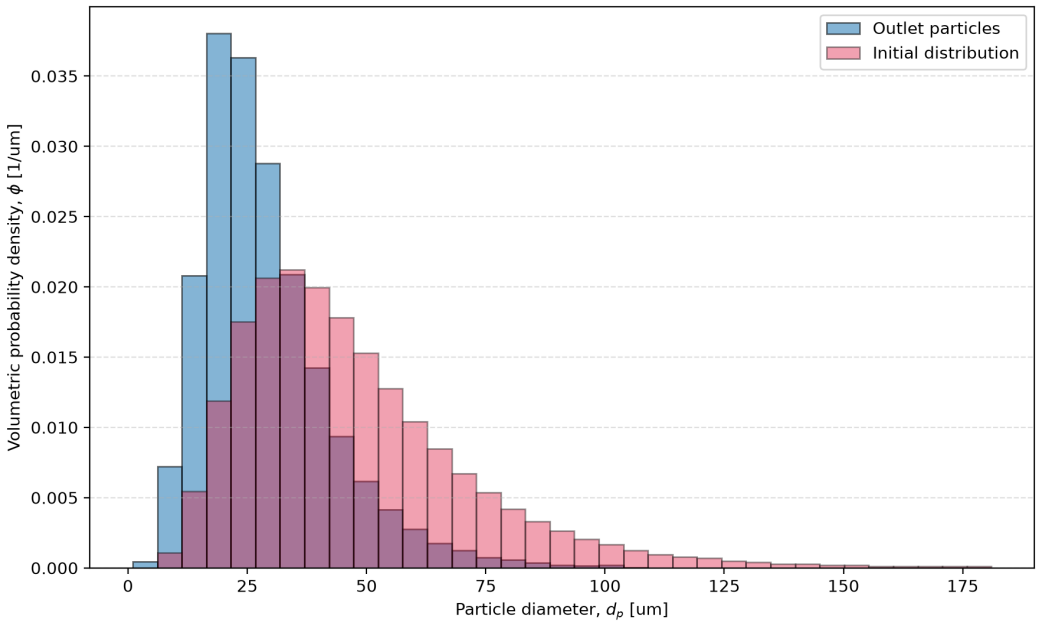
From a mathematical modeling and validation perspective, X_{cr} serves as a calibration scalar. By comparing numerical predictions of the final PSD or bulk residual moisture against empirical pilot-plant data, X_{cr} can be iteratively tuned to accurately close the heat and mass transfer balances. Within this established Eulerian-Lagrangian framework, X_{cr} remains the primary empirical fitting parameter, while all other interphase transport phenomena are rigorously resolved via thermodynamic and aerodynamic principles.

Influence of the Initial Droplet Temperature

In addition to the critical moisture parameter, the precise inlet temperature of the dispersed liquid droplets is a significant source of empirical uncertainty. In industrial configurations, the liquid feedstock is frequently subjected to preheating prior to injection. Furthermore, the thermal environment in the atomizer



(a) Comparison of the numerical Particle Size Distribution at the injection inlet versus the exhaust outlet.



(b) Comparison of the volumetric Particle Size Distribution at the injection inlet versus the exhaust outlet.

Figure 6.18: Comparison between initial and final PSD.

complicates the accurate determination of the initial droplet temperature precisely at the injection nozzle.

Given these operational complexities, estimating the exact injection temperature introduces a degree of uncertainty into the numerical model. In order to quantify the sensitivity of the macroscopic transport phenomena and final product properties to this parameter, two independent simulations were executed

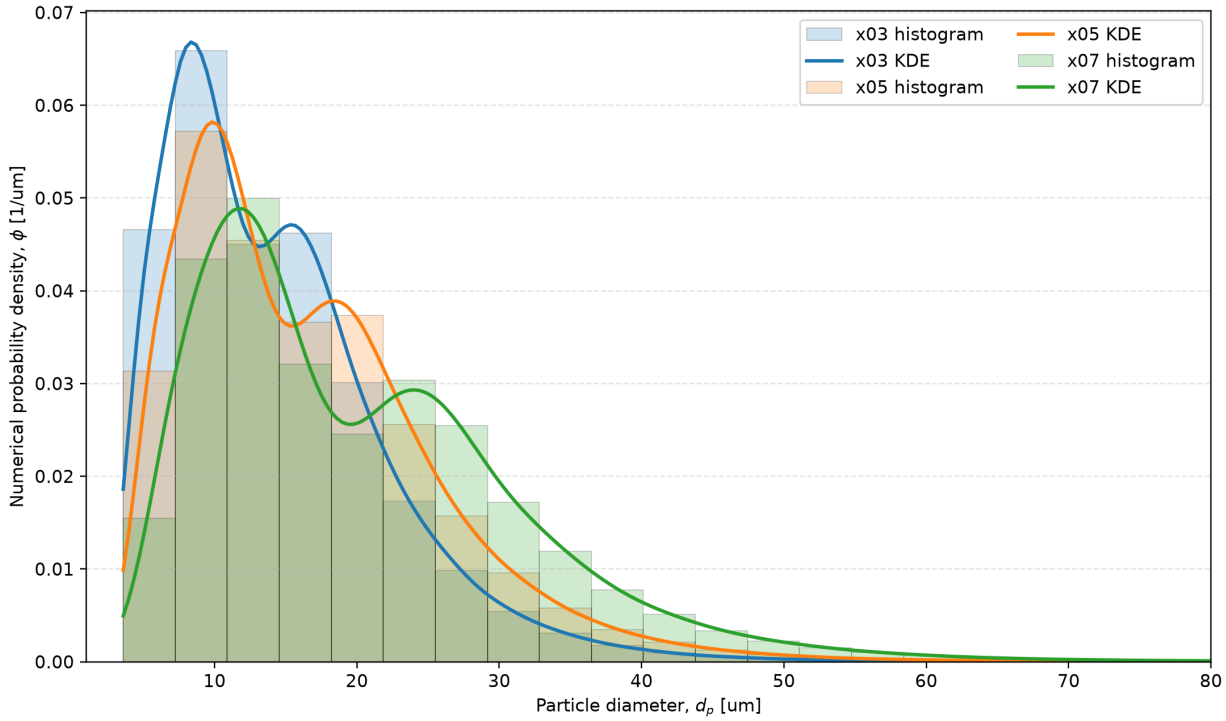


Figure 6.19: Comparison of the final product numerical Particle Size Distributions across varying critical moisture parameter thresholds.

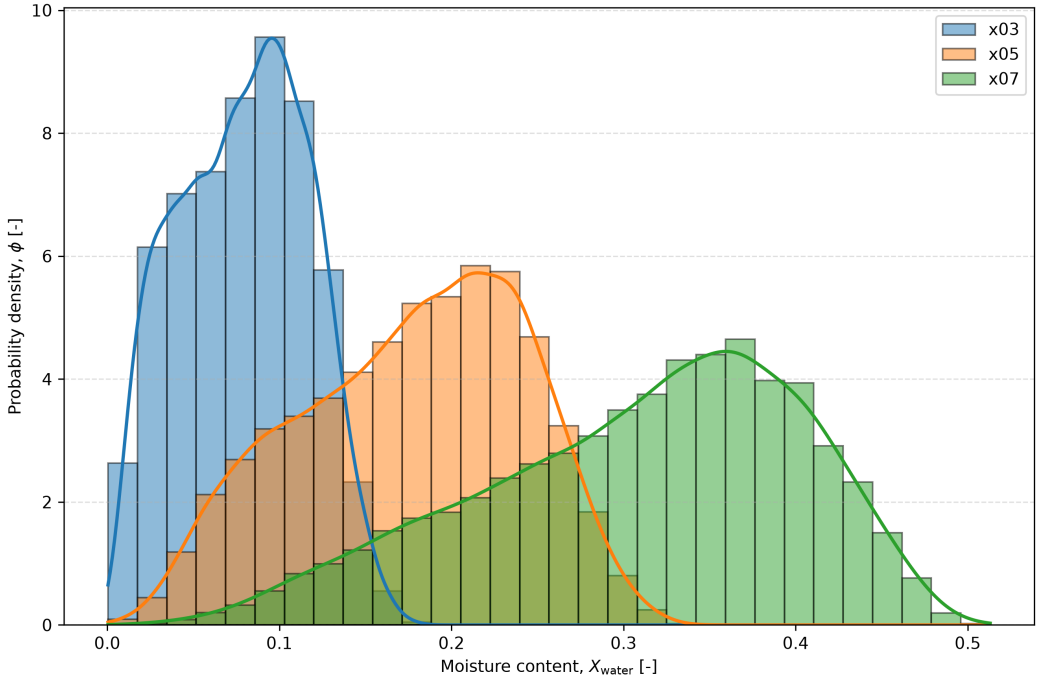


Figure 6.20: Comparison of the final residual moisture content distributions across varying critical moisture parameter thresholds.

utilizing distinct initial droplet temperatures. Following the established quasi-steady stabilization protocol, the resulting global Residence Time Distributions were extracted and are compared in Figure (6.21).

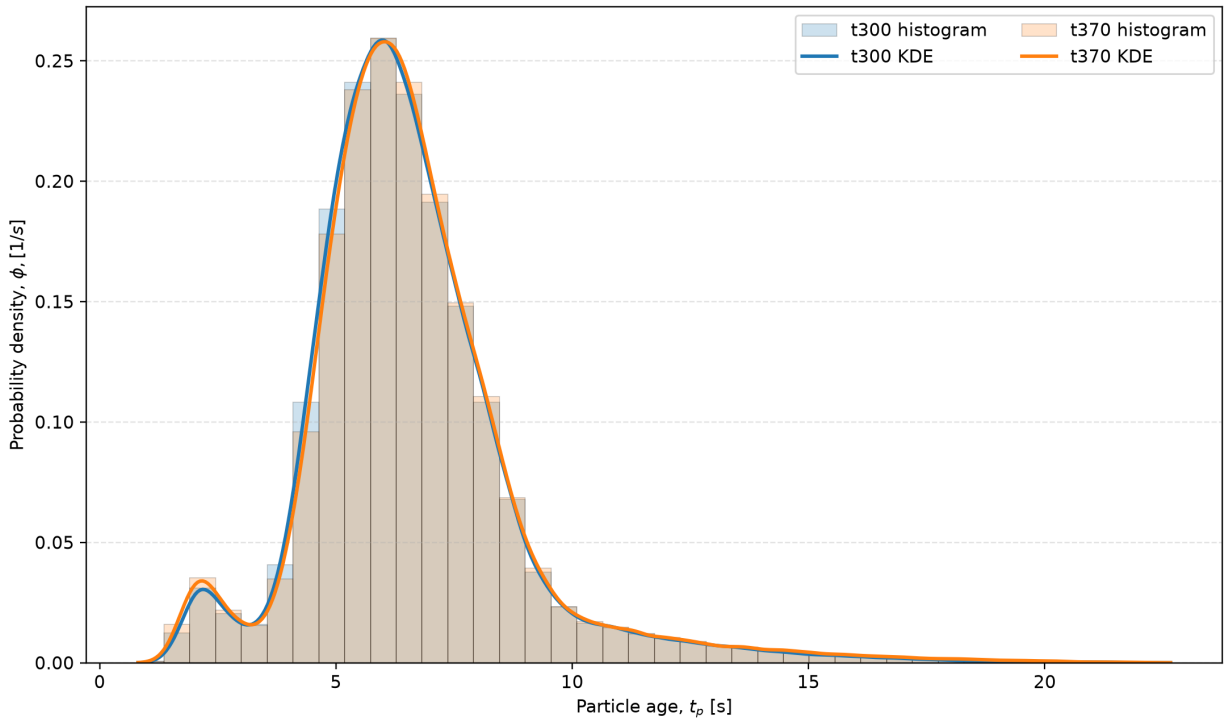


Figure 6.21: Comparison of the residence time distribution across cases with different initial droplet temperature.

The superimposed RTD profiles in Figure (6.21) show near-perfect alignment. This temporal invariance demonstrates that the initial thermal state of the droplets does not significantly affect the overall kinematics or aerodynamic transport of the dispersed phase. Based on this kinematic consistency, it follows that the final residual moisture distributions should display a similar degree of insensitivity. This hypothesis is evaluated in Figure (6.22).

As anticipated, the residual moisture distributions for the evaluated temperatures demonstrate good alignment. A marginal shift toward higher residual moisture is observable in the lower initial temperature case; however, this deviation is negligible. The sensitivity of the final product properties to the initial injection temperature is an order of magnitude lower than its sensitivity to the critical moisture parameter.

Despite the minimal impact on particle kinematics and final moisture content, reducing the initial droplet temperature increases the sensible heat demand required to elevate the droplets to their saturation temperature. This elevated thermal demand extracts additional enthalpy from the continuous phase, thereby increasing the overall temperature drop. As previously detailed in Figure (6.13), the axial temperature profiles confirm that a lower initial droplet temperature induces a corresponding reduction in the bulk steady-state gas temperature.

In summary, the macroscopic multiphase flow and final product characteristics demonstrate insensitivity to the initial droplet temperature within the evaluated operating window. However, the evaluation of this thermal parameter exposes a significant limitation associated with the simplified phase-change model. As outlined in the preliminary assumptions, the custom numerical framework acts strictly as a one-way vaporization model; the source terms governing interphase mass transfer do not account for the inverse kinetics of steam condensation. Consequently, thermal energy is exchanged strictly via sensible heat fluxes and droplet vaporization.

If the initial droplet subcooling is excessively large, the localized enthalpy extraction required for sensible heating could theoretically drive the surrounding steam temperature below the saturation dome. In a

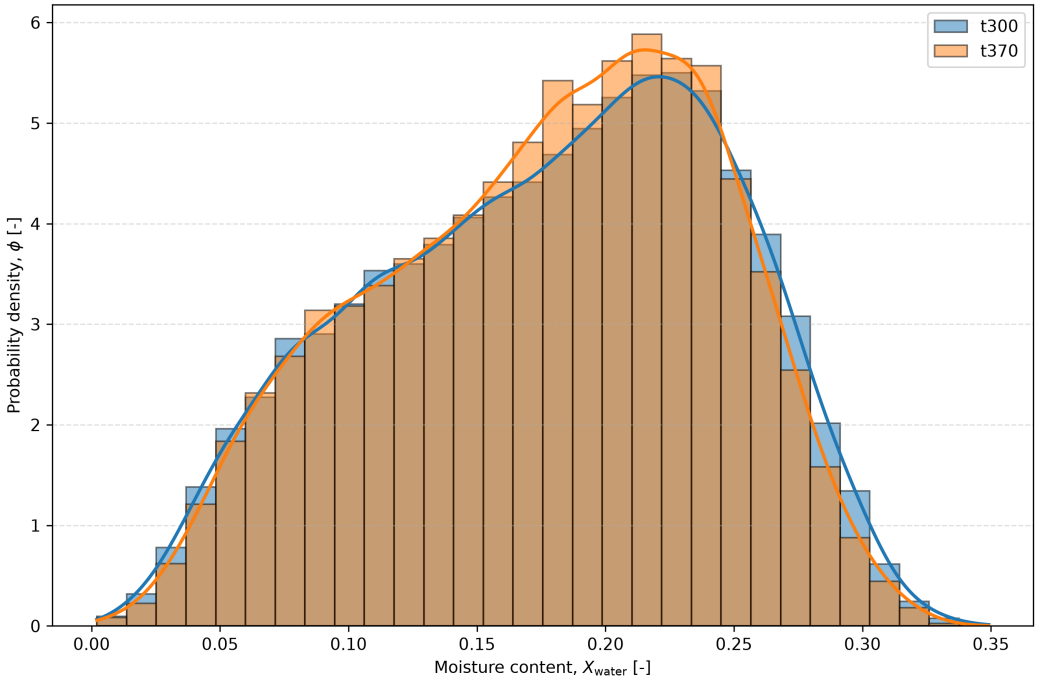


Figure 6.22: Comparison of the final residual moisture content distributions across varying initial droplet temperatures.

physical system, such localized subcooling would trigger spontaneous condensation, releasing significant latent heat back into the domain. Because this mechanism is intentionally disabled to preserve solver stability, sub-saturation conditions will manifest as localized, non-physical thermal depressions within individual computational cells.

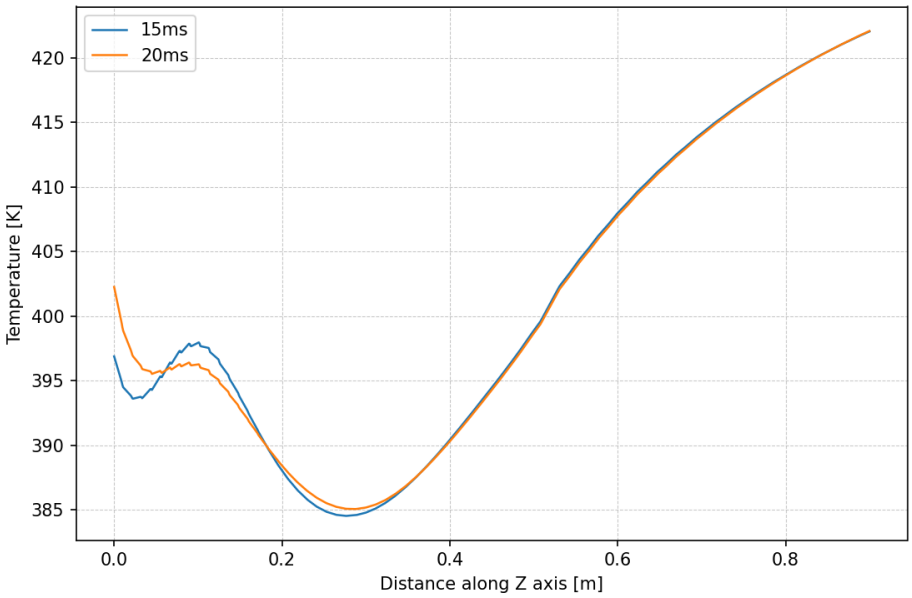
To circumvent this numerical artifact, the initial droplet temperature boundary condition should be specified sufficiently high to ensure the continuous phase remains superheated throughout the domain. Nonetheless, computational testing indicates that even if isolated cells transiently violate the saturation threshold, the core thermodynamic library maintains numerical stability, and the macroscopic, bulk-averaged results remain largely unchanged. Future implementations utilizing more complex, real-gas thermodynamic libraries would require either rigorous sub-saturation clipping or the integration of a full condensation sub-model to prevent solver divergence under extreme subcooled injection conditions.

Influence of the Droplet Injection Angle and Velocity

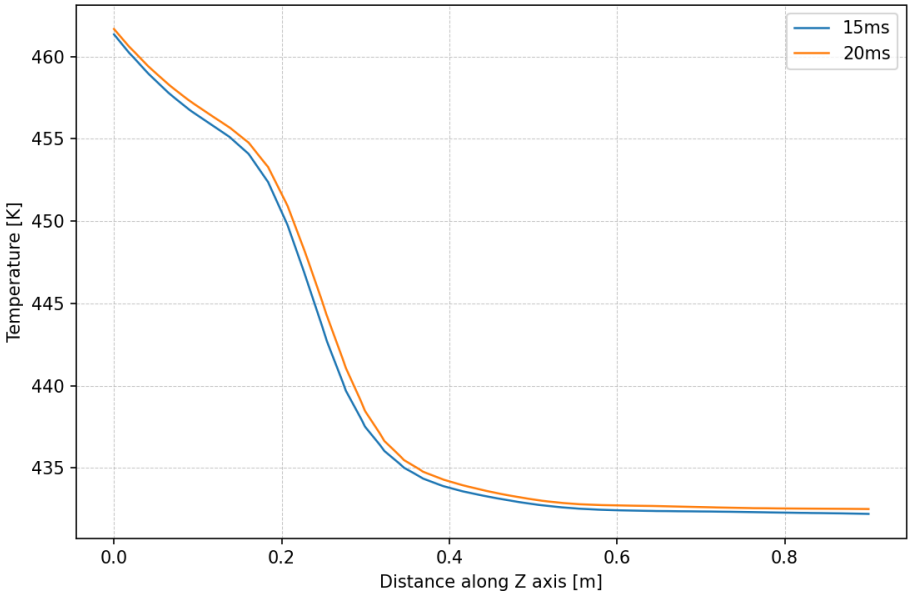
The preceding purely hydrodynamic analysis established that the initial injection kinematics — specifically, the spray cone angle and droplet velocity — have a negligible influence on the macroscopic Residence Time Distribution. However, it was necessary to investigate whether this kinematic invariance persists within a fully coupled thermodynamic framework. It was hypothesized that altering the initial injection parameters could modify the radial dispersion of the droplet cloud, thereby reshaping the localized cooled region immediately downstream of the atomizer. To evaluate this phenomenon, parametric simulations were executed, independently varying the initial injection velocity and the spray cone angle while holding all other conditions constant.

Comparative analysis of the resulting Lagrangian data revealed that the global RTD curves and the final residual moisture distributions exhibit near-perfect superimposition across all evaluated configurations. Consistent with the uncoupled hydrodynamic findings, the macroscopic transport and overall drying kinetics remain statistically insensitive to the atomizer's initial kinematic specifications. The initial momentum of the dispersed phase is rapidly dissipated by the prevailing aerodynamic forces of the continuous steam environment, effectively decoupling the final product properties from the initial injection angle and velocity.

Despite this macroscopic invariance, localized thermal perturbations were observed within the continuous phase. The influence of these injection parameters on the axial temperature gradients is quantified in Figures (6.23) and (6.24).



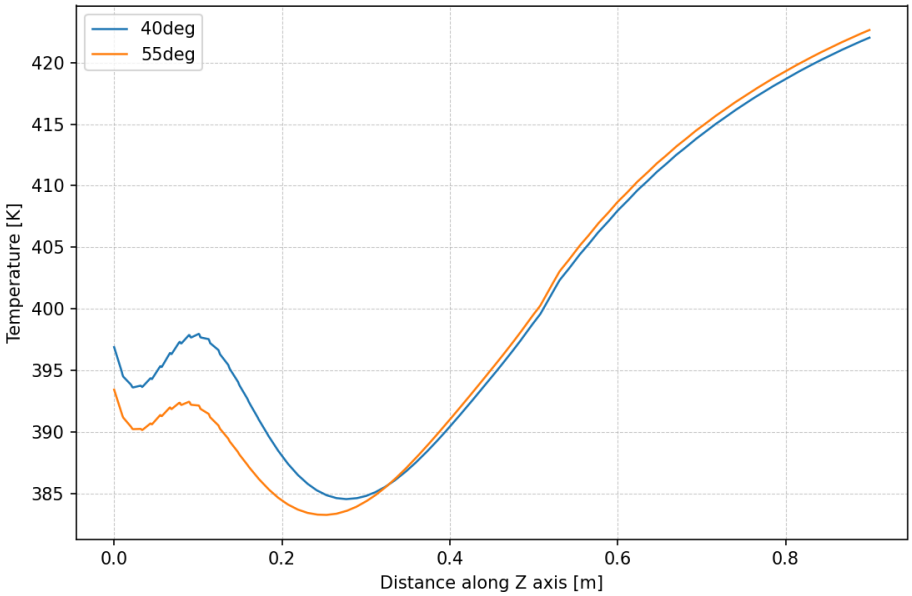
(a) Temperature profile along the central Z-axis, originating immediately below the nozzle.



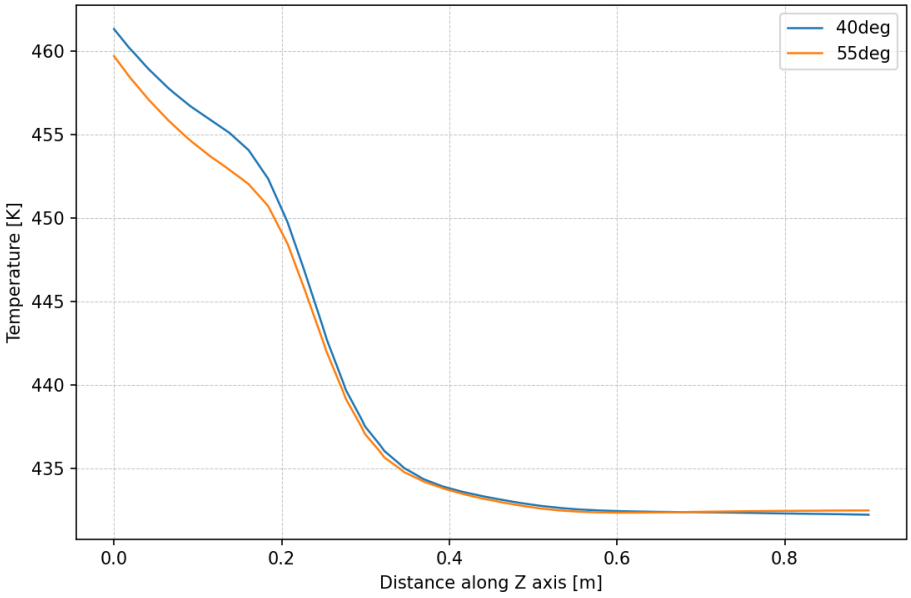
(b) Temperature profile along a vertical axis offset toward the chamber wall.

Figure 6.23: Continuous phase (steam) temperature profiles evaluated at two different injection velocities.

As depicted in both figures, noticeable deviations in the continuous phase temperature field are confined to the primary atomization zone downstream of the nozzle. An increase in the injection velocity marginally elevates the local steam temperature within this immediate region. This occurs because the accelerated droplets penetrate deeper into the spatial domain before convective heat transfer and latent



(a) Temperature profile along the central Z-axis, originating immediately below the nozzle.



(b) Temperature profile along a vertical axis offset toward the chamber wall.

Figure 6.24: Continuous phase (steam) temperature profiles evaluated at two different injection angles.

heat extraction can occur, effectively elongating the thermal sink. Conversely, broadening the injection cone angle exacerbates the localized thermal deficit near the inlet; the dispersed phase is distributed over a wider radial cross-section, cooling a broader, shallower volumetric region.

Nevertheless, beyond this localized atomization zone, the axial thermal profiles converge to an identical bulk equilibrium temperature in the lower regions of the drying chamber. This convergence confirms that while injection kinematics exert a minor spatial influence on the immediate interphase heat transfer rates, they do not alter the global thermodynamic energy balances or the macroscopic drying kinetics of the spray

drying process.

6.3 Particle Drying Kinetics

The idealized single-particle drying kinetics, characterized by constant boundary conditions, were presented in Figure (5.13). In that validation scenario, a stationary droplet suspended within a uniform superheated steam flow showed theoretical temporal evolutions of temperature, diameter, and moisture content, allowing for the precise delineation of the fundamental drying stages.

However, the operational environment within an industrial spray dryer is far from an ideal validation scenario. A dense, polydisperse spray population is injected into a turbulent, three-dimensional flow field. Localized accelerations and decelerations of the continuous phase induce continuous fluctuations in the particle Reynolds number, which alter the convective heat transfer coefficient via the local Nusselt number.

At the same time, the bulk temperature field is bound to severe, non-linear spatial gradients, as demonstrated in the preceding Eulerian scalar maps. The in-situ drying kinetics deviate from idealized zero-dimensional models. To quantify these transient effects, the thermal and morphological histories of five randomly selected, initially similarly sized particles were tracked and analyzed.

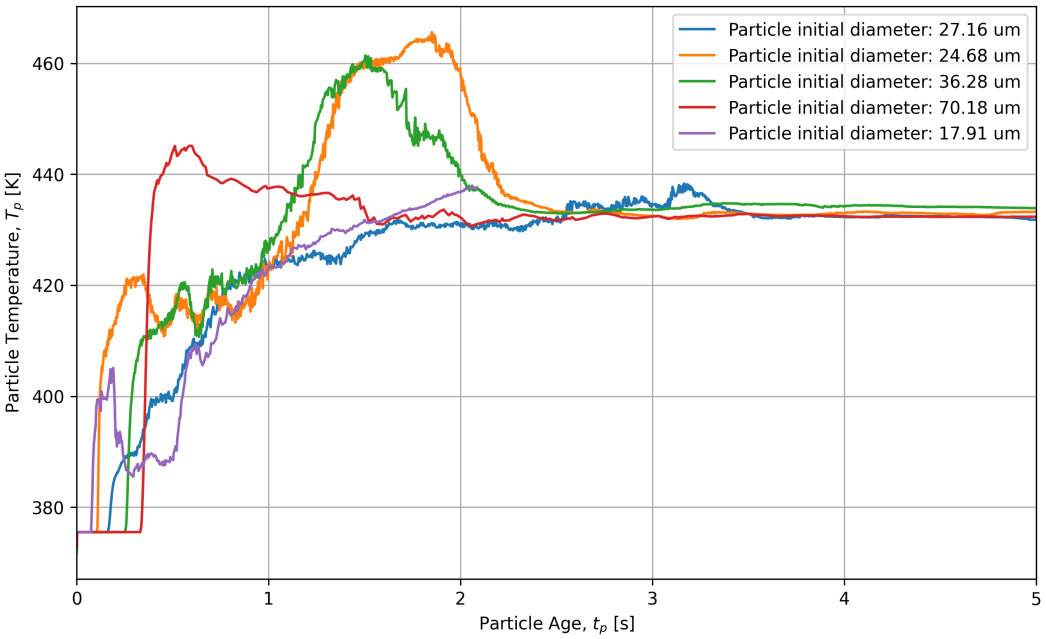


Figure 6.25: Lagrangian temperature evolution of five discrete, similarly sized particles.

Figures (6.25) through (6.28) illustrate the temporal evolution of temperature, diameter, bulk density, and moisture content for these five discrete parcels. These Lagrangian profiles reveal substantial deviations from the idealized baseline established in Figure (5.13).

The thermal histories depicted in Figure (6.25) show an almost instantaneous bypass of the initial sensible heating phase, which is a direct consequence of the elevated droplet injection temperature. The constant-rate drying period starts quickly, lasting a fraction of a second. Following this phase, the particle temperatures begin to climb, marking the onset of the falling-rate period. Notably, the temporal transition into this regime is not uniform; individual discrete parcels enter the falling-rate phase at varying times. Furthermore, the rate of temperature increase is different among the particles, dictated by the specific thermodynamic environments traversed along their respective Lagrangian trajectories.

Throughout the falling-rate period, the particle temperatures do not smoothly approach a uniform equilibrium asymptote. Instead, they experience distinct transient fluctuations. These variations are aerodynamic artifacts; as particles are advected through turbulent eddies, they are subjected to shifting

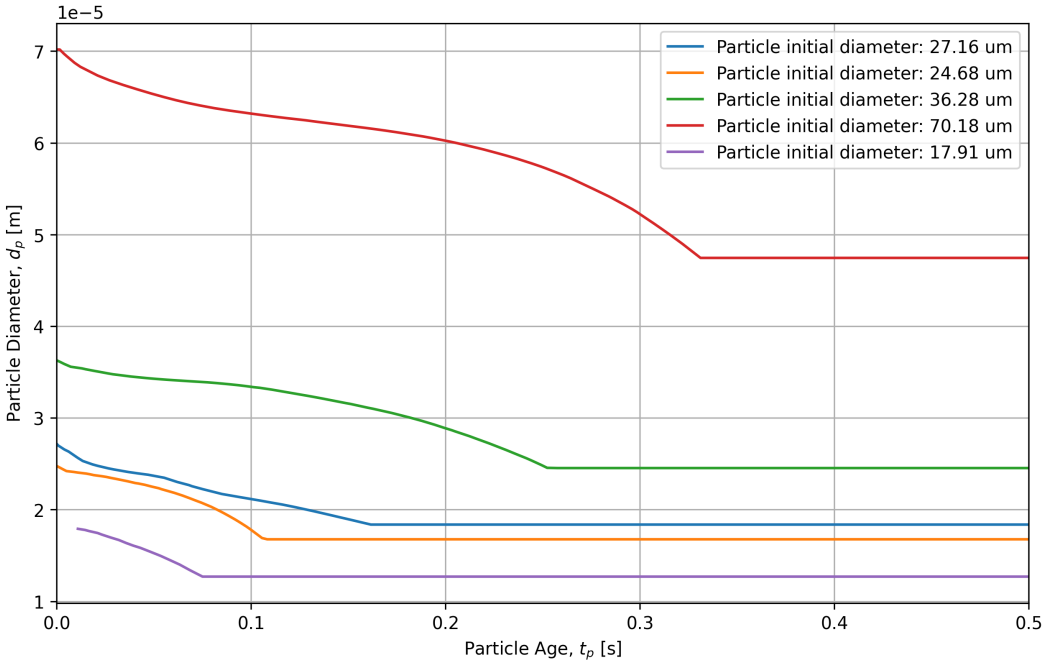


Figure 6.26: Transient diameter evolution of five discrete, similarly sized particles.

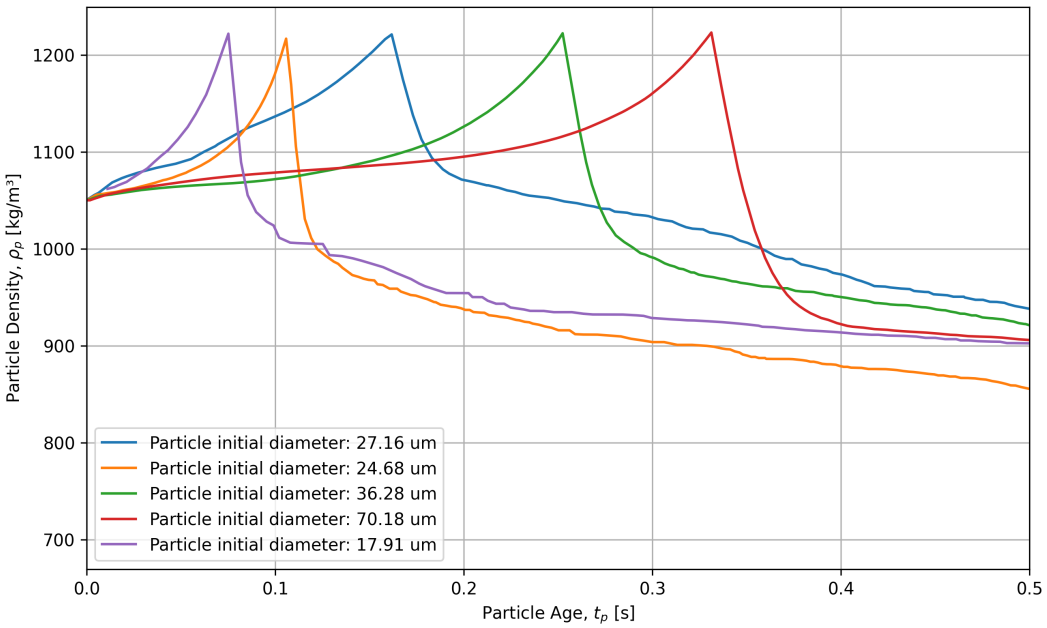


Figure 6.27: Transient residual moisture content evolution of five discrete, similarly sized particles.

local bulk temperatures. For instance, one tracked particle achieves a peak temperature of approximately 460 K before gradually cooling toward the local continuous-phase temperature, whereas other particles experience lower peak temperatures occurring at entirely different temporal coordinates.

This kinematic variability is evident in the morphological evolution presented in Figure (6.26). The transient diameter shrinkage is non-linear. Several trajectories show rapid initial contraction, followed by temporal plateaus where the diameter remains almost constant, before undergoing secondary contraction

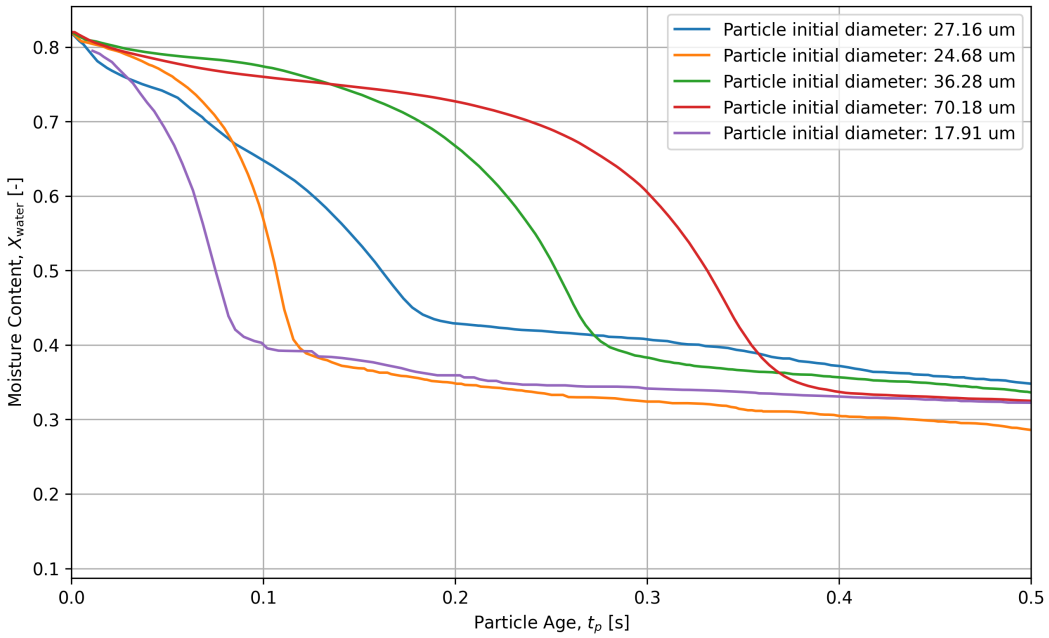


Figure 6.28: The moisture content evolution of 5 random similarly sized particles.

phases prior to solid crust precipitation. The specific onset time of crust formation is unique to each parcel and governed by its specific thermal history.

The density profiles in Figure (6.27) reflect these different transport paths. While all analyzed particles achieve an identical peak density upon the formation of the rigid crust matrix, the exact moment of this structural transition varies. The subsequent density decay, driven by the continued internal vaporization of the constrained wet core, likewise proceeds along divergent trajectories.

The moisture evaporation kinetics (Figure 6.28) further support these findings. The interphase mass transfer rate dynamically fluctuates as the discrete parcels navigate the spatially varying Eulerian fields. For certain trajectories, the moisture content profile exhibits two distinct inflection points, whereas others display a single continuous transition. Due to their unique stochastic trajectories and divergent thermal histories, the discrete parcels converge upon slightly varying final residual moisture contents, generating the continuous macroscopic moisture distribution previously presented in Figure (6.20).

In conclusion, multiphase drying within a cyclonic chamber is a highly transient, path-dependent process. The localized evaporation rates are dynamically coupled to both the transient particle state and the continuous phase. Because discrete parcels are subjected to stochastic turbulent dispersion, no two thermal histories are identical. This trajectory-dependent variance dictates that the final product is characterized not by a single residual moisture value, but by a statistical distribution. Despite these intermediate spatial variations, Figure (6.25) confirms that as the dispersed phase approaches the exhaust boundary, the discrete particle temperatures successfully equilibrate with the bulk continuous phase.

Chapter 7

Conclusion and Future Work

The global trend toward a circular economy and sustainability directives has compelled numerous industrial sectors to re-evaluate their core processing workflows. Minimizing industrial energy consumption remains a primary mechanism for achieving substantial reductions in greenhouse gas emissions. Among these carbon-intensive operations, the industrial drying sector represents one of the most energy-demanding manufacturing workflows globally.

A vast majority of consumer and industrial commodities utilize particulate or powdered intermediates at some stage of their manufacturing lifecycle, requiring thermal dewatering to increase stability and mitigate downstream transport and storage costs. Within this context, spray drying has emerged as a wide spread technique. It is preferentially deployed in the synthesis of high-value products where precise control over final particle morphology, volumetric size, and residual moisture content is necessary.

To improve the ecological and thermodynamic sustainability of these systems, conventional hot air or flue gas drying mediums can be substituted with superheated steam. While Superheated Steam Drying offers thermodynamic advantages over traditional non-condensable carrier gases — most notably the potential for near-total latent heat recovery — its practical implementation introduces novel complexities from both a process control and numerical modeling perspective.

Furthermore, empirical characterization of active spray drying domains is constrained by the harsh, highly transient, and turbulent internal environments of the processing chambers. Given the limitations in acquiring high-fidelity experimental data, the utilization of advanced multiphase Computational Fluid Dynamics frameworks becomes necessary. By leveraging a two-way coupled Eulerian-Lagrangian approach, a specialized phase-change thermodynamic model can be developed. This computational framework enables a high-resolution, analysis of discrete droplet kinematics, localized residual moisture profiles, final product particle size distributions, and macroscopic Residence Time Distributions.

7.1 Key Findings

Throughout this work, an extensive computational fluid dynamics campaign was conducted, comprising of hundreds of core-hours of computational runtime. The numerical framework was developed sequentially, beginning with a baseline evaluation of the single-phase superheated steam hydrodynamics. The continuous-phase simulations revealed the existence of a central recirculation zone which, while stable in its spatial localization, exhibited periodic oscillations. This macro-transient behavior mathematically prevented the convergence of standard steady-state solvers.

However, this transient behavior was bounded; the precessing vortex core remained anchored along the central geometric axis rather than wandering stochastically throughout the domain. This stable macro-structure was verified by using a curvature correction to the Shear Stress Transport ($k-\omega$ SST) turbulence model. Furthermore, a comprehensive grid-independence study conducted across three distinct hexahedral-dominant meshes confirmed that this periodic hydrodynamic behavior was numerically invariant of spatial discretization.

Following the continuous phase simulations, the second phase of investigation analyzed discrete phase transport. Droplets were introduced into the domain through a pressure atomizer, generating a cone spray

of the droplets. A two-way coupled Eulerian-Lagrangian framework was employed to account for interphase momentum, heat, and mass transfer. The validity of this two-way coupling assumption was verified by evaluating the localized spatial distribution of the particle volume fraction (α_p). The system operated within a dilute multiphase regime where particle-particle collisions are negligible but interphase coupling remains highly significant.

The hydrodynamic tracking simulations showed that initial droplet diameter is the most important factor affecting particle trajectories within the domain. Fine particles, characterized by low Stokes numbers execute numerous orbital revolutions within the upper recirculation zones before being advected downstream by the bulk gas flow. Conversely, coarser particles possess sufficient initial inertia to resist continuous-phase streamlines; centrifugal force propels them toward the walls. Upon wall impingement, these coarse particles undergo a series of inelastic collisions, dissipating their initial kinetic energy. These particle experience then a friction-dominated boundary-layer transport regime along the lower conical hopper. This spatial segregation mechanism was confirmed by the boundary collision density heatmaps, which displayed a highly defined, characteristic helical particle roping topology.

Sensitivity studies have been perform to analyze the impact of various parameters on the average RTD. The initial injection angle and droplet velocity showed a negligible impact on the global mass-averaged RTD. The aerodynamic drag of the continuous phase quickly dissipated variations in the initial droplet kinetic energy. Instead, the macroscopic RTD was affected by the inlet Particle Size Distribution and the liquid feedstock mass flow rate. A reduction in the feedstock mass flow rate minimized the axial momentum source terms transferred to the gas, allowing the tangential swirling structures to dominate. This shift expanded the local turbulent eddies, resulting in an RTD heavily skewed toward extended residence times along with an larger statistical variance.

In the last phase, a custom phase-change thermodynamic library was compiled within the OpenFOAM. A new solver resolved heat-transfer limited vaporization within a pure-vapor environment, and its accuracy was verified and validated against benchmark empirical data from the literature. The activation of the vaporization kinetics induced a localized temperature drop directly downstream of the atomizer nozzle. The continuous-phase temperature drops in the nozzle region by up to 80 K. This thermal plume extended radially across the core but did not extend fully towards the walls. The depressed temperature drop marks the spatial boundaries of intense localized mass transfer. Downstream of this primary vaporization zone, convective mixing between the cooled central core and the hotter peripheral steam established a uniform thermal equilibrium prior to the domain exhaust.

An analysis of the Lagrangian drying histories of individual discrete particles showed a high degree of variability. The droplets underwent an initial, rapid sensible heating phase, a constant-rate evaporation period characterized by a thermal plateau, and a falling-rate drying period. During the falling-rate regime a rigid solid crust is formed that undergoes sensible superheating by the surrounding steam. The precise onset and duration of these respective drying phases varied randomly for each discrete parcel, depending entirely on the trajectories traversed by the particles within the turbulent flow field.

The final residual moisture content and product PSD were found to be highly sensitive to the critical moisture content. The value of critical moisture content governs the moisture threshold at which geometric shrinkage stops and the porous solid crust solidifies, dictating both the final particle volume and the quantity of trapped unbound solvent. Other nozzle-specific kinematic parameters had a marginal effect on these final product properties compared to this primary thermodynamic fitting scalar.

In summary, a computational fluid dynamics campaign was executed to advance the understanding of the superheated steam spray drying process. The developed numerical framework generates results that are highly coherent and consistent with contemporary scientific literature. While this computational tool provides process engineers with insights into internal chamber transport, its predictive application must be evaluated having simplifying assumptions in mind. There are numerical limitations present, detailed in the subsequent section.

7.2 Model Limitation

During the development of this numerical framework, several simplifying assumptions were implemented. While these choices were necessary to maintain computational efficiency and solver stability, they restrict

the accuracy of the model. The primary limitations are detailed below:

- **Turbulence Model**. The selected turbulence model relies on the Boussinesq hypothesis, which assumes an isotropic eddy viscosity to resolve turbulent stresses. While this approach is standard and computationally efficient for many industrial applications, it struggles with highly rotational, swirling flows. The isotropic assumption may under predict or mischaracterize the exact physical behavior of the precessing central vortex. Transitioning to a more advanced framework, such as a Reynolds Stress Model, would be necessary to capture these anisotropic turbulent variations accurately.

- **Particle Breakage and Agglomeration**. The current Lagrangian framework omits four-way coupling, assuming that discrete droplets do not collide or interact. In a real spray drying chamber, smaller droplets frequently coalesce into larger ones altering their mass, Stokes numbers, and trajectories. Additionally, solid particles are assumed to be perfectly rigid and immune to mechanical failure. In reality, dry particles can undergo attrition or shatter upon wall impact, exposing trapped core moisture directly to the steam and altering the final residual moisture content.

- **Steam condensation**. The phase-change library is mathematically bounded as a one-way vaporization mechanism. It assumes the continuous phase heats the droplets through sensible heat transfer. In a physical system, the cold surfaces of the newly injected droplets act as localized condensation zones. The continuous steam would transiently condense onto these cold surfaces, releasing large amounts of latent heat during the initial droplet heat-up phase before the boiling-driven evaporation sequence begins.

- **Thermodynamic model**. An ideal gas equation of state was used to describe the continuous steam phase. While this approximation is valid for highly superheated states, its accuracy degrades significantly as the steam approaches the saturation line. A more precise real gas thermodynamic model, or the integration of empirical steam tables, is required to correctly resolve the fluid behavior near the saturation dome, particularly within the steep thermal gradient zone surrounding the nozzle.

7.3 Future Work

Future research initiatives should primarily focus on addressing the numerical and physical limitations outlined in the previous section. First, the custom phase-change library should be expanded to incorporate bidirectional mass transfer, allowing the solver to simulate localized steam condensation alongside vaporization. To complement this, a real-gas equation of state or empirical steam tables should be integrated into the continuous-phase framework to properly resolve fluid behavior near the saturation dome, particularly within the steep thermal gradients of the nozzle region.

To account for particle-particle interactions, a Population Balance Model should be integrated into the Lagrangian framework. This addition would allow the model to simulate droplet agglomeration and particle breakage. To support the implementation of a breakage model, a targeted empirical testing campaign is necessary to investigate the mechanical and structural properties of these hollow, porous particles under impact stress.

Finally, the current numerical framework needs to be validated against comprehensive experimental data from a physical pilot plant. Specifically, future experimental work should focus on measuring internal spatial temperature profiles within the drying chamber, as well as the final product's particle size distribution and average residual moisture content. These physical metrics can subsequently be used as calibration targets to fit the phenomenological critical moisture parameter, ensuring that the model accurately reflects physical reality.

7.3.1 Declaration on the Use of Generative AI

During the preparation of this thesis, a Large Language Model (Gemini by Google) was utilized as a supportive tool for text editing (refining readability, grammar, and phrasing) and as an auxiliary aid for accelerated C++ code prototyping and syntax lookup within the OpenFOAM framework.

The AI was not used to design the core physical models or formulate research conclusions. All algorithmic workflows, thermodynamic models, custom library modifications, and source-code implementations were thoroughly debugged, corrected, verified, and validated independently by the author. The author retains full intellectual ownership and assumes complete responsibility for the accuracy of all written content, numerical implementations, and scientific results presented in this work.

Nomenclature

Dimensionless Numbers

Bi	Biot number
Co	Courant number
Nu, Nu_p	Nusselt number
Pr	Prandtl number
Pr_t	Turbulent Prandtl number
Re, Re_p	Particle Reynolds number

Greek Characters

α	Volume parameter / Helmholtz energy
α_p	Dispersed phase local volume fraction
α_w	Water activity
α_{avg}	Global averaged particle volume fraction
ϵ	Volumetric kinetic dissipation rate
κ	Molecular thermal conductivity
μ	Molecular dynamic fluid viscosity
μ_t	Turbulent dynamic dynamic viscosity
ν_f	Fluid kinematic molecular viscosity
ω	Specific dissipation rate / Acentric factor
ϕ	Arbitrary fluid transport target property
ρ, ρ_f	Continuous phase fluid field density
ρ_p	Effective bulk discrete particle density
$\sigma_k, \sigma_\epsilon, \sigma_\omega$	Turbulent Prandtl numbers
$\vec{\tau}$	Effective continuous phase stress tensor

Latin Characters

$\dot{M}$	Feedstock liquid mass flow rate

$\dot{m}_{p,k}$	Evaporative mass transfer rate
$\vec{F}_B$	Basset history force vector
$\vec{F}_b$	Fluid buoyancy force vector
$\vec{F}_D$	Aerodynamic drag force vector
$\vec{F}_g$	Gravitational force vector
$\vec{F}_L$	Transverse lift forces vector
$\vec{F}_P$	Pressure gradient force vector
$\vec{F}_{vm}$	Virtual mass force vector
$\vec{g}$	Gravitational acceleration vector
$\vec{J}_i$	Diffusive flux vector of species i
$\vec{r}$	Particle spatial position vector
$\vec{u}, \vec{u}_f$	Continuous phase fluid velocity vector
$\vec{u}_p$	Discrete particle velocity vector
$a_0, a_1, \ldots$	Polynomial regression coefficients
a_c	Attractive forces parameter
A_p	Droplet/particle surface area
b	Excluded molecular volume parameter
C_μ	Turbulence calibration constant
C_D	Drag coefficient
c_p	Specific heat capacity
$C_{1\epsilon}, C_{2\epsilon}, C_{3\epsilon}$	Turbulence model constants
D_ω	Cross-diffusion modification term
d_p	Particle or droplet diameter
E	Specific internal energy (or total enthalpy)
F	External aerodynamic body force
$G_\omega, G_{\omega b}$	Specific dissipation rate generation
G_k, G_b	Turbulent kinetic energy generation
H	Specific enthalpy of the steam phase
h	Convective heat transfer coefficient
h_c	Localized film condensation heat coefficient
h_i	Specific enthalpy of species i

H_{evp}	Latent heat of vaporization
k	Turbulent kinetic energy / empirical rate constant
k_g	Thermal conductivity of steam
m_p	Particle or droplet mass
n	Empirical crust resistance exponent
p	Static pressure
q_k	Heat flux to discrete phase parcel k
R	Ideal gas constant
S_E	Volumetric interphase energy source term
$S_k, S_\epsilon, S_\omega$	User-defined turbulence source terms
S_m, S_{mass}	Volumetric interphase mass source term
S_{mom}	Volumetric interphase momentum source
T	Continuous phase fluid temperature
t	Temporal variable (time)
T_g	Glass transition temperature
T_p	Particle or droplet temperature
T_R	Reduced temperature (T/T_{crit})
T_∞	Bulk continuous phase background temperature
T_{sat}	Operational solvent boiling point threshold
V_{avg}	Volumetric size of a computational cell
V_{domain}	Total interior volume of drying chamber
$v_{i,k}$	Velocity components of evaporating mass
V_{mol}	Molar volume
X	Dry-basis moisture content
X_c, X_{cr}, X_{crit}	Critical moisture content threshold
Y_ω	Turbulence dissipation of omega parameter
Y_M	Compressibility dilatation dissipation
Z	Compressibility factor (pV_{mol}/RT)

Bibliography

[1] C. Strumillo, P.L. Jones, and Romuald Żyłła. Energy aspects in drying. *Handbook of Industrial Drying*, pages 1075–1101, 07 2014. 1, 5

[2] Ian C. Kemp. *Fundamentals of Energy Analysis of Dryers*, chapter 1, pages 1–45. John Wiley Sons, Ltd, 2011. 1, 9

[3] Arun S. *Handbook of Industrial Drying*. Taylor Francis Group, LLC, 2006. 1, 6

[4] W. Rähse and O. Dicoi. Produktdesign disperser stoffe: Industrielle sprühtrocknung. *Chemie Ingenieur Technik*, 81(6):699–716, 2009. 1, 6

[5] Iva Filkova, Li Xin Huang, and Arun S Mujumdar. *Handbook of Industrial Drying*, chapter 10 : Industrial Spray Drying Systems. Taylor Francis Group, LLC, 2006. 1, 5, 7, 8, 9

[6] Tobias Linke and Reinhard Kohlus. What is a functional design for a superheated steam pilot plant spray drier? - design considerations for food applications. *Drying Technology*, 43(13):1962–1977, 2025. 1

[7] Arun S Mujumdar. *Handbook of Industrial Drying*, chapter 19 : Superheated Steam Drying. Taylor Francis Group, LLC, 2006. 1, 2, 6, 9, 10

[8] Mariia Sobulska, Pawel Wawrzyniak, and Meng Wai Woo. Superheated Steam Spray Drying as an Energy-Saving Drying Technique: A Review. *Energies*, 15(22):8546, November 2022. 1, 2, 6, 10, 11, 12, 13

[9] Ali Darava. *CFD Simulation of Spray Drying process using a New Droplet Drying Kinetics*. PhD thesis, Univ., 2016. 2, 11, 12, 15, 20, 21, 22, 24

[10] W.R.W. Daud et al. M.W.Woo, A.S. Mujumdar. *Spray Drying Technology Volume One*. 2010. 2, 5, 6, 7, 8, 9, 15, 22

[11] Narjes Malekjani and Seid Mahdi Jafari. Simulation of food drying processes by Computational Fluid Dynamics (CFD); recent advances and approaches. *Trends in Food Science & Technology*, 78:206–223, August 2018. 2, 15, 19, 22, 23

[12] A. Frydman, J. Vasseur, F. Ducept, M. Sionneau, and J. Moureh. Simulation of spray drying in superheated steam using computational fluid dynamics. *Drying Technology*, 17(7-8):1313–1326, August 1999. 2, 13, 16, 17, 18, 22

[13] Ananda J. Jadhav and Mostafa Barigou. Eulerian-Lagrangian Modelling of Turbulent Two-Phase Particle-Liquid Flow in a Stirred Vessel: CFD and Experiments Compared. *International Journal of Multiphase Flow*, 155:104191, October 2022. 2, 15, 24

[14] Arun S Mujumdar. *Handbook of Industrial Drying*, chapter 1 : Principles, Classification, and Selection of Dryers. Taylor Francis Group, LLC, 2006. 5, 6, 10

[15] Farooq Hussain, Maciej Jaskulski, Marcin Piatkowski, and Evangelos Tsotsas. CFD simulation of agglomeration and coalescence in spray dryer. *Chemical Engineering Science*, 247:117064, January 2022. 8

[16] S.M. Hosseinalipour and A.S. Mujumdar. Superheated Steam Drying of a Single Particle in an Impinging Stream Dryer. *Drying Technology*, 13(5-7):1279–1303, January 1995. 13, 18, 22, 23

[17] Rinil Kuriakose and C. Anandharamakrishnan. Computational fluid dynamics (CFD) applications in spray drying of food products. *Trends in Food Science & Technology*, 21(8):383–398, August 2010. 15, 19, 20, 24

[18] Hasan Jubaer, Sepideh Afshar, Jie Xiao, Xiao Dong Chen, Cordelia Selomulya, and Meng Wai Woo. On the effect of turbulence models on CFD simulations of a counter-current spray drying process. *Chemical Engineering Research and Design*, 141:592–607, January 2019. 15, 18, 19, 20

[19] Marco Trofa, Igino Foglia, Federica Vallefuoco, Valentina Ruggiero, Paola Russo, Domenico Larobina, and Gaetano D'Avino. CFD modeling and experimental validation of spray drying for inhalable particles. *Chemical Engineering Science*, 322:123083, March 2026. 15, 16, 20, 24

[20] Ettore Fadiga, Nicola Casari, Alessio Suman, and Michele Pinelli. CoolFOAM: The CoolProp wrapper for OpenFOAM. *Computer Physics Communications*, 250:107047, May 2020. 17, 18

[21] Bruce E. Poling, J. M. Prausnitz, and John P. O'Connell. *The properties of gases and liquids*. McGraw-Hill, New York, 5th ed edition, 2001. 17, 18

[22] Dominik Martynek, Luděk Ridvan, and Miroslav Šoóš. In-depth CFD simulation of a spray drying process of Indometacin using ethanol as a solvent. *Powder Technology*, 473:122217, April 2026. 17, 19

[23] Johannes Vincent Bürger, Maciej Jaskulski, and Abdolreza Kharaghani. Modeling of maltodextrin drying kinetics for use in simulations of spray drying. *Drying Technology*, 43(1-2):214–227, January 2025. 18

[24] Lili Xia, Hamid Montazeri, and Bert Blocken. On the accuracy of Eulerian-Lagrangian CFD simulations for spray evaporation in turbulent flow. *International Journal of Thermal Sciences*, 208:109461, February 2025. 19, 20

[25] Andrea Milanesi, Giada Diana, Alessandro Candiani, Alessandro Sodano, Paolo Rassè, Andrea Foglio Bonda, Elia Bari, Maria Luisa Torre, Lorena Segale, and Lorella Giovannelli. Spray drying: From a traditional technology to modern biotechnological applications. *International Journal of Pharmaceutics: X*, 10:100449, December 2025. 20

[26] S V Apte, K Mahesh, and T Lundgren. A Eulerian-Lagrangian model to simulate two-phase/particulate flows. *Center for Turbulence Research Annual Research Briefs 2003*, 2003. 20

[27] L. Schiller and A. Maumann. Über die grundlegenden berechnungen bei der schwerkraftaufbereitung. *Zeitschrift des Vereines deutscher Ingenieure*, 77(12):318–320, March 1933. 21

[28] Fangnian Wang, Jianjun Xiao, and Thomas Jordan. Two-way Eulerian-Lagrangian coupling approach in GASFLOW code for containment spray modelling. *Nuclear Engineering and Design*, 413:112495, November 2023. 21, 22

[29] Thanit Swasdisevi, Wut Thianngoen, and Somkiat Prachayawarakorn. Mathematical Modeling and Design of Parboiled Paddy-Impinging Stream Dryer Using the CFD-DEM Model. *Foods*, 13(10):1559, May 2024. 24

[30] OpenFOAM Documentation - reactingParcelFoam — doc.openfoam.com. https://doc.openfoam.com/2306/tools/processing/solvers/rtm/lagrangian-particle/reacting{P}arcel{F}oam/. [Accessed 22-07-2026]. 31

[31] OpenFOAM Documentation - Reacting Mixture — doc.openfoam.com. https://doc.openfoam.com/2306/tools/processing/models/thermophysical/mixture/rtm/reacting{M}ixture/. [Accessed 22-07-2026]. 31

[32] 31

[33] Nikolaos D. Katopodes. *Vorticity Dynamics*. Elsevier, 2019. 42

[34] M.J. Andrews and P.J. O'Rourke. The multiphase particle-in-cell (mp-pic) method for dense particulate flows. *International Journal of Multiphase Flow*, 22(2):379–402, 1996. 45

[35] Kwan Lee and D. J. Ryley. The evaporation of water droplets in superheated steam. *Journal of Heat Transfer*, 90(4):445–451, 11 1968. 51

[36] Zelin Zhou, Timothy A. G. Langrish, and Sining Cai. Using Particle Residence Time Distributions as an Experimental Approach for Evaluating the Performance of Different Designs for a Pilot-Scale Spray Dryer. *Processes*, 11(1):40, December 2022. 57

[37] Alírio E. Rodrigues. Residence time distribution (RTD) revisited. *Chemical Engineering Science*, 230:116188, February 2021. 57

[38] K. El Korchi, R. Alami, A. Saadaoui, S. Mimount, and A. Chaouch. Residence time distribution studies using radiotracers in a lab-scale distillation column: Experiments and modeling. *Applied Radiation and Isotopes*, 154:108889, December 2019. 57

[39] Ankur Kapil, Claire Wombwell, Laurel L. Kegel, and Michael D. Hamlin. Model-aided process development for scalable spray drying of sticky substances. *Frontiers in Chemical Engineering*, 7:1565916, April 2025. 59